CHARGE TRANSFER IN POLY(3-HEXYLTHIOPHENE)/TITANIUM DIOXIDE INVERSE OPALS: EFFECTS OF SURFACE PASSIVATION AND DONOR CONCENTRATION

CHRISTOPHER KERR

A THESIS SUBMITTED TO

THE FACULTY OF GRADUATE STUDIES

IN PARTIAL FULFILLMENT OF THE REQUIREMENTS

FOR THE DEGREE OF

MASTER OF SCIENCE

GRADUATE PROGRAM IN CHEMISTRY

YORK UNIVERSITY

TORONTO, ONTARIO

APRIL 2018

Abstract

Hybrid photovoltaics are attractive because of their low cost and ability to be applied onto flexible substrates. However defect states can trap charges and are undesirable. We investigate TiO_2 inverse opals treated with titanium tetrachloride ($TiCl_4$) and subsequently coated with poly(3-hexylthiophene) (P3HT) to elucidate the effect of surface passivation on the photoinduced charge transfer and polaron dynamics. The chemical, physical and morphological properties were characterized using UV-vis spectroscopy, reflectance microscopy, X-ray diffraction, Raman spectroscopy and scanning electron microscopy. Passivation resulted in increased wall thickness of the inorganic framework and crystallite size. Photoinduced absorption spectroscopy showed enhanced polaron absorptions and reduced polaron lifetimes with increased titanium tetrachloride concentration and reduced concentration of the solution from which the P3HT is cast. The 3D structure presents an opportunity to study the charge transfer within a percolated network.

Acknowledgements

The research involved in completing my Master's thesis was a colossal task that I would never have been able to accomplish if it wasn't for the support of the Chen group members. I'd like to thank Dr. Chen for giving me the opportunity to learn a more hands – on approach to materials chemistry and introducing me to the topic of photonic crystals and their applications in solar cells research. Dr. Chen has always been willing to provide her insight and assist me in my research. I'd like to thank Nick Tulsiram for his invaluable instruction regarding pretty much every procedure I had to do and in showing me how to analyze my data. I'd like to thank the following Chen lab members who have made my experience a joyful one, on both an intellectual and emotional level: Bach Kim Nguyen, who was among the very first people to greet me and always offered me bagels during lunch breaks. Brian Malile, who always took time out of his busy schedule to help me find reagents in the lab or operate instruments. I'd also like to thank Lili for providing me with her valuable postdoctoral insight into matters relating to graduate studies. I'd like to thank Shane Robichaud of Perkin Elmer for his expertise in trouble shooting UV – Vis spectrometers whenever I ran into trouble when operating them. I'd like to thank Prof. Vladimir Kitaev at Wilfred Laurier University for assisting with Raman spectra acquisition and Magdelena Jackwicz for her assisitance in operating the scanning electron microscope. I'd like to thank my father for his support in my studies. Finally, I'd like to thank my mother, whose unshaken faith in me and my abilities propelled me through elementary school, high school, my undergraduate studies and finally graduate studies, while allowing me to succeed in every way I could. She believed I could do this project when I thought I couldn't and if it wasn't for her humor, enthusiasm, moral support, and generosity I wouldn't have made it as far as I have.

Table of Contents

List of Tables

Chapter 2

Chapter 3

List of Figures

Chapter 1

Chapter 2

Chapter 3 Figures

Appendix Figures

List of Schemes

List of Equations

List of Acronyms

Abs	Absorptance
AFM	Atomic force microscopy
Ag	Silver
APS	Ammonium persulfate
ALD	Atomic layer deposition
BHJ	Bulk Heterojunction
CdSe	Cadmium selenide
CdS	Cadmium Sulfide
CdTe	Cadmium Telluride
D:A	Donor Acceptor
$C_8H_{16}I_2$	1,8 – diiodo-octane
DSSC	Dye Sensitized Solar cells
EA	Electro-absorption

E_g	Energy gap
FCC	Face center cubic
F_{air}	Fraction of air
$F_{dielectric}$	Fraction of dielectric material
FTO	Fluorine doped tin oxide
FWHM	Full width half maximum
Ge	Germanium
HE	High Energy
$(-CH_2(CH_2)_4CH_3)$	Hexyl side chains
HOMO	Highest occupied molecular orbital
H_2O	Water
H_3BO_3	Boric acid
IPCE	Incident photon-to-current conversion efficiency
InGaP	Indium Gallium Phosphide
InGaAs	Indium Gallium Arsenide
IR	Infrared

ITO	Indium tin oxide
IO	Inverse opal
J_{sc}	Short-circuit current density
LPD	Liquid phase deposition
LE	Low Energy
LUMO	Lowest unoccupied molecular orbital
Mg	Magnesium
MQ	Milli-Q
MoO_3	Molybdinum oxide
mc-Si	Monocrystalline Silicon
n_{air}	Refractive index of air
NASA	North American Space Association
$n_{dielectric}$	Refractive index of dielectric
NH_4OH	Ammonium hydroxide
$NH_4S_2O_8$	Ammonium persulfate

$HS(CH_2)_8SH$	1,8-Octandithiol
OPV	Organic Photovoltaics
$PC_{61}BM$	[6,6]-Phenyl-C_{61}-butryic acid methyl ester
$PC_{71}BM$	[6,6]-Phenyl-C_{71}-butyric acid methyl ester
PhC	Photonic crystal
PL	Photoluminescence
PIA	Photoinduced absorption
PV	Photovoltaic
pc-Si	Polycrystalline Silicon
P3HT	Poly(3-hexylthiophene)
P3HT:PCBM	P3HT:PCBM nano-composite
P3HT:PCBM/TiO_2	1:1 P3HT:PCBM cast over TiO_2
P3HT/PCBM/TiO_2	P3HT cast over PCBM cast over TiO_2
P3HT/mTiO_2	P3HT mesoporous titania nanocomposite
i-P3HT/TiO_2-o	P3HT inverse opal titania nanocomposite
PMHCTCT	Poly(3-(2-methyl-2-hexylcarboxylate) thiophene-co-thiophene
PS	Polystyrene
PTB7	Polythieno[3,4-b]-thiophene-co-benzodithiophene
PTB7 F20	Poly(thienothiophene-co-benzodithiophenes)7-F20

PCE	Power conversion efficiency
QDSSC	Quantum dot sensitized solar cells
QTH	Quartz tungsten halogen lamp
SWA	Scalar wave approximation
SEM	Scanning electron microscopy
SiO_2	Silica
SiO_x	Non-stoichiometric silica
TiO_2	Titania
TiBALDH	Titanium Bis(ammonium lactato) dihydroxide (**Sigma-Aldrich**); Diammonium dihydroxybis[lactato(2-)-O1,O2] titanate(2-) (**IUPAC**)
$Ti(ButO)_4$	Titanium Butoxide
$TiCl_4$	Titanium tetrachloride
TiF_6^{-4}	Hexfluorotitanate
UV	Ultra-violet
V_{oc}	Open-circuit voltage
XRD	X-ray diffraction

ZnO	Zinc Oxide

Chapter 1. Introduction

1.1. Traditional inorganic photovoltaics and emerging materials

The photovoltaic principle describes the production of electrical current in a device upon exposure to solar energy. Monocrystalline silicon (mc-Si) exhibits the highest theoretical photovoltaic conversion efficiency in accordance with the Shockley-Quesseir limit, which is about 30%[1], and has shown high energy practical conversion efficiencies of 25%[2]. However, the cost required to fabricate high purity crystalline Si is a prohibitive as a long term replacement for non – renewable resources like fossil fuels[2,3]. Titania (TiO_2) polymorphs would be a prime candidate for the replacement of Si due to their ease of use, low toxicity, and low cost of fabrication[4,5,6,7,8,9], if not for their large bandgaps. Assuming negligible scattering, absorption can only occur if the photon has an energy greater than or equal to the band gap of the semiconductor[10,11]. The band gap of Si is 1.1 eV[2], comparable to the energy of an infrared photon at a wavelength of 1100 nm, and therefore photoconduction is possible using ultra violet (UV), visible, and some infrared (IR) light[2]. The band gap of anatase TiO_2 is 3.25 eV[4] and can only be superseded by UV photons with wavelengths of 382 nm or lower[4] . The influence of bandgap on photovoltaic performance and the solar energy distribution is summarized in **Figure 1.1**. Bandgaps impose a limit on the practical use of native TiO_2 for solar cell applications. Since only 5% of solar photons entering the earth's atmosphere are UV active, only 5 % of solar photons have enough energy to excite electrons from the valence band into the conduction band[3]. **Figure 1.1 B** illustrates the process behind photon induced charge generation in semiconductors using UV photons and visible photons for large and low bandgap materials, respectively. The visible region (green) of the solar spectrum offers the largest concentration of harvestable solar photons and much work has been done to fabricate solar cells with materials that can harvest these photons.

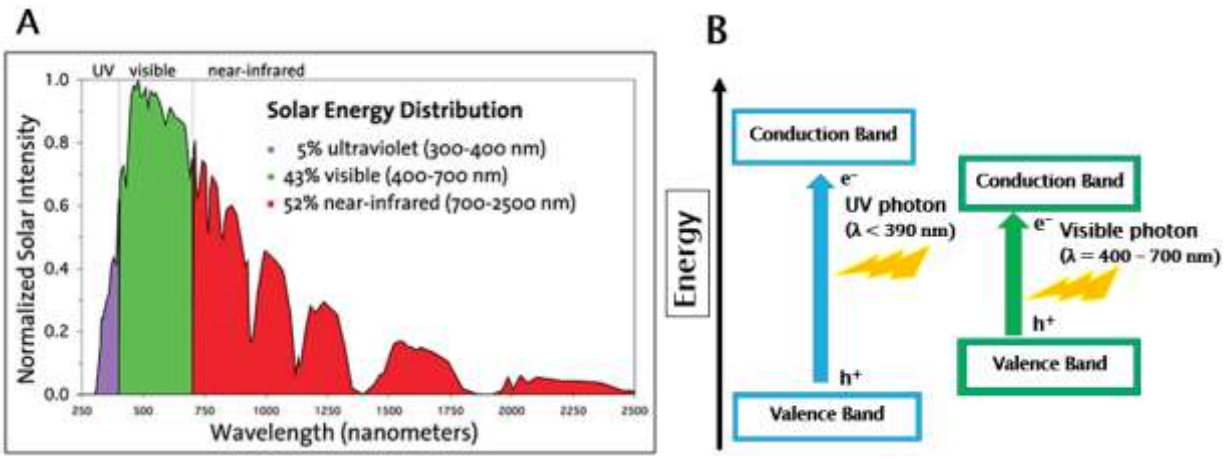

Figure 1.1: Distribution of normalized solar intensity (Air mass 1.5) as a function of wavelength (A). Normalized solar intensity is measured in power per unit area, power being proportional to the number of photons available for absorption at a given wavelength. The distribution is integrated with respect to wavelength within regions defining UV (purple), visible (green), and infrared (red). Adapted with permission from Ref [11]. A generic energy level diagram illustrating radiation induced excitation in a semiconductor by visible and ultra violet solar photons (B).

To efficiently harvest the sun's available energy, a plethora of architectures have been developed, the efficiencies of which are summarized in **Figure 1.2**. Light-weight multi-junction solar cells function by combining crystals of group III-V elements. Reaching efficiencies close to 50%, they are the most efficient class of solar cells. Indium gallium phosphide:indium gallium arsenide:germanium (InGaP:InGaAs:Ge) device efficiencies have reached 37.4%[12] and are of particular interest for aerospace applications due to their light weight, but their high manufacturing cost limits their target market to space technology corporations such as NASA[13]. Subsequent architectures include thin-film photovoltaics, such as cadmium telluride (CdTe) which have reached efficiencies of 22% as of 2016 based on modules developed by First Solar. These efficiencies are comparable to polycrystalline silicon (pc-Si) modules while having slightly lower production costs, making them primary competitors for Si photovoltaics.

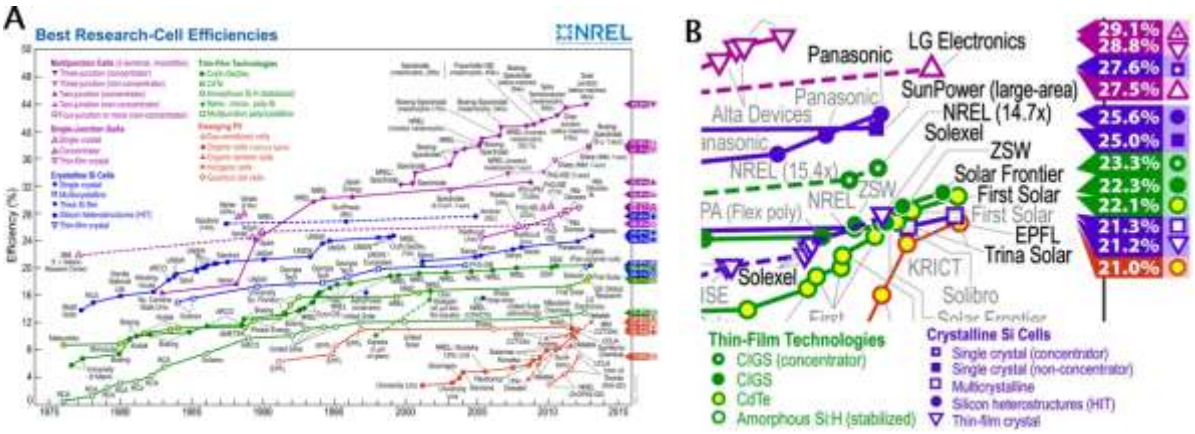

Figure 1.2: A summary graph of the best cell efficiencies for single and mutli-junction solar cells (A, purple), crystalline silicon solar cells (blue), as well as thin-film technologies (green). Detailed plot of the efficiency of emerging photovoltaics including perovskite solar cells (B, yellow triangles, red circle) and CdTe (B, yellow circles, green outline). This plot is reprinted with permission from the National Renewable Energy Laboratory, Golden, CO[14].

Comparable efficiencies of CdTe to Si can be achieved by coupling CdTe to MgCdTe to form a hetero-structure and applying a SiO_x anti-reflective coating[15]. Despite this, CdTe efficiency has yet to equal single crystalline Si and silicon hetero-structures (see **Figure 1.2 A**, blue circles), and the limited supply of tellurium in the earth's crust proves to be a significant bottleneck to replacement of Si with CdTe[16], thus the goal of Si replacement is long term sustainability in combination with efficiency, and emerging photovoltaics based on dye-sensitization, perovskite crystals, and organic bilayers seek to rectify sustainability issues by converting ubiquitous materials into flexible, light-weight devices. Futhermore, Cd toxicity may limit their application.

Dye-sensitized solar cells (DSSC) function by depositing mesoporous metal oxides onto a transparent electrode and sensitizing them with a broadband, light-active molecular dye which absorbed sunlight and donates electrons through the metal oxide layers into the cathode after excitation. A surrounding electrolyte is also included, which forms a redox couple with the sensitizer dye, repeating the process[17], and as of 2014 have resulted in devices reaching 13% efficiency when coupled with panchromatic sensitizers[18], exceeding the required efficiency for commercialization[19]. However larger efficiencies are still required to compete with Si solar cells; the plateau in the efficiency

for DSSC may indicate a saturation point for the device improvement (see **Figure 1.2 A** red outlined circles), and the reduction in device efficiency with temperature imparts seasonal limitations for DSSC in countries such as Canada[20].

Perovskite materials are composed of minerals of the formula ABX_3 where A is usually an ammonium group, B is a lead ion and X are halogen ions[21]. Their broadband absorption capabilities can be tuned by substituting different halides into the structure[22], making it possible to produce efficienct films using about 100 nm of material[23], and their charge transport capabilities are efficient enough to produce 100% charge collection efficiency. The growth in efficiency of perovskite solar cells are among the fastest with an average growth of 2.61%/year between 2009 and 2016 which is unprecedented for a solar cell architecture[24]. Perovskite solar cells have low manufacturing costs compared to Si photovoltaics[25]. However, the most efficient perovskite solar cells utilize lead ions and lead content of typical perovskites is non-trivial which may hinder their commercialization, due to Pd toxicity or availability[26]. Perovskite materials can also degrade in the presence of electrolytes when there are incorporated into DSSC[27]. Limitations connected to electrolyte application and toxic materials have led to the application of organic compounds for solar cell applications[28].

1.2. Organic photovoltaics

Organic photovoltaic devices (OPV) have emerged as a counter architecture to costly inorganic semiconductor photovoltaics[29]. The use of organic layers can provide increased flexibility unavailable in inorganic photovoltaics and additional market opportunities provided by roll-to-roll printing techniques. Flexibility also reduces the possibility of physical damage done to the cells during transport.[29]. Printing applications provided by, for example, ink-jet processing also reinforce the possibility of ‘paintable’ photovoltaics[30]. In addition, OPV devices can be rendered from non-toxic, abundant materials with low manufacturing costs compared to inorganic PV. Despite cost efficiency, OPV have lower lifetimes and efficiencies than traditional inorganic PV. Sources of limitation can be better understood by examining the mechanism of OPV operation.

Organic solar cells are excitonic solar cells. The principle of operation relies on a light active material, generally a conjugated polymer with an energy gap between 3.18

and 1.77 ev (390 to 700 nm). Absorption of light leads to the excitation of an electron from the highest occupied molecular orbital (HOMO) level to the lowest unoccupied molecular orbital (LUMO) level, forming a coulombically-bound exciton. The production of excitons in an organic photoactive layer is illustrated in **Figure 1.3 A.** In contrast to inorganic semiconductors where excitons exhibit weaker binding energies on the order of 0.01 eV, excitons of organic compounds exhibit large binding energies because of the small dielectric constant of organic molecules[31]. **Figure 1.3 B** shows that, when the excitonic polymer comes in contact with another compound of LUMO level slightly below that of the excited polymer, the exciton will dissociate into electrons and holes if the potential difference between the two energy levels is at least large enough to overcome the exciton's binding energy[32], which is on the order of 0.3 to 0.5 eV for conjugated polymers[33,34]. Free electrons will then transfer into the neighbouring materials lower lying LUMO, representing the electron affinity of the acceptor compound, and a hole will be left behind in the HOMO of the previously excited polymer, now referred to as a donor[35]. Large exciton binding energy is a key reason for reduced device efficiency of organic solar cells compared to inorganic solar cells[29]. Incorporation of electron donors and acceptors allows for charge generation at the donor:acceptor (D:A) interface by aligning the electron donor's LUMO to be slightly higher in energy than the conduction band of the electron acceptor[36]. Once free charge carriers are produced, the difference in the anode and cathode work-functions will drive the free electrons and free holes through the various electron and hole transporting materials, respectively, completing the circuit[32].

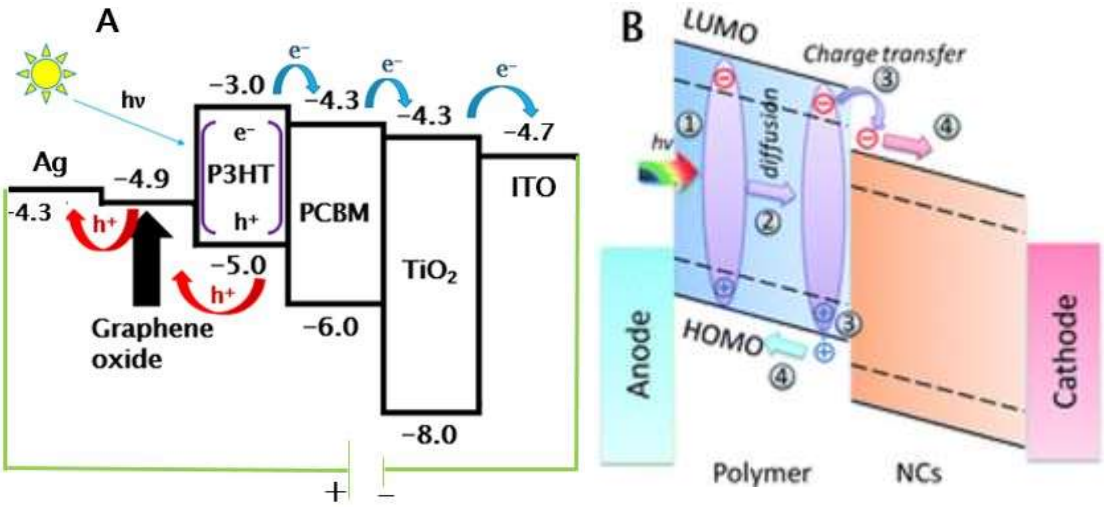

Figure 1.3: Energy level diagram for a P3HT:PCBM solar cell device with P3HT functioning as a donor and PCBM as an acceptor (A). Horizontal black lines highlight HOMO or LUMO energy levels for P3HT, PCBM,TiO_2, or work function values of the electrodes. Work functions for the electrodes are not to scale. Connections of electrodes to a load are shown in green. Photoinduced exciton formation within P3HT is highlighted by purple brackets. Energy level diagram illustrating exciton diffusion and charge transfer between polymer and nanocrystal (NC) acceptor species. Figure B used with permission from Ref [36].

OPV efficiency can be enhanced by rational design of photoactive layer architecture instead of using different combinations of compounds[28] and electrodes[37] or by modifying the interfacial contact between donor, acceptor, and transporting groups[32].

1.3. Bulk Heterojunction solar cells

Photoactive layers of early OPV were assembled in a bi-layer fashion[38] shown in **Figure 1.4 A**. Donor and acceptor materials are casted sequentially to form films with only the center of the photoactive layer forming the donor:acceptor interface. Limitations of this architecture stem from inefficient charge carrier production compared to inorganic photovoltaics. For this reason, the photoactive layers must be on the order of 100 nm, which limits absorption, for charge carriers to reach electrodes[39]. Furthermore, exciton diffusion lifetime, which is on the order of 1 nano-second (ns)[40], requires the interfacial thickness of the exciton generation site in the donor phase and the donor:acceptor

interface to be on the order of approximately 5 - 20 nm for regio-regular poly(3-hexylthiophene) (P3HT)[40], restricting the thickness of self-assembled donor layers to these dimensions. Given that photoactive layers of 100 nm are required for sufficient charge carrier generation, only a fraction of excitons will be able to dissociated at the interface[41]. To this end other architectures optimizing charge carrier generation and exciton diffusion efficiency via an internal donor:acceptor network have been employed.

The bulk heterojunction system (BHJ) maximizes charge transfer efficiency by thoroughly dissolving and mixing electron donating and accepting materials together with differing or equal weight ratios. The donor:acceptor mixture can then be cast over an electrode substrate. Phase separation will occur if the entropy of mixing of the components is small[42], leading to a self-assembled, bicontinuous, interpenetrating donor:acceptor network whose interface thickness is similar to the exciton diffusion length of the donor material[43]. Bilayer and bulk heterojunction architectures are summarized in **Figure 1.4**.

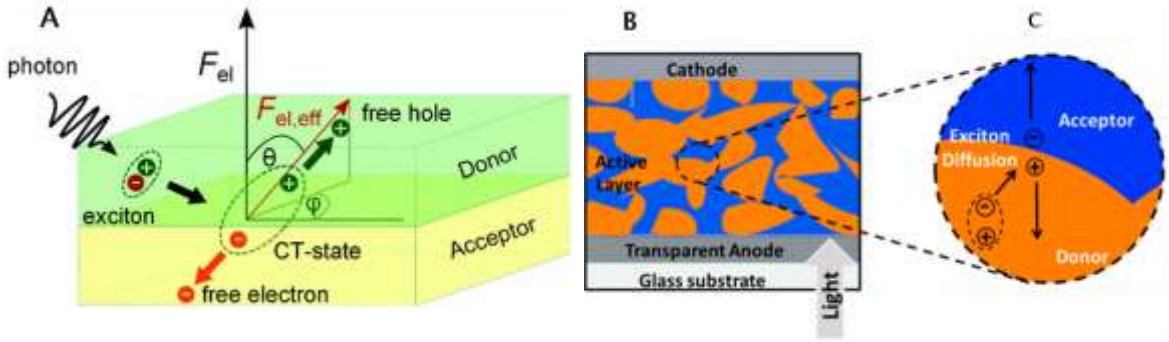

Figure 1.4: An example of a bilayer photoactive layer. Green and yellow denote the donor and acceptor compounds, respectively. Photoinduced exciton formation is shown in the donor phase, encapsulated by dashed circle around the green and red dots marking holes and electrons, respectively. Similar process for BHJ architecture. Figure A adapted with permission from Ref [38]. Figure B and C adapted with permission from Ref [43].

The bi-continuous network increases the interfacial contact between the donor and acceptor compounds, amplifying the total production of charge carriers[4]. The most widely studied BHJ solar cell is composed of poly (3-hexyl thiophene) (P3HT) as the donor. P3HT is used due to its low cost compared to other donor polymers, stability, and

the wealth of existing studies concerning its properties[45]. P3HT is often coupled to the acceptor [6,6] phenyl C_{60} butyric acid methyl ester (PCBM) due to the favourable alignment of its LUMO energy with P3HT's LUMO level[46], high electron mobilities[46], and quick charge transfer dynamics on the order of 40 fs aided by the ultrafast dissociation of its exciton renders this a functional architecture[44]. **Figure 1.5** outlines the large variation of reported P3HT:PCBM solar cell efficiencies compiled between 2002 and 2010. Variation in P3HT:PCBM device performance can be traced to different fabrication techniques and optimization methods that alter the morphology of the blend. For example, BHJ nano-morphology can be influenced by thermal annealing of photoactive layer[49]. Zhao *et al*. fabricated a Poly[[4,8-bis[(2-ethylhexyl)oxy]benzo[1,2-b:4,5-b']dithiophene-2,6-diyl][3-fluoro-2-[(2-ethylhexyl)carbonyl]thieno[3,4-b]thiophenediyl]]:phenyl C-71 butyric acid methyl ester (PTB7:$PC_{71}BM$) solar cell and reported a PCE of 3.26% after thermal annealing, while the non-annealed controlled devices yielded a PCE of 1.81%[48]. Enhanced PCE is attributed to roughening of the photoactive layer surface, increasing interfacial contact between electrodes and the photoactive surface.

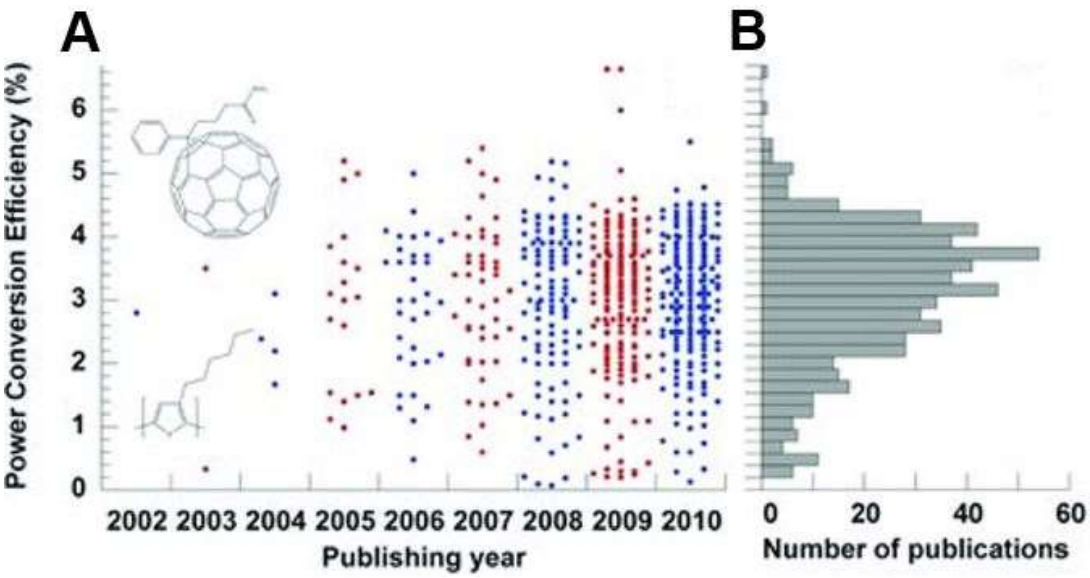

Figure 1.5: Power conversion efficiencies for select P3HT:PCBM devices as a function of publication year (A). Insets reveal the molecular structures of PCBM (top) and P3HT (bottom). Each dot corresponds to a maximum PCE. Red and blue dots signify odd and even numbered years, respectively. The number of publications associated with a specific PCE range (B). Figure adapted with permission from Ref [47].

Kadem *et al*. came to similar conclusions in their annealing treatment of P3HT:PCBM films, which alters the phase separation as well[49]. They attribute increase roughness to enhanced phase segregation of PCBM and report increased absorption of the films between 300 and 800 nm upon heat treatment in **Figure 1.6**. Phase separation can also be promoted by solvent additives such as 1,8-diiodooctane ($C_8H_{16}I_2$) and 1.8-octanedithiol ($HS(CH_2)_8SH$). In the fabrication of their PTB7:$PC_{71}BM$ nano-composite, Liang *et al*. dissolved the donor:acceptor materials in various solvent mixes. They report the following PCE for each solvent condition i.) pure dicholorbenzene, PCE = 6.22%, ii.) 97% to 3 % of dichlorobenzene to 1,8-diiodooctane, PCE = 7.18%, iii.) pure chlorobenzene, PCE = 3.92%, and iv.) 97% to 3% chlorobenzene to 1,8-diiodooctane, PCE = 7.40%[50]. The enhancement in PCE is traced to homogeneous charge carrier extraction at the electrode:photoactive layer interface, due to better phase organization, leading to reduces short circuit current densities.

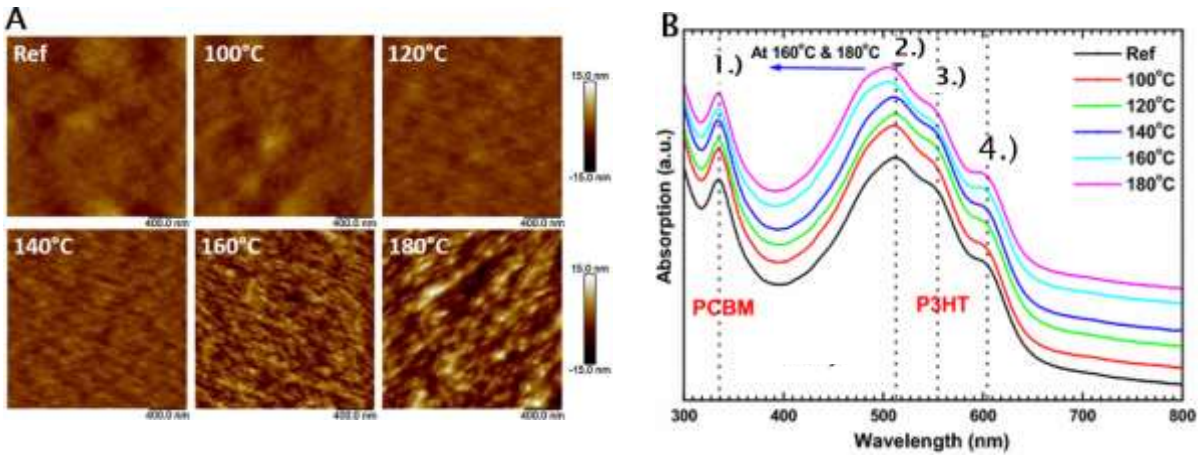

Figure 1.6: Atomic force micrographs (AFM) for a P3HT:PCBM film treated with various annealing temperatures (A). Bright regions correspond to PCBM domains. Scale bars to the right denote degree of surface roughness (rms). UV-Vis absorption spectra for P3HT:PCBM films annealed at various temperatures. PCBM absorption features are noted at 340 nm (1). P3HT absorption features are noted at 513 nm (2), 560 nm (3), and 605 nm (4). The reference film refers to P3HT:PCBM film without heat treatment. Figure adapted with permission from Ref [49].

1.4. Hybrid solar cells

Inorganic acceptors have distinct advantages over organic acceptors such as consistent phase morphology and crystallinity during solution processing[51], large surface areas[52], continuous carrier conduction pathways by virtue of the inorganic network that can be anchored directly onto the electrode surface[53], and reduced recombination of charge carriers compared to organic acceptors due to localization of electrons onto inorganic acceptors and holes onto organic polymers[54]. Breakthroughs in dye-sensitized perovskites solar cell efficiencies can be traced to the use of inorganic acceptors in their hybrid architectures[55,56]. Hybrid solar cells can be fabricated as bilayers, in which a planar inorganic film is cast with an organic solution, or as bulk heterojunctions by solution processing of surfactant coated colloidal nano-crystals, such as lead sulfide (PbS) quantum dots, with organic polymers[57]. Bulk heterojunctions can also be formed by growing cheap, abundant, environmentally friendly metal oxide acceptors such as TiO_2 and zinc oxide (ZnO) in nano-rod arrays[51], nano-tube arrays[58], nano-belts and nano-helices to form an intercalated network. Kuo *et al.* investigated the performance of P3HT-TiO_2 solar cells as a function of TiO_2 architecture summarized in **Figure 1.7**[51] Devices fabricated using TiO_2 nano-rod arrays demonstrated device efficiencies of 0.512% while bilayer samples demonstrated efficiencies of 0.12%. The increase in efficiency due to nano-rod array is attributed to improved absorption of P3HT in the rod array compared to the film as seen in **Figure 1.7 D**, enhanced donor:acceptor contact afforded by the larger surface area of TiO_2 nano-rods, as well as improved electron transport through TiO_2 due to anchoring of TiO_2 nano-rods on ITO[51]. Futhermore, increased P3HT absorption could be attributed to different ordering of polymer[59,60,61].

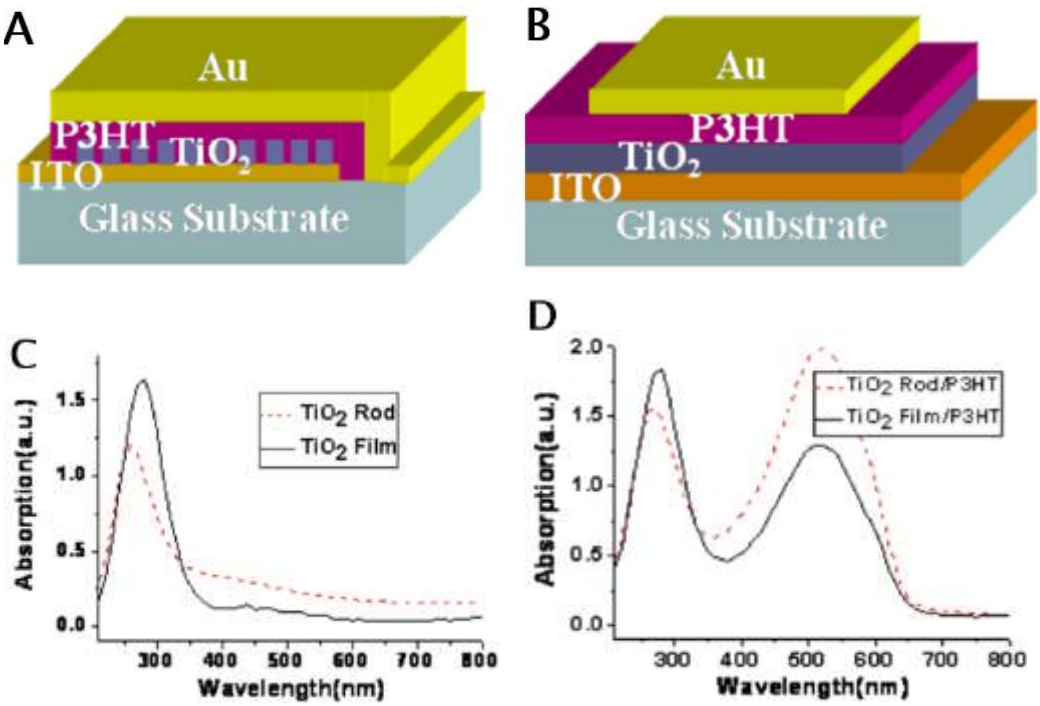

Figure 1.7: Schematic showing a bi-layer (A) and bulk heterojunction (B) hybrid nano-composite. Absorption of TiO_2 nano-rods and films are noted by dashed red and solid black lines, respectively (C). Absorption of P3HT:TiO_2 nano-rod and film composites are noted by dashed red and solid black lines, respectively (D). Figures adapted with permission from Ref [51].

This highlights the effects of nanoscale architecture on absorption properties of donor compounds[62], and the effect of surface area on charge generation has led to the application of metal oxide based photonic crystal inverse opals in solar cells as electron accepting compounds[63].

1.5. Photonic Crystals

Photonic crystals (PhC) are nanomaterials that have periodic, dielectric contrast on the length scale of a light wave in one, two, or three dimensions[64]. PhC have composite refractive indices much like a distributed Bragg reflector[65] where each crystallographic plane acts as a mirror allowing incident radiation to transmit through the crystal or reflect at various angles according to Bragg's law (**Eqn 1.1**) depending on the refractive index change according to Snell's law (**Eqn 1.2**).

$$m\lambda = 2d_{111}\sin\theta \quad \text{(Eqn 1.1)}$$

Refractive index considerations can be accounted for by Snell's law (**Eqn 1.2**) which describes the change in the refracted angle (θ_1 and θ_2) in terms of refractive index variations at an interface (n_1 and n_2).

$$n_2\sin\theta_2 = n_1\sin\theta_1 \quad \text{(Eqn 1.2)}$$

The Bragg condition is illustrated in **Figure 1.8**. The solid black spheres represent generic point lattices in a crystal structure and black lines represent the crystallographic planes. λ is the wavelength of incident radiation, d is the distance between the [111] crystallographic planes, θ is the angle of scattered radiation, and n is the refractive index of the material[66]. Bragg diffraction accounts for the spectacular colours of photonic crystals. Colours in these structures do not arise from molecular transitions but are instead produced by coherent Bragg diffraction of visible light off the material along specific crystallographic directions[66]. Photonic structures are ubiquitous in nature. They are responsible for the biological iridescence observed in butterfly wings[67] shown in **Figure 1.8 B**, spinal iridescence in the sea mouse[68] , the remarkable colour patterns in peacock feathers[69] , as well as iridescence in opal gemstones[64].

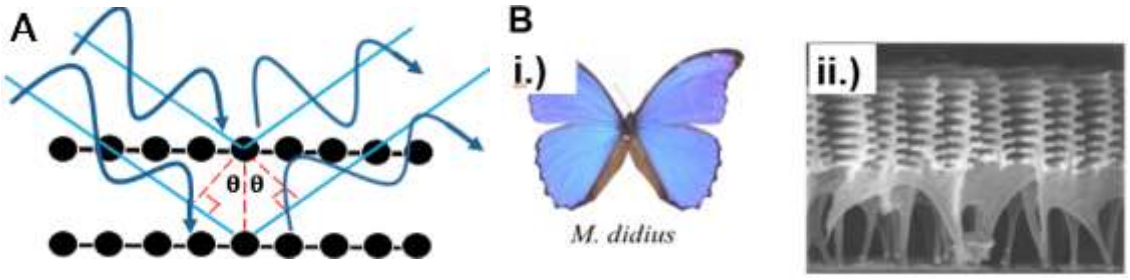

Figure 1.8: A schematic outlining the Bragg condition for reflection of incident radiation upon a crystal (A.)). An example of a natural photonic crystal found in Morpho didius (B.)). An overview of the wing structure as it would appear by the human eye (B, i)). A SEM image of the wing scales (B, ii). Figure B adapted with permission from Ref [67].

Constructive interference of radiation upon scattering will give rise to a sharp peak in the reflectance spectrum. This is known as the photonic stop band and it encapsulates a specific wavelength range where light is forbidden to propagate through the crystal and is thus reflected. To this end photonic crystals can function as inverted

interference filters[70], where instead of passing a narrow wavelength range of radiation through the film it instead reflects a narrow wavelength range. The amplitude of an incoming light wave focusses on the low and high dielectric materials at the blue and red edges of the photonic stopband, respectively. **Figure 1.9** illustrates a reflectance spectrum of a photonic crystal as a function of wavelength. Slow photons result at the edges of the photonic band gap marked in circles. It has been shown by Chen *et al* that photo-degradation of methylene blue dye absorbed onto a TiO_2 photonic crystal experiences a two-fold enhancement when the excitation light source is coupled to the red-edge of the photonic stopband[66].

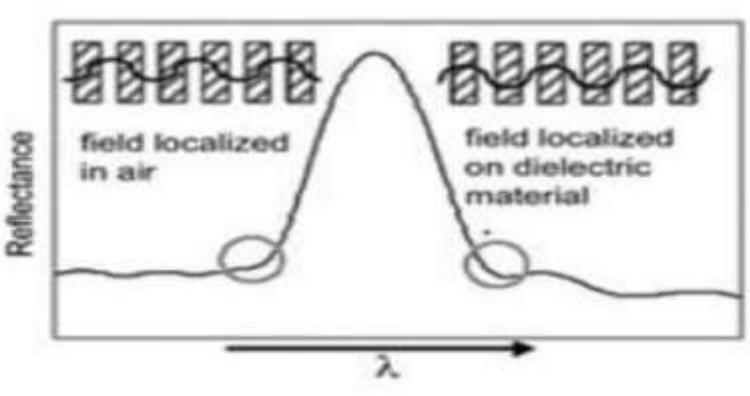

Figure 1.9: The energy of a light wave as a function of wave vector and the reflectance spectrum as a function of wavelength illustrating the presence of slow photons. Figure adapted in part from Ref [65]. Copyright 2003 American Chemical Society.

The stop band position can be tuned by varying the degree of dielectric contrast between the materials constituting the structure and the periodicity. This can be shown qualitatively by modifying Bragg's law with Snell's law (**Eqn 1.3**), where D represents the diameter of a particle arranged in a face centered cubic array, $\boldsymbol{\lambda}$ represents the stop band position, $\boldsymbol{\theta}$ represents the angle of incident light relative to the normal of the film, and m is the order of the reflection.

$$\boldsymbol{m\lambda = 2\frac{\sqrt{2}D}{\sqrt{3}}\sqrt{{n_{eff}}^2 - \sin^2\theta}} \qquad \text{(Eqn 1.3)}$$

The effective refractive index (neff) can be calculated by summing the compact filling factor of air and dielectric material multiplied (f and 1-f, respectively) by their respective refractive indices (n_{air} and $n_{dielectric}$)[71] (Eqn 1.4).

$$n_{eff} = n_{air}f + (1\text{-}f)n_{dielectric} \quad \text{(Eqn 1.4)}$$

Work has been done on enhancing absorption using poly(3-(2-methyl-2-hexylcarboxylate) thiophene-co-thiophene) (PMHCTCT) and PCBM nanocomposites by localization of light due to low group velocity of photons[72]. Ko *et al*. reported a 70% improvement in device efficiency stemming from improved light absorption and an increase in electrical factors by virtue of a 10% improvement in open circuit voltage[72]. However, this field remains largely unexplored.

1.6. Charge generation in hybrid inverse opal nano-composites

Previous member of the Chen group investigated how the slow photon enhancement influences P3HT polaron absorption and lifetime in inverse opal (IO) photonic crystal P3HT/TiO_2 nanocomposites (i-P3HT/TiO_2-o)[73]. Charge generation and lifetime of charge carriers was investigated as a function of acceptor composition[73], as shown in **Figure 1.10 A**. Casting P3HT onto TiO_2 inverse opals provided on average a 3 times enhancement in charge carrier generation compared to reference P3HT:PCBM and P3HT/meso-TiO2 nano-composites, which is attributed to an increase in P3HT-TiO_2 contact area provided by the inverse opals large surface area as well as differences in polymer ordering. Differences in the P3HT polaron lifetime were observed (**Figure 1.10 B)**. A faster drop off in normalized differential transmittance (-ΔT/T) with frequency indicates longer polaron lifetimes. Mesoporous and inverse opal TiO_2 acceptors exhibited a polaron lifetime of approximately 7.91 ms while PCBM bulk heterojunction exhibited polaron lifetimes of 0.525 ms. The larger polaron lifetime in P3HT-TiO_2 films arise from higher dielectric screening, but potentially also from trap states of the inorganic semiconductors. We hypothesized that the surface defects accompanying the large surface area to volume ratio of TiO_2 inverse opals act as recombination centers for charge carriers, lengthening the lifetime of charge capture by trap states

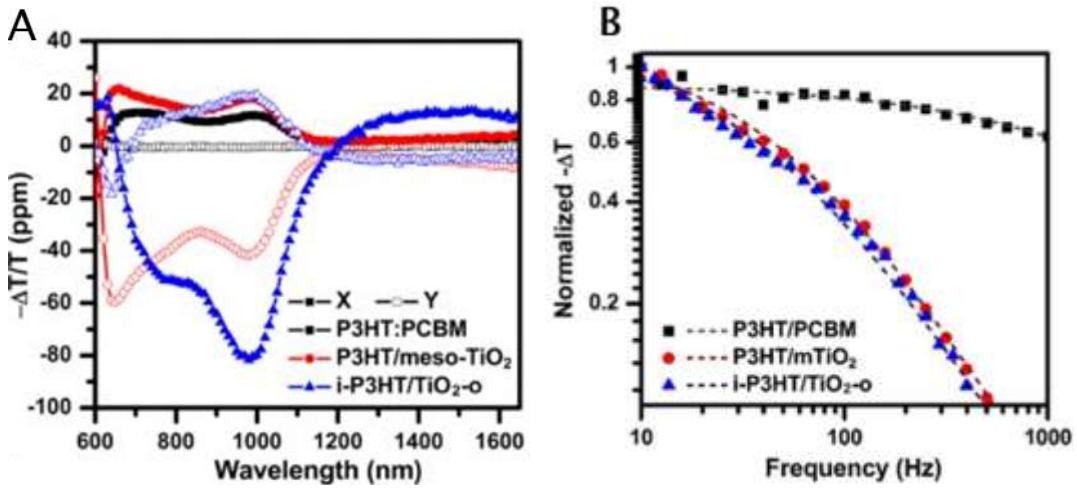

Figure 1.10: Photoinduced absorption spectra for P3HT: PCBM (black squares), P3HT/meso-TiO_2 (red circles) and inverse opal cast with P3HT (blue triangles) (A). X channel signals correspond to in-phase signals and are represented by solid shapes while Y channel signals correspond to out of phase signals and are presented by unfilled shapes (white). Normalized transmittance as a function of pump frequency for P3HT:PCBM (black squares), P3HT:mTiO_2 (red circles), and i-P3HT/TiO_2-o (blue triangles) (B). Dashed lines show modulated fits. Figures adapted with permission from Ref [73].

1.7. Trap states and Passivation

Trap states in nano-crystalline solids are defined as intermediate energy states that exist between the valence and conduction bands of a semiconductor. Trap states manifest as structural defects produced during heating/calcination and cooling of crystal samples[74] and are also characterized by their proximity to either the valence or conduction band, with shallow trap state energy levels occurring closer to either the conduction or valence bands[75] or deep trap state energy levels occurring halfway within the band gap[75] as shown in **Figure 1.11**. Defects can manifest as uncapped surface bonds[76], or complete vacancies in the crystal structure[77], grain boundaries[78], and organic:inorganic junctions[79]. Electrons caught in shallow traps can sometimes be thermally promoted into a conduction band due to their proximity in energy to the conduction band and can even assist in charge transport through diffusion[80]; however deep trap states, such as surface hydroxyls or oxygen vacancies, are especially

detrimental to photovoltaic performance efficiencies since these vacancies function as recombination centers for conduction band electrons and trapped holes, inhibiting charge transport[76]. Extensive characterization has revealed photoluminescence (PL) of recombination processes[81] as well as the facets recombination tends to occur on[82]. Recombination of CB electrons with VB holes captured by oxygen vacancies exhibit green PL, while recombination of trapped CB electrons with VB holes by surface hydroxyls exhibits red PL[81], with the red and green PL processes being localized onto the [101] and [001] crystal facets, respectively[82].

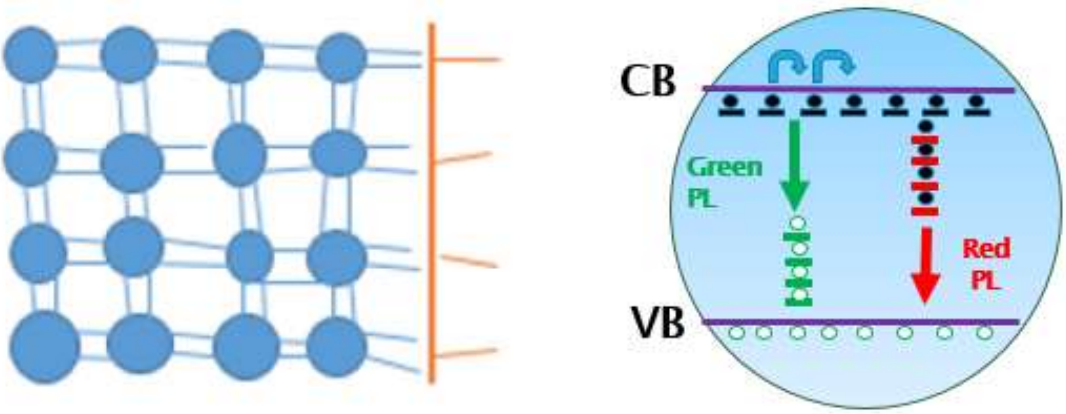

Figure 1.11: An illustrated example of the passivation of trap states arising due to surface defects for a generic semiconductor crystal. Blue circles represent atoms and blue lines represent bonds. Yellow lines represent passivated surface bonds.

It has been established that trap states localized to nano-crystalline surfaces in dye sensitised solar cells (DSSC) deteriorate electron transport within the cell electrolyte solution; however this can been rectified by surface treatment, which is not possible for bulk trap states[83]. Lee *et al* improved the efficiency and charge transfer dynamics of DSSC by passivating the TiO_2 surface and the results are summarized in **Figure 1.12**[76]. An increase in the electron diffusion coefficient as a function of photo-charge density for TiO_2 films annealed with 5 mM $TiCl_4$ (**Figure 1.12 D**) was observed. Furthermore, electron recombination frequency was amplified due to surface area increases resulting from additional TiO_2 deposition (**Figure 1.12 C ii**). An increase in power conversion efficiency when the films were treated with 15 – 50 mM of $TiCl_4$ results, from 3.6% for non-passivated films to 4 %, 4.7%, 5 % for 5 mM, 15 mM, and 50 mM $TiCl_4$-treated

samples, respectively, (**Figure 1.12 A**, **Figure 1.12 C iii**) resulted. Enhanced incident photon to current efficiency (IPCE) between 500 and 750 nm increased with $TiCl_4$ treatment was observed and attributed to light scattering from rutile over-layers (**Figure 1.12 B**)[76].

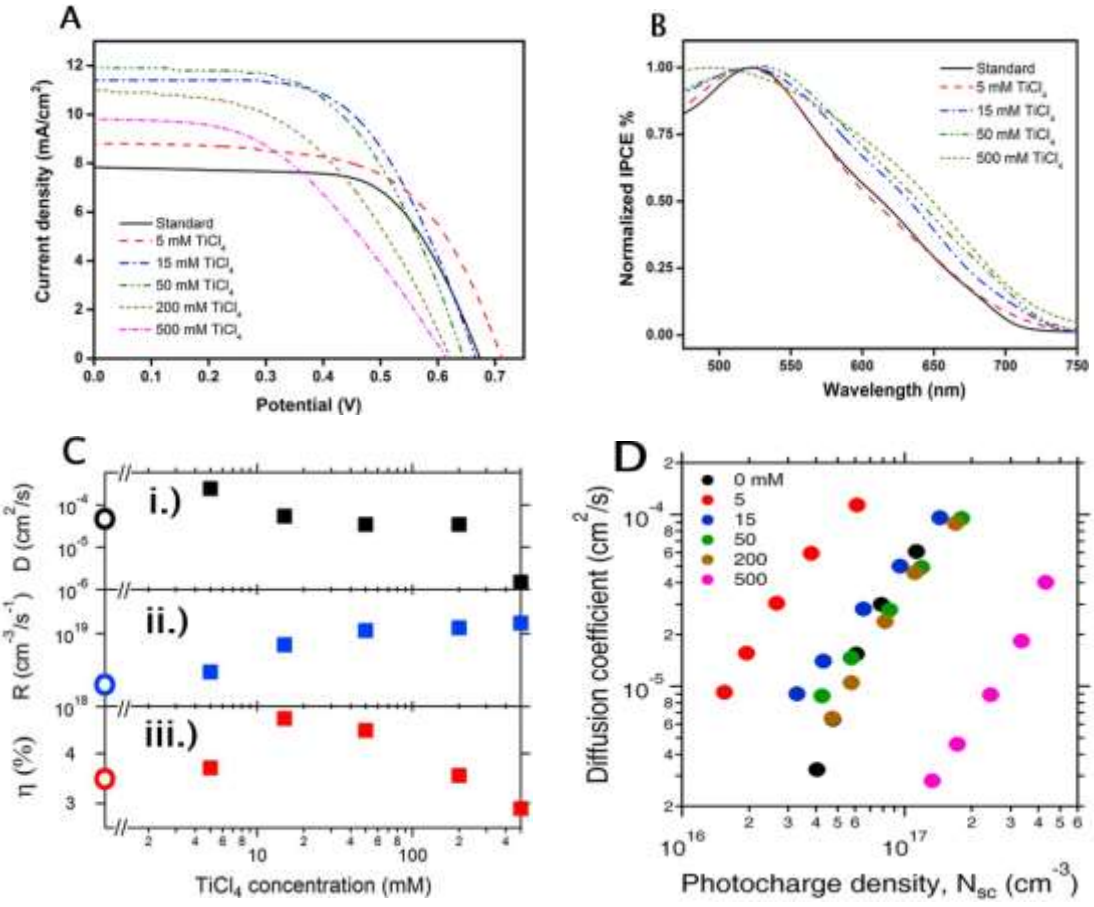

Figure 1.12: A summary of current density as a function of applied voltage (A) and incident photon-to-current converson efficiency (IPCE) (B) for non-passivated (black), 5mM (red,dashed), 15 mM (blue, dashed) 50 mM (green dashed) 200 mM (gold, dashed) and 500 mM (pink, dashed) $TiCl_4$ treatment. Figures of merit for $TICl_4$ treated dye-sensitized solar cells as a function of $TiCl_4$ concentration (C). Overall device efficiency is shown as red squares, recombination rates shown as blue squares, and electron diffusion coefficients shown as black squares. Figure adapted with permission from Ref [76].

Rutile formation from $TiCl_4$ treatment has been observed in mixed phase TiO_2 nanoparticles, particularly P25 Degussa which are 75% anatase to 25% rutile[84]. The

most efficient TiO_2 photocatalysts are composed of mixed anatase/rutile phases due to synergistic effects between the two phases, leading to enhanced charge separation[85]. Dark current measurements of nano-composites assembled by Knorr *et al* using $TiCl_4$ treated P25 Degussa TiO_2 nanoparticles and just pure anatase failed to yield a potential onset shift in current density that would be expected if $TiCl_4$ treatment altered the conduction band edge[84]. Furthermore, work done in the McHale group regarding photoluminescence quenching in $TiCl_4$ treated films sheds light on the mechanism of passivation. **Figure 1.13** displays a feature at 540 nm. This broad visible emission is observable under inert atmosphere and is associated with electrons trapped within surface oxygen vacancies. Upon treatment of $TiCl_4$, the photoluminescence feature at 540 nm of pure anatase TiO_2 is slightly supressed, while that of mixed phase TiO_2 is completely supressed, suggesting additional TiO_2 deposited from $TiCl_4$ hydrolysis functions as a 'healing' agent that remedies TiO_2 defects. These results also indicate that the effect of passivation may differ depending on the phase of TiO_2.

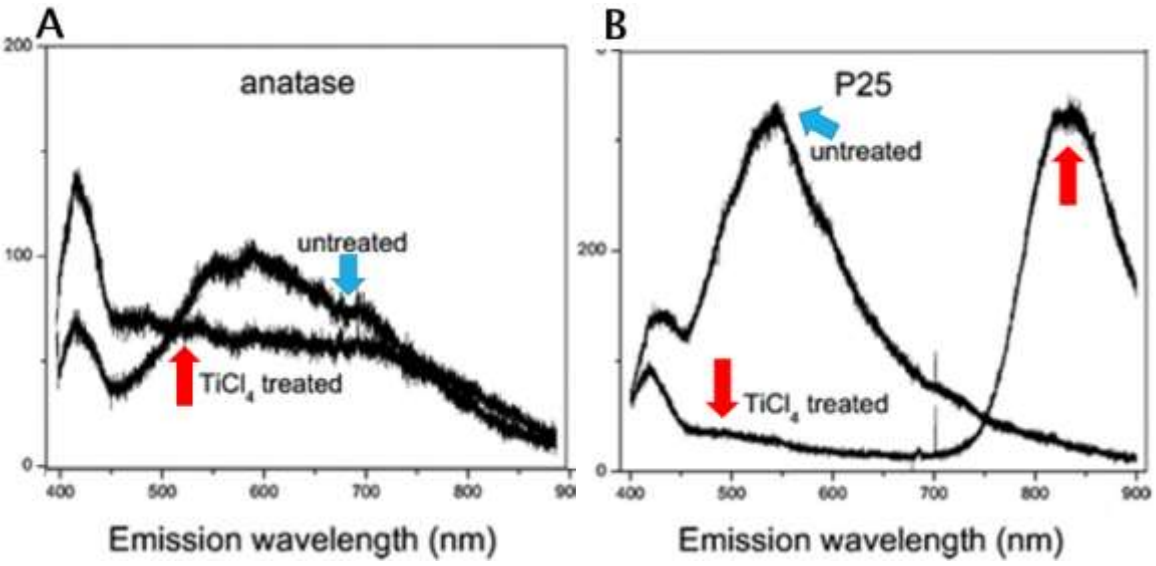

Figure 1.13: Photoluminescence spectra for anatase (A) and 75% anatase to 25% rutile nanoparticle mixture (B) before and after $TiCl_4$ treatment. Figures adapted with permission form Ref [84].

Furthermore, mixed phase TiO_2 results in a strong near infrared (IR) feature at 950 nm (**Figure 1.13 B**) associated with rutile emission. Rutile TiO_2 was observed through Raman spectroscopy in $TiCl_4$ treated P25 nano-particles, and the complete quenching of anatase PL in $TiCl_4$ treated P25 nano-particles supports the claim that

passivation results in a rutile layer over the nanoparticles after 30 minute calcination at 450 ^{o}C (**Figure 1.13 B**)[84,86]. However, a similar experiment probing PL intensity of TiO_2 films, with and without $TiCl_4$ applied, as a function of applied voltage in aqueous media did not reveal significant green PL quenching upon passivation, suggesting the trap states aren't completely passivated. Therefore the mechanism of improved charge transport remains controversial. PL intensity as a function of applied voltage is shown in **Figure 1.14.**

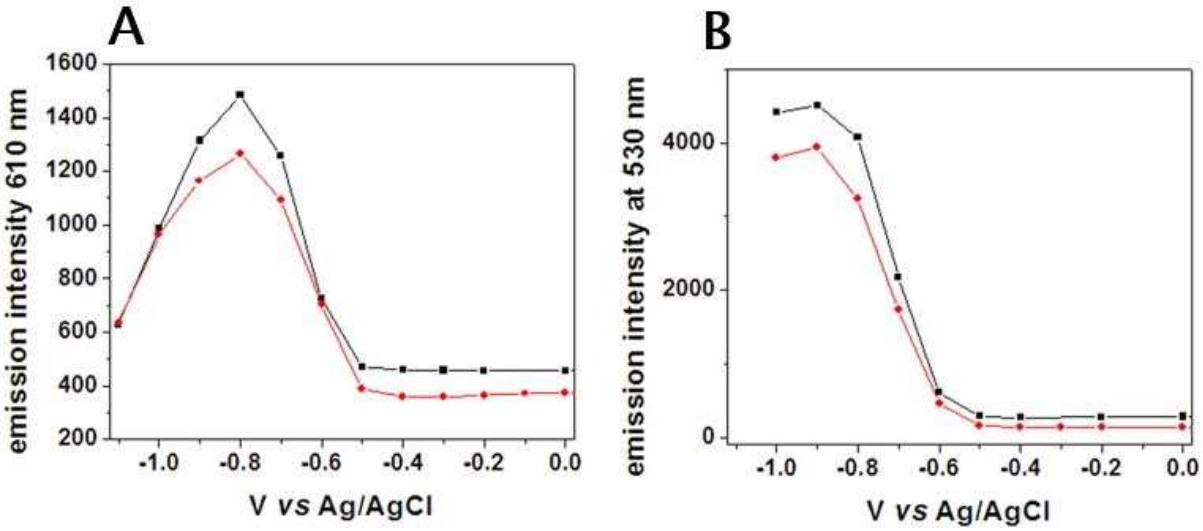

Figure 1.14: Photoluminescence intensity as a function of applied voltage for anatase (A) and 75% anatase 25% rutile mix (B) with (red) and without (black) $TiCl_4$ treatment. Figure adapted with permission from Ref [81].

$TiCl_4$ treatment for enhanced device efficiency has been restricted to quantum dots[87,88], mesoporous TiO_2 nano-structures[89] and TiO_2 nano-rod arrays, as well as halide perovskite[90], while chemical passivation effects on photonic crystals is relatively unexplored, only being reported for dye-sensitized solar cells fabricated from TiO_2 inverse opals[91].

1.8. Objective

Our objective is to improve upon the hybrid organic-inorganic bulk heterojunction P3HT:TiO_2 nano-composite system previously prepared and produce functioning solar cell devices by addressing issues pertaining to surface quality and morphology of the photoactive layer. The bulk heterojunction is prepared by spincoating P3HT over TiO_2 inverse opal. In our device the P3HT:TiO_2 nano-composite would function as the photoactive layer, with P3HT and TiO_2 functioning as the donor and acceptor species, respectively. Improvements in film quality will be achieved by fabricating TiO_2 inverse opals via the co-assembly of polystyrene spheres (of diameters 177 nm and 140 nm) with the water stable TiO_2 precursor in order to reduce the surface cracking associated with vacuum-assisted infiltration techniques. Changes in charge transfer and charge carrier lifetime were monitored using photoinduced absorption spectroscopy (PIA) as a function of $TiCl_4$ treatment, the solution concentration from which the P3HT is cast, and donor acceptor architecture by functionalization with PCBM. We hypothesize that passivation treatment will increase the contact between the TiO_2 and P3HT and will alter polymer ordering at the donor:acceptor interface due to additional TiO_2 deposition from $TiCl_4$ hydrolysis, resulting in larger polaron absorption, shorter polaron lifetimes, and that the inclusion of PCBM will enhance charge separation. Potential changes in crystallite size, the increase of which is known to enhance charge separation via delocalization of charge transfer states over the crystallite, with passivation treatment would be determined by X-ray diffraction. Wall-thickness was measured using scanning-electron microscopy (SEM) and changes in stopband position were measured using reflectance spectroscopy. Changes in polymer ordering were measured by subtracting the absorptance of the P3HT-TiO_2 nano-composite from the bare TiO_2. We hope this work will assist in the rational design of hybrid organic-inorganic nano-composites for solar cells applications.

Chapter 2. Fabrication of passivated inverse opal nano-composites

TiO_2 inverse opals were fabricated by co-assembling polystyrene spheres with a water-soluble TiO_2 precursor, diammonium dihydroxybis[lactato(2-)-O1,O2] titanate(2-)[92–94] (also called Titanium (IV) bis(ammonium lactato)dihydroxide by the chemical supplier Sigma-Aldrich), herein denoted as TiBALDH, or by infiltration of the void spaces in a polystyrene colloidal crystal film with titanium butoxide ($Ti(ButO)_4$)[73,65]. In both the co-assembly method and the infiltration method capillary forces resulting from solvent evaporation allow polystyrene spheres to spontaneously assemble into a FCC array. The resulting film is composed of polystryrene and air in the case of the infiltrated samples or polystyrene and an equilibrium mixture of monocrystalline TiO_2 and the water stable unhydrolyzed TiO_2 precursor (TiBALDH) in the case of co-assembled samples. The equilibrium for nanocrystalline TiO_2 production from TiBALDH hydrolysis is shown below[95].

$$3[Ti_4O_4(Lactate)_8]^{-8} + 8NH_4^+ \rightleftharpoons 8[Ti(Lactate)_8]^{-2} + 4TiO_2 + 8NH_3 + 4H_2O$$

The effect of matrix infiltration and co-assembly on the quality of the resulting IO is shown in **Figure 2.1.**

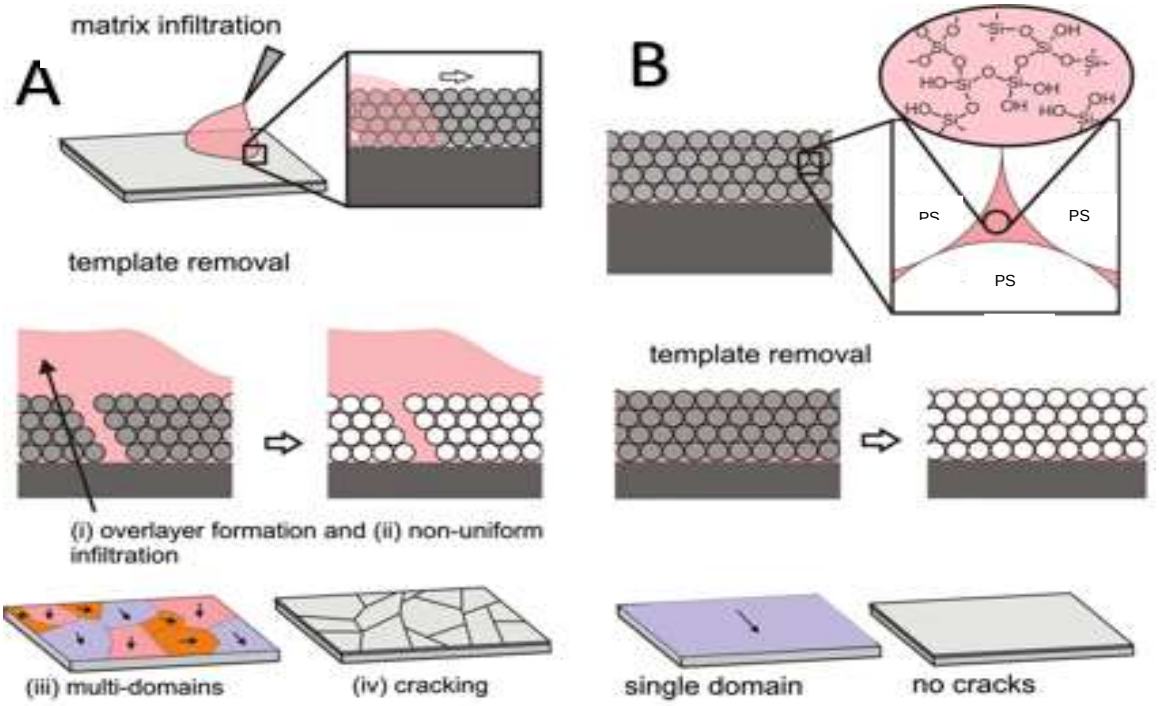

Figure 2.1: Comparison of film quality for IO prepared by infiltration with a metal alkoxide precursor (A) and by co-assembly of a colloidal solution with a water-stable metal oxide precursor (B). Adapted with permission from Ref [94]. Copyright 2010 National Academy of Sciences.

In the co-assembly method a metal hydroxide precursor is mixed in with the solvent. Evaporation of water also induces the formation of FCC array with cross linked hydroxide precursor occupying the void spaces. Fabrication of inverse opals using the infiltration method formation of inverse opal films is generally difficult to achieve structural uniformity over length scales beyond ~50 μm due to under- or over-infiltration, which causes either structural collapse and cracking, or over layer formation[94] shown in **Figure 2.1 A**. Combustion of polystyrene spheres during calcination can also introduce irregularities into the inverse opal. Cracking results due to the high capillary forces associated with the infiltration of the precursor into the high-curvature pores of the fragile colloidal crystal. Unlike possible defects arising from combustion of colloidal spheres, which are unavoidable, cracking due to infiltration by the precursor can be avoided by removing the infiltration step altogether. **Scheme 2.1** shows our fabrication scheme for inverse opals as prepared from infiltration of a polystyrene template from $Ti(OBut)_4$ (A) and by co-assembly of TiBALDH with polystyrene (B).

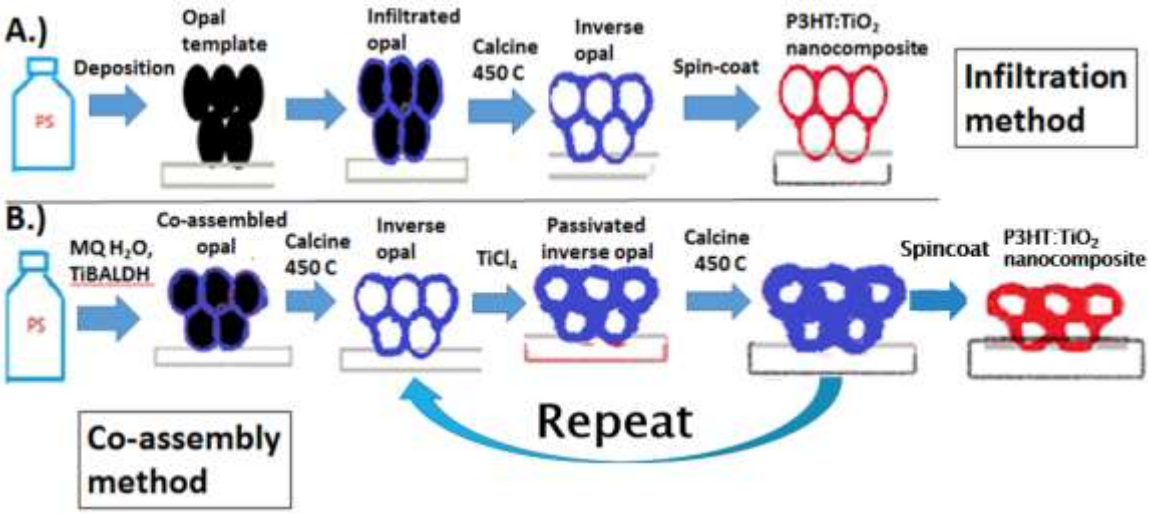

Scheme 2.1: Outline of infiltration and co-assembly methods including passivation treatment and spincoating.

2.1. Experimental

2.1.1. Synthesis of polystyrene spheres

A 250-mL three-necked flask was filled with 100 mL of MQ-H_2O and 15 mL of 95% anhydrous ethanol. The initiator was added through the central neck while the remaining necks were used for nitrogen inlet and outlet lines, the outlet being fixed with a bubbler to measure the nitrogen flow rate (2 bubbles per second). A magnetic stir bar was added, and the flask was immersed in a silicone oil bath set onto of a hotplate and heated to 75.8 °C. The solvent system was purged with a nitrogen needle line for 2 hours, after which the needle was left above the solution during the course of the synthesis. Once the temperature of the bath equilibrated to 75.8 °C the reagents were then added in the order of styrene sulfonate, followed by styrene monomer, and then APS initiator last. APS was weighed out in a dark environment to prevent light from initiating formation of radicals.. Styrene monomer was weighed out in a volumetric syringe and delivered through rubber without exposing the solution to the atmosphere. The solution was left to react for 12 hours. The resultant emulsion was filtered with glass wool previously boiled in water. Sphere diameter was controlled by varying the volume of surfactant delivered[96].

2.1.2. Infiltration and co-assembly method for producing TiO_2 inverse opals

TiO_2 inverse opal photonic crystals were prepared by an optimized co-assembly method adapted from Davis *et al*[11]. Microscope slides, cleaned with 3:1 mixture of H_2SO_4 to H_2O_2 by volume for 1 hour, were thoroughly rinsed with iso-propanol and inserted in vials containing a mixture of 0.21 mL of 140-nm polystyrene spheres, 30 µL of a 10 vol % TiBALDH (Sigma Aldrich) solution, and 5.76 mL of milli-Q H_2O (MQ H_2O). Comparatively, samples of 177 nm sphere size were co-assembled using 0.27 mL of polystyrene spheres, 21 µL of TiBALDH and 5.71 mL of MQ H_2O. Solutions were sonicated for 1 minute. 240 nm samples were also prepared using 0.7 mL of PS, 5.3 mL, and 100 uL TiBALDH. 265 nm samples were prepared using 0.7 mL PS, 5.3 mL, and 95 uL of TiBALDH. Co-assembly was carried out at 60 ^oC in an oven in the presence of a 0.01% solution of NH_4OH. After two and a half days, films of large-area, highly ordered polystyrene spheres crystallized in a face centered cubic (fcc) array with void spaces occupied by unhydrolyzed TiBALDH precursor were obtained. Opals that were infiltrated through vacuum assisted methods were prepared by inserting cleaned glass slides into a vial containing polystyrene spheres with 95% anhydrous ethanol mixture. The samples were heated at 60 ^oC for two and a half days. The void spaces of the resulting opals were infiltrated with titanium butoxide ($Ti(ButO)_4$) via vacuum assisted infiltration. The co-assembled and infiltrated opals were calcined at 450 ^oC for 7 hours and 12 minutes hours with a ramp speed of 1.04 ^oC/min.

2.1.3. Passivation of inverse opals using $TiCl_4$

Aqueous $TiCl_4$ (Sigma-Aldrich) solutions were prepared in a purged glove bag under a nitrogen atmosphere based on a procedure adapted from Lee *et al*[76]. A 2 M stock solution was prepared within the glove bag by withdrawing 0.22 mL $TiCl_4$ and injecting it through a seal into a vial with 0.78 mL of frozen water. The stock solution was removed from the glove-bag in order to warm up to room temperature. Diluted solutions were then prepared using the appropriate volume of the stock solution. Samples were then coated with approximately 60 µL of the respective diluted concentration and placed within a water saturated chamber and heated at 70 ^oC for 30 minutes. Samples were removed, rinsed with distilled water and calcined at the same temperatures as co-assembled opal templates except with a 1.5 hour ramp time to 450 ^oC and a 30 minute hold time. The

concentrations of $TiCl_4$ were 0.1 M for 177 nm IO and 0.025 M and 0.05 M for 140 nm IO. Additionally, passivation was repeated twice (at 0.05 M) for 140 nm IO.

2.1.4. Preparation of P3HT solution and spincoating of TiO_2 inverse opals.

Regioregular P3HT (M_w: 50,000-70,000, RR = 91-94%, Rieke Metals) was weighed out in a glovebox and dissolved in dichlorobenzene at 70 °C for 3 hrs to give 7, 10, or 15 mg/mL solutions. Inverse opal samples were cast with 80 µL of P3HT solution and spun coat in a glovebox under nitrogen atmosphere and in the dark for a minute and thirty seconds at 2000 rotations per minute (rpm). Spuncoat samples were stored in a glovebox under nitrogen atmosphere. For inverse opal of P3HT:PCBM/TiO_2, samples were spuncoat with 1:1 mixtures of P3HT:PCBM solutions (PCBM from Nano-C). For inverse opal of P3HT/PCBM/TiO_2, sequential spincoating of PCBM at 2000 rpm followed by spincoating with ethanol at 1,500 rpm for 5 seconds then spincoating with P3HT for 1.5 minutes at 2000 rpm was carried out.

2.1.5. Absorptance, transmittance, and diffuse reflectance spectroscopy

A Perkin Elmer Lambda 950 UV-Vis-Near IR spectrophotometer (Chen group, York Unviersity) equipped with a 150 mm integrating sphere was used to obtain diffuse reflectance spectra for co-assembled TiO_2 inverse opals. Spectra were taken from 800 – 250 nm using a deuterium light source for wavelengths below 319.20 nm and a tungsten lamp for wavelengths above 319.20 nm. Photonic stopband positions of inverse opals were determined by diffuse reflectance spectroscopy (DRS). Absorptance was measured by placing the sample in the center of the integrating sphere where both total reflectance and total transmittance are measured simultaneously.

2.1.6. Scanning electron microscopy

Scanning electron microscopy (SEM) using an FEI Quanta 3D dual-beam (York University) was used to characterize the sample surfaces. Images were taken under high vacuum with a chamber pressure of 1.45 x 10^{-4} Pa and working distances between 7 and 10 mm. 25 kV electrons were scanned across the sample surface with a specimen current of -0.52 pA. An Everhart-Thornley detector (ETD) was used to measure back-scattered electrons. SEM image analysis by Image J was performed for all sample images.

2.1.7. Reflectance microscopy

Reflectance images were obtained using a Nikon eclipse TE 2000 equipped with a ProgRes® camera (Jenoptik Optical Systems Inc.). Images were taken at 15 X magnifications and with integration times of 10 ms.

2.1.8. X-ray diffraction

Wide angle X-ray diffraction (XRD) patterns ranging from 2θ values of 20 to 50 degrees were measured using a Bruker D2 phaser (Ozin group, University of Toronto) equipped with a Cu Kα1 source (λ=0.15406 nm) operating under step scan mode at 30 kV and 10 mA for a total power output of 300 W. Samples were obtained with an acquisition time of 6.66 minutes. 140 nm sample was prepared from ten 25 layer samples whereas the infiltrated powder was prepared from approximately 30 samples assembled from various sphere sizes ranging from 140 to 375 nm.

2.1.9. Raman spectroscopy

An Advantage 785 benchtop Raman spectrometer from SciAps Inc (Kiteav group, Wilfred Laurier University) with a laser operating at 785 nm with a power of 60 mW was used to collect Raman spectra. Spectra for the 0.05 M and the 0.05 M x2 $TiCl_4$ treated IO powders were collected at an integration time of 5 and 10 seconds, respectively, and were averaged from 10 scans with high smoothing applied.

2.2. Results and discussion

2.2.1. Optimization of opal co-assembly and vacuum assisted infiltration

Opal template thickness was controlled based on a model developed by Nagayama *et al* shown in equation 2.1 The number of layers of the colloidal crystal, k, is related to the sphere diameter (d), the volume percent of the colloids (ϕ), the solvent meniscus height (L), the velocity of the particle with respect to the solvent (β), which is taken as 1, and the volume percent of the solvent (1-ϕ). The 0.605 is a factor taking into account hexagonally arranged spheres on a substrate[97].

$$\boldsymbol{k} = \frac{\boldsymbol{\beta} * \boldsymbol{L} * \boldsymbol{\phi}}{\mathbf{0.605} * \boldsymbol{d}(\mathbf{1} - \boldsymbol{\phi})} \qquad \text{Eqn (2.1)}$$

The thickness of the opal template can be experimentally determined by SEM[98] or optical spectroscopy[99].

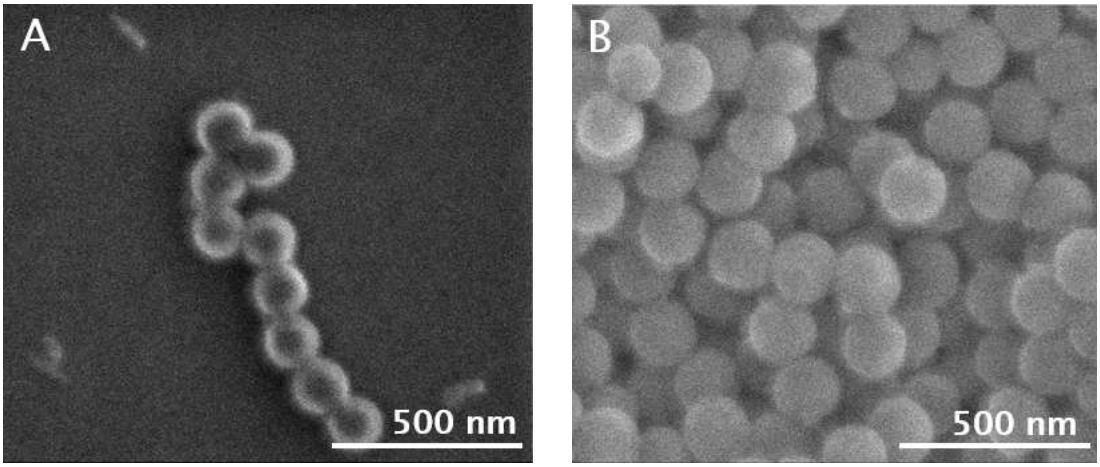

Figure 2.2: Scanning electron micrographs for 149 nm (A) and 183 nm polystyrene spheres (B). Scale bars are noted as insets for each image.

Polystyrene spheres (PS) were fabricated as colloidal suspensions by a surfactant-free emulsion polymerization scheme proceeding by a free radical mechanism of styrene monomer with an ammomium persulfate ($NH_4S_2O_8$, APS)) initiator, with styrene sulfonate acting as a surfactant[96,100]. **Figure 2.2** shows the SEM images of two

batches that were used in this study, with sphere diameters of 149.1 ± 3.4 nm (A) and 182.6 ± 5.6 nm (B). Sphere diameters were measured using Image J software. The quality of the opal template depends on the polydispersity of polystyrene sphere diameter. Batches with large polydispersity will cause assembly of uneven opal films. Spheres are considered to have low polydispersity if the standard deviation of the diameter is less than 5 %[101].

Although SEM is the most definitive and direct method for sphere diameter measurement, reflectance spectroscopy can also estimate sphere diameter in a non-destructive manner based on the wavelength of the Bragg peak, or the photonic stopband [100]. Scalar-wave approximation is used to simulate the optical spectra by modeling the refractive indices of the materials and the sphere size (Equation 4). The opal templates of the spheres shown in **Figure 2.2** have stop bands at 360 nm and 460 nm, and optical simulation suggests the diameters are 140 and 177 nm.

In co-assembled opals, the interstitials of the cubic closed-packed spheres are occupied by the TiO_2 precursor. The reflectance spectra of 140 and 177-nm co-assembled opals are shown in **Figure 2.3.** The stopbands are located at 366 and 451 nm for opals co-assembled from 140 and 177 nm diameter spheres, respectively[102]. The increase in reflectance from 800 to 375 nm arises from Rayleigh scattering[103]. Interference of Rayleigh scattering with photonic properties has been documented in materials composed of small crystallites[104]. The stopband intensity for the 140 nm sample exhibits higher intensity than other sizes due to higher random scattering at short wavelength.

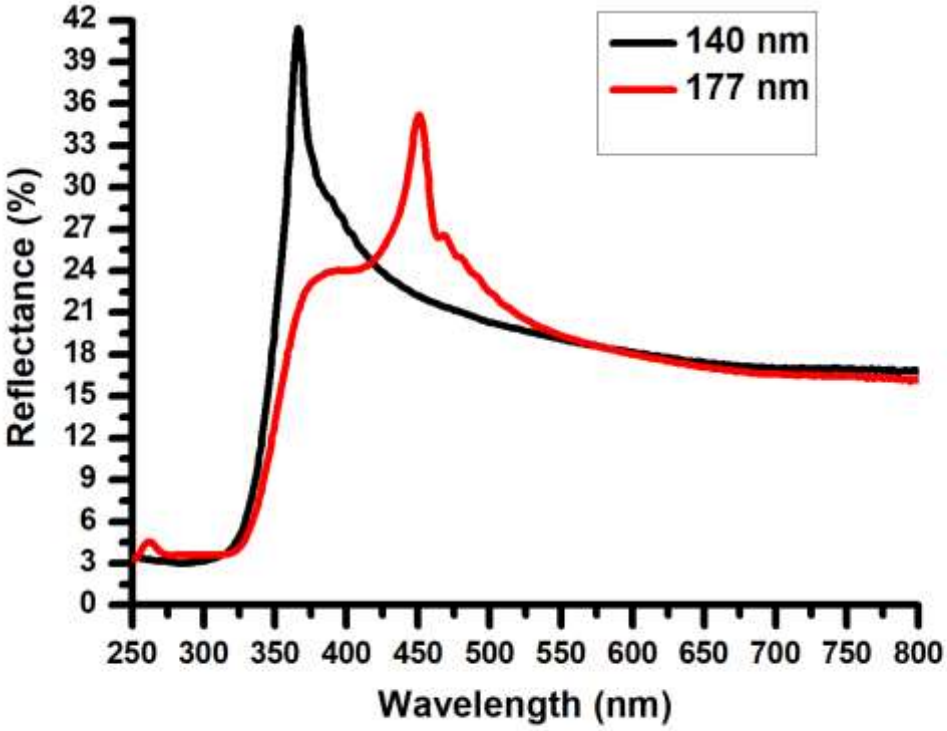

Figure 2.3: Reflectance spectra for co-assembled opals fabricated from 140 nm (black) and 177 nm (red) polystyrene spheres. Each samples were co-assembled using 1.7 vol% TiBALDH solutions.

Below 350 nm – energies higher than the electronic bandgap of TiO_2 – the inorganic material absorbs and a significant decrease in reflectance is observed.

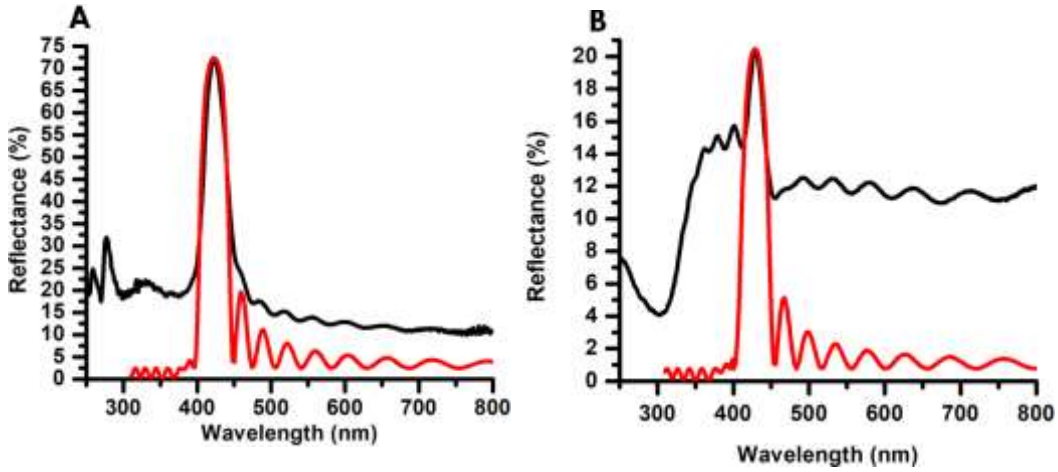

Figure 2.4: Reflectance spectra for a 18 layer 177 nm opal prepared by self-assembly in ethanol (A) and co-assembly with TiBALDH (B). Black lines correspond to experimental reflectance and red lines correspond to simulated reflectance using the SWA.

Figure 2.4 shows the experimental and simulated reflectance spectra of polystyrene opal template (A) and co-assembled opal with TiBALDH (B). Small features observed at 265 and 241 nm in **Fig. 2.4 A** (black spectra) are higher order bands. In high quality and uniform films, Fabry-Perot fringes on either side of the stopband can be clearly observed. The number of fringes correlate with the thickness of the film, such that the number of layers of spheres in the opal can be accurately simulated using scalar wave approximation (SWA). The SWA method fits simulates photonic features by ignoring the polarization of the incoming electromagnetic field[105]. Structural and optical characterization of inverse opals prepared by either two-step infiltration or co-assembly were carried out.

Upon calcination, organic materials are combusted and amorphous or unhydrolyzed TiO_2 precursor material is crystallized into the anatase phase to yield TiO_2 inverse opals. **Figure 2.5** shows the reflectance spectra of inverse opals from co-assembly in air and in water. The inverse opals exhibit random light scattering which peaks at 350 nm in reflectance spectra, below which TiO_2 strongly absorbs. The photonic stopbands are deep into the absorption region of TiO_2 and are approximated to be at 269 and 287 nm for 140 and 177 nm template spheres respectively (**Fig. 2.5A**). The stopband redshifts upon immersing the film in water as the effective refractive index of the inverse opal increases. **Figure 2.5 B** shows a stopband at 328 nm for 177 nm-sphere

templated inverse opal. The 140 nm IO doesn't exhibit a stopband upon immersion in water because it overlaps with the absorbance feature of TiO_2 which occurs at 325 nm. Reflectance spectroscopy is useful for quantifying the light scattering in a sample based on the intensity of baseline; a common source of scattering results from the cracks in the film[106]. Reduced light scattering is sought after for solar applications since scattering is a common loss mechanism in photoactive materials.,

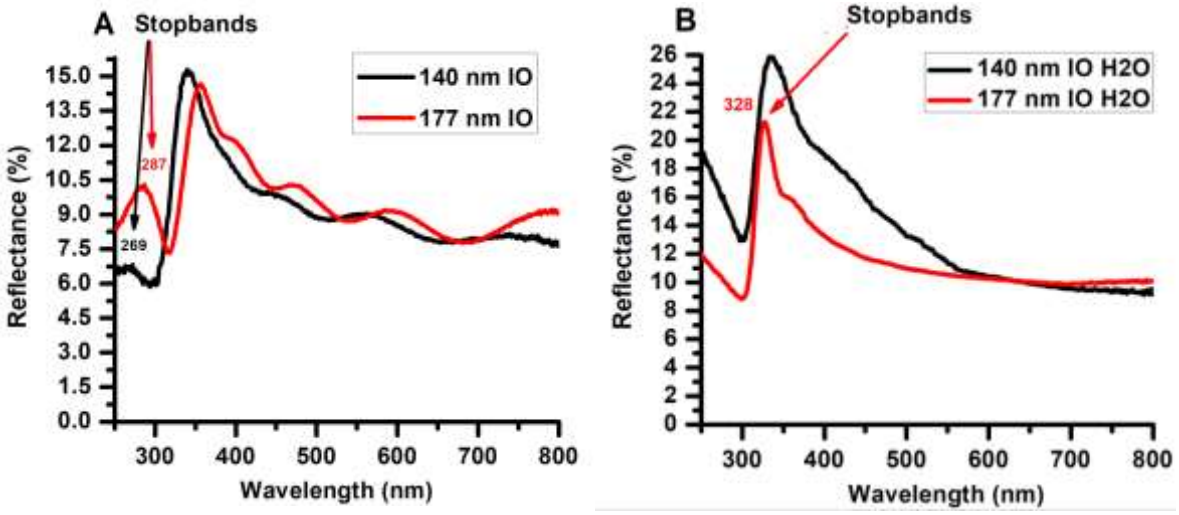

Figure 2.5: Reflectance spectra for inverse opals prepared by co-assembly using various sphere diameters in air (A) and in water (B). Stopband positions are marked by arrows over the respective peaks.

Possible improvement in the structure quality for inverse opals fabricated from co-assembly instead of infiltration can be evaluated by comparing their total reflectance spectra. **Figure 2.6** shows that the inverse opal from co-assembly exhibit much lower background scattering than that obtained from the infiltration method (R of 26% vs 13%, respectively, at 375 nm). The lower Rayleigh scattering for the co-assembled sample relative to the infiltrated sample indicates reduced cracking or deformation in the inverse opal film. The co-assembled sample also yields a discernible stopband at 250 nm for inverse opal templated with 140 nm spheres; this stopband could not be detected in the infiltrated sample.

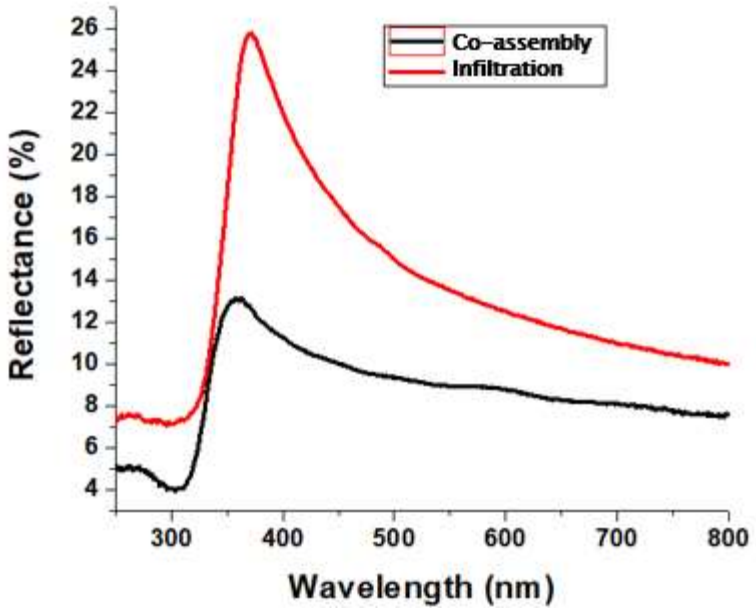

Figure 2.6: Reflectance spectra for 140 nm inverse opals prepared by co-assembly (black) and by vacuum assisted infiltration (red).

A high degree of cracking can be observed in the sample prepared by infiltration, as observed by the smaller domain sizes on the surface relative to the co-assembled sample. Cracking is much more substantial in samples prepared by infiltration due to additional capillary forces acting upon the structure during vacuum assisted infiltration by $Ti(ButO)_4$ [94]. Vacuum assisted infiltration also can lead to the formation of a TiO_2 overlayer, which leads to more flaking and peeling off of the film[64]. **Figure 2.7 B** shows cracking still persists in co-assembled samples due to shrinkage effects during the calcination[64]; however the domain sizes are much larger than infiltrated films.

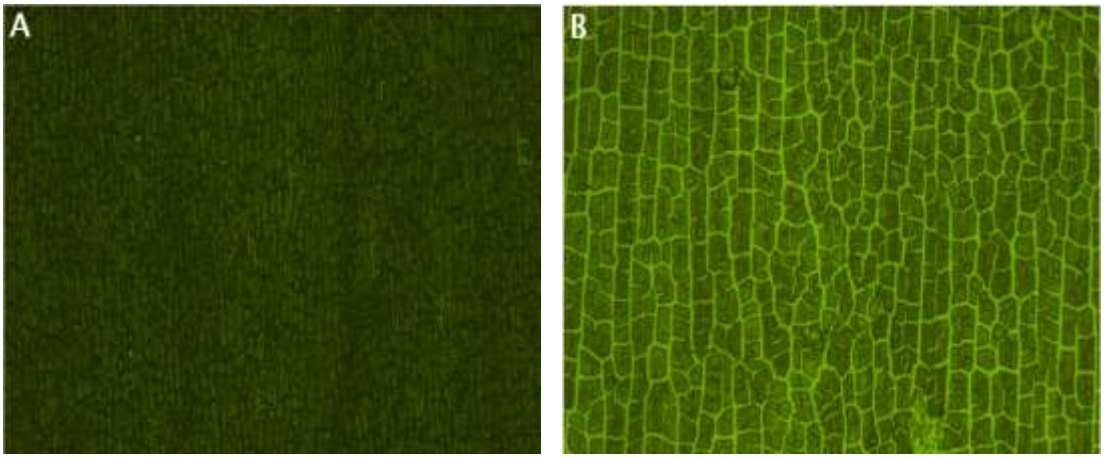

Figure 2.7: Reflectance micrographs of 231 nm IO prepared by infiltration (A) and by co-assembly (B) at 15X magnification and integration times of 10 ms.

Macroscopic cracking and structural defects in the photonic crystal are examined by SEM. Contrasting **Figure 2.8 A** and **B**, enhanced domain size is observed in the co-assembled samples compared to the infiltrated films.

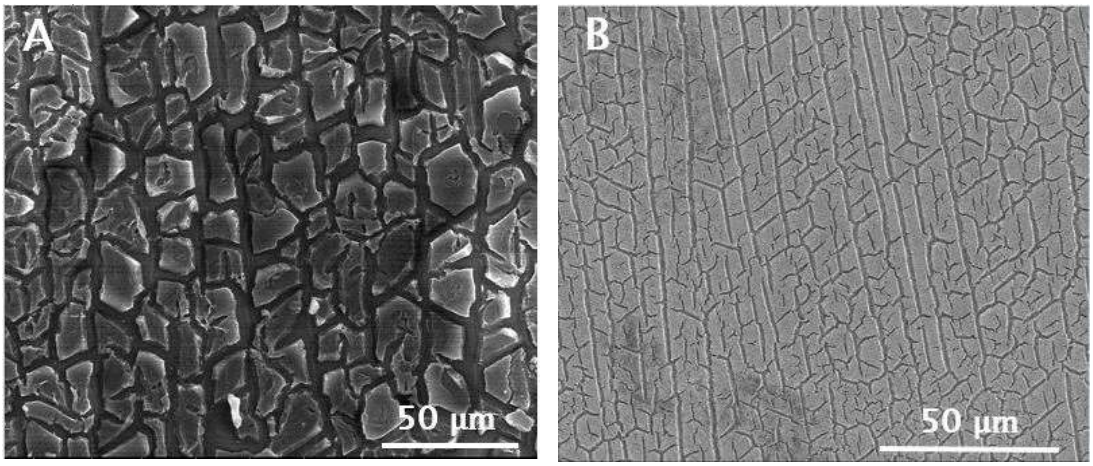

Figure 2.8: Scanning electron micrographs of 177 nm inverse opals prepared by infiltration (A), and co-assembly (B).

SEM images in **Figure 2.9** confirm crystallization in the fcc array during both assembly processes. Colloidal point defects are observed in the infiltrated film (A) while the co-assembled film is relatively uniform. Co-assembled inverse opals also exhibit more uniform sphere positions relative to infiltrated samples, despite both being assembled from the same sphere batch, indicating improved sphere arranged during co-

assembly. Cracking and point defects are of particular concern for photonics applications due the intensity reduction and broadening effects on photonic stopbands[101], which results in more light scattering that weakens photonic effects. Relative to the original PS sphere diameters (140 and 177 nm), the unpassivated inverse opals exhibit void space diameters of 98.0 ± 4.8 nm and 137.9 ±9.1 nm, indicating a 30% and 20% contraction upon inversion. This contraction is in line with previous reports and is expected due to the melting and combustion of polystyrene spheres during calcination[107,108,109].

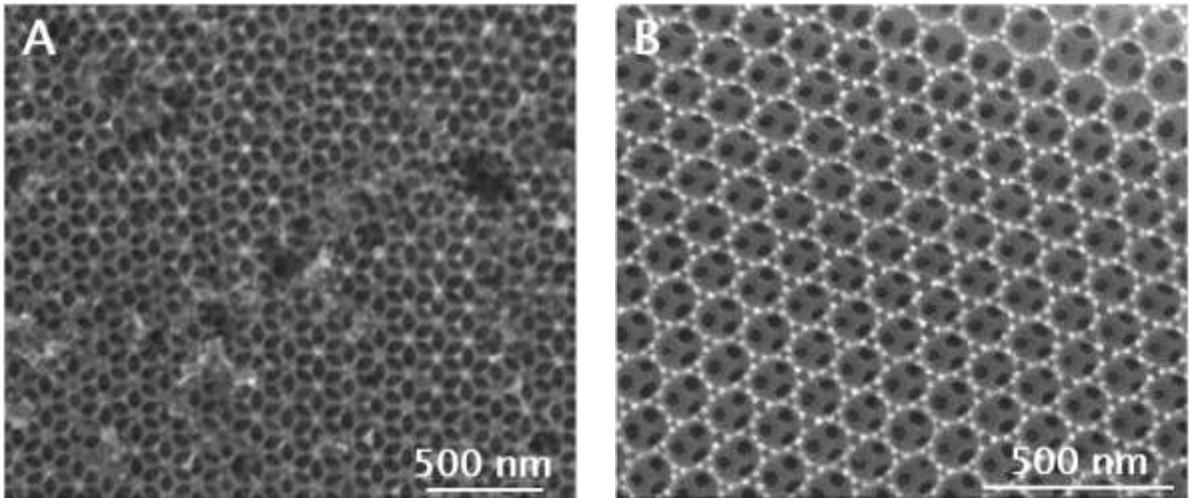

Figure 2.9: Scanning electron micrographs of 177 nm inverse opals prepared by infiltration (A) and co-assembly (B).

The phase, crystallinity and size of the TiO_2 nanoparticles making up the framework are studied by powder X-ray diffraction (XRD). **Figure 2.10** shows the XRD patterns of inverse opals from infiltration vs co-assembly methods. The XRD patterns confirm anatase phase for inverse opals prepared from both methods. The crystallite sizes are estimated using the Scherrer equation in equation 2.2.

$$\boldsymbol{D = \frac{0.9\lambda}{\beta cos\theta}} \qquad \text{Eqn (2.2)}$$

where D is the crystallite size, λ is the source wavelength (0.15406 nm), β and θ are the full-width at half maximum (FWHM) and angle of the Bragg 101 diffraction peak, respectively, in radians[92,110]. The narrowwer FWHM for infiltrated samples compared to co-assembled samples indicates larger crystallite sizes, 18.9 nm vs 5.1 nm [111].

Passivation enhances crystallinity of TiO_2 as observed by the narrowing of the FWHM of the 101 peak (from 2θ of 1.74 to 1.33 upon passivation).

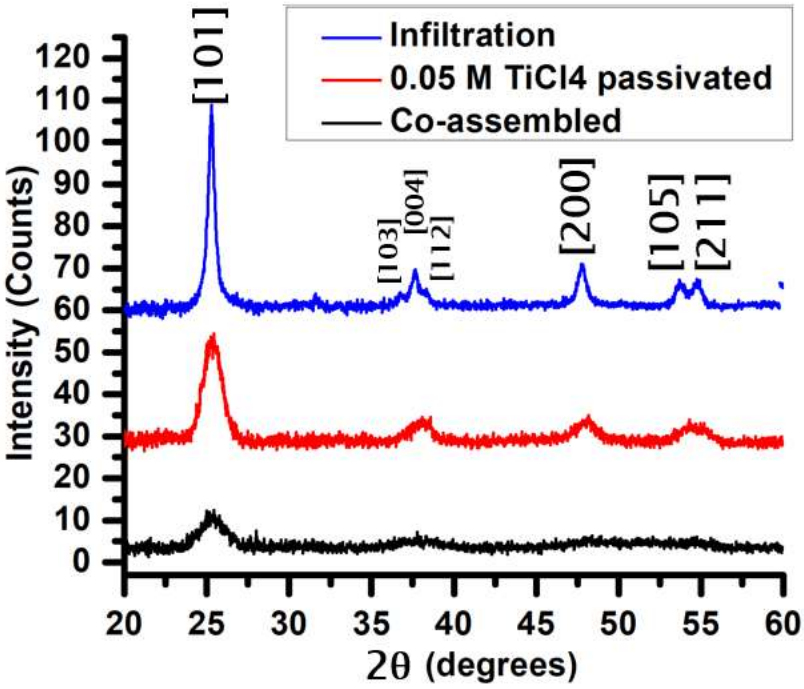

Figure 2.10: XRD patterns for inverse opal powders produced from infiltration of an opal template (blue),by passivation of a co-assembled IO treated with 0.05 M $TiCl_4$ (red), and for a non-passivated co-assembled IO (black). Miller indices corresponding to anatase are noted above each diffraction peak. Diffraction pattern for inverse opal powder prepared from co-assembly and the passivated powder have been multiplied by 10 times.

A summary of XRD parameters for the infiltrated, co-assembled, and passivated powders are presented below.

Table 2.1: Summary of crystallite sizes for inverse opals produced by $Ti(ButO)_4$ infiltration, co-assembly of PS with TiBALDH, and passivated co-assembled inverse opals. FWHM values correspond to the baseline corrected values.

Sample	**FWHM of [101] peak (degrees)**	**2θ of [101] peak(degrees)**	**Crystallite size (nm)**
Infiltration	0.4648	25.27	18.9
Co-assembled	1.74	25.43	5.1
0.05 M passivated	1.33	25.43	6.6

Variation in the crystallite size may arise due to different properties of the TiO_2 precursors. Samples produced by co-assembly of PS spheres with TiBALDH are known to exhibit smaller TiO_2 crystallite sizes due to the water stability afforded by the chelating lactate ligands of the octahedral TiBALDH complex[112]. Alkoxide precursors, such as $Ti(OBut)_4$, exhibit tetrahedral co-ordination of alkoxy ligands around the lewis acidic Ti (IV) center, which is air and moisture sensitive. Solvent effects during infiltration or co-assembly may also influence crystallite size since TiO_2 nanoparticles increase in size with decreasing boiling point of the solvent[113]. Ethanol, with a boiling point of 78.3 ^oC[113], is used during vacuum assisted infiltration of $Ti(OBut)_4$ and has a lower boiling point than water which is used for co-assembly so larger crystallite size for the infiltration method would be expected.

Next we investigate inverse opals from co-assembly process with different passivation conditions. Various $TiCl_4$ concentrations were applied to 177 nm inverse opals to elucidate the dependence of photonic properties on passivation treatment; their reflectance spectra are shown in **Figure 2.11A**. The change in stopband position as a function of passivation treatment is summarized in **Figure 2.11B**. A general redshift in stopband is observed with increasing passivation treatment up to 0.2 M $TiCl_4$ treatment. The red-shift results from the increase in the effective refractive index with additional TiO_2 deposition from the hydrolysis of $TiCl_4$ (see **Scheme 2.1**).

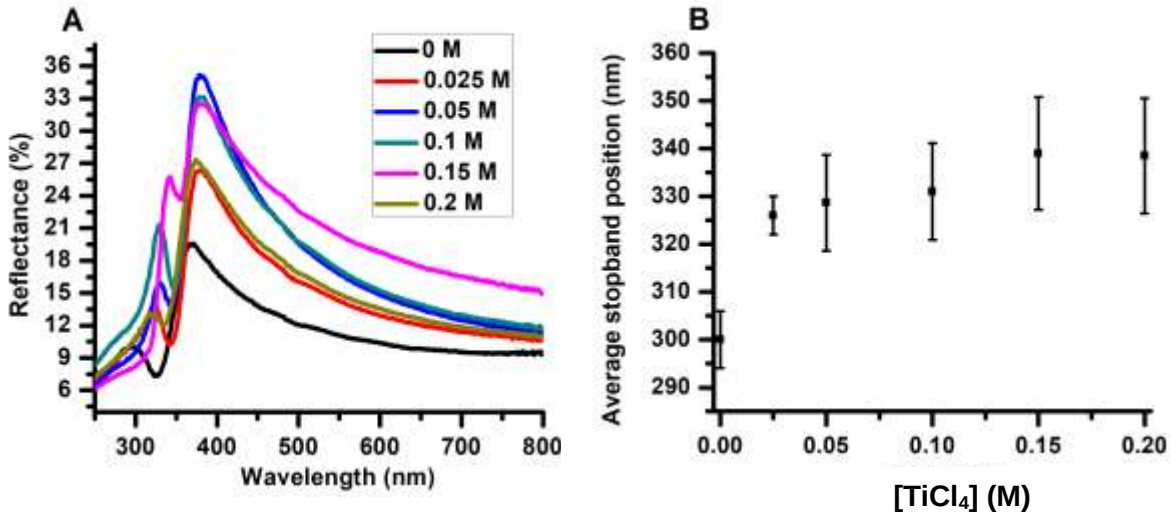

Figure 2.11: A series of reflectance spectra for 177 nm co-assembled inverse opals after various $TiCl_4$ treatments (A.). A summary plot of the average stopband positions obtained from reflectance spectroscopy for inverse opals treated with various $TiCl_4$ concentrations (B). Error bars are reporting in standard deviations of the average stopband position at each wavelength.

Figure 2.12 shows the SEM images of passivated inverse opals; an increase in wall-thickness with increasing passivation treatment, either through increasing $TiCl_4$ concentration or through repeated passivation process, is observed.

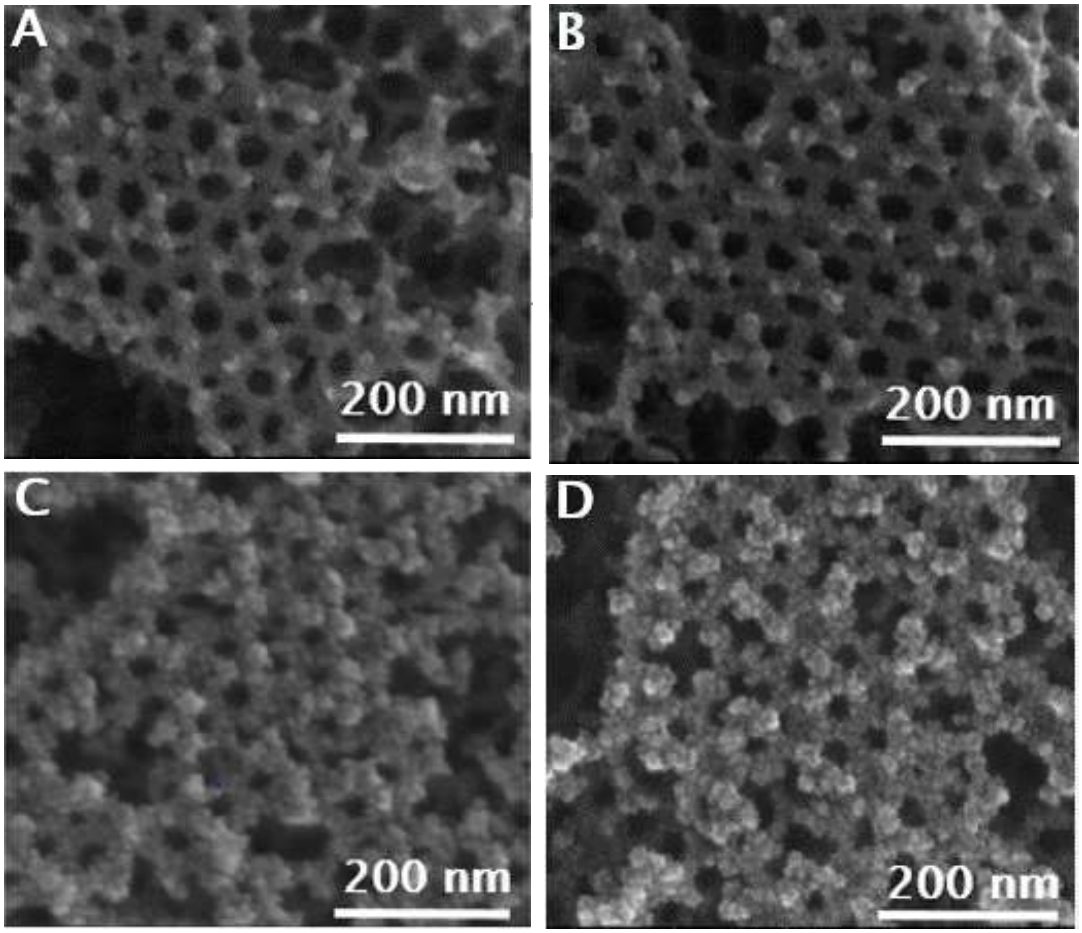

Figure 2.12: SEM images for a series of 140 nm co-assembled inverse opals under the following conditions: non-passivated (A), passivated with 0.025 M $TiCl_4$ (B), passivated with 0.05 M $TiCl_4$ (C), and passivated twice with 0.05 M $TiCl_4$ (D).

Table 2.2.summarizes the thickness of the TiO_2 wall for the different samples templated with 140 nm sphere. The TiO_2 framework increases from 17.1 nm for non-passivated inverse opal, to 20.2 nm and ~28 nm for increasing passivation treatment. The increase in the wall thickness results from the formation of additional TiO_2 shell around the inverse opals walls upon $TiCl_4$ hydrolysis.[91] This increase in the overall effective refractive index of the inverse opal results in the red shift of the stopband in the reflectance spectrum. Note that although the void space becomes smaller with increasing TiO_2 deposition, the periodicity of the inverse opals remain the same as determined by the original un-passivated co-assembled opal. **Table 2.3** shows the air sphere diameter of 177-nm templated inverse opals with and without passivation. A clear reduction in the diameter of the void space and an increase in wall thickness are observed with increasing passivation treatment.

Table 2.2: Summary of the average TiO_2 framework thickness and stopband positions for inverse opals prepared from 140 PS spheres under passivated and non-passivated conditions. Errors are standard error of the means of 60 measurements for each sample.

[$TiCl_4$] (M)	0	0.025	0.05	0.05 x2
Stopband position (nm)	259.1 ± 0.6	267.4 ± 1.7	275.0 ± 1.0	294.0 ± 2.2
Average wall thickness (nm)	17.1 ± 0.4	20.2 ± 0.5	28.4 ± 0.8	29.1 ± 0.5

Table 2.3: Summary of average void space diameter for inverse opals prepared from 177 nm PS spheres under passivated and non-passivated conditions. Errors are standard error of the means of 30 measurements for each sample.

[$TiCl_4$] (M)	0	0.1
Stopband position (nm)	300	330
Average void space diameter (nm)	137.9 ± 9.1	111.9 ± 6.3

While XRD shows only anatase phase of TiO_2, it cannot rule out the possibility of trace amount of rutile. Hence Raman spectroscopy was also employed to compliment XRD measurements by obtaining vibration modes of anatase or potential trace rutile. **Figure 2.13** shows the Raman spectra of inverse opals without passivation and upon repeated passivation. For each sample condition trace rutile could not be obtained and only the anatase phase was observed. Raman spectrum could not be obtained for the non-passivated sample due to limited amount of material and lower crystallinity. The intensity of Raman active bands for the twice passivated samples is about 10 times that

of the single passivated sample due to increased crystallinity of TiO_2. Rutile bands were not observed for either sample, however splitting of the B_{1g} mode was observed. This feature, at 419 cm^{-1}, may arise from the formation of smaller anatase particles which have been known to shift Raman bands to higher wavenumbers due to enhanced force constants by larger, neighboring crystallites[114]. In a previous study that investigated the potential effects of $TICl_4$ treatment on TiO_2 photoluminescence, passivation treatment of purse anatase by $TiCl_4$ did not result in rutile formation, while passivation of a 75%/ 25% anatase/rule mixture resulted in additional rutile formation[84]. In this work the inverse opals are originally in anatase phase and the formation of rutile phase was not detected with $TiCl_4$ passivation which is in line with observations by the McHale group.

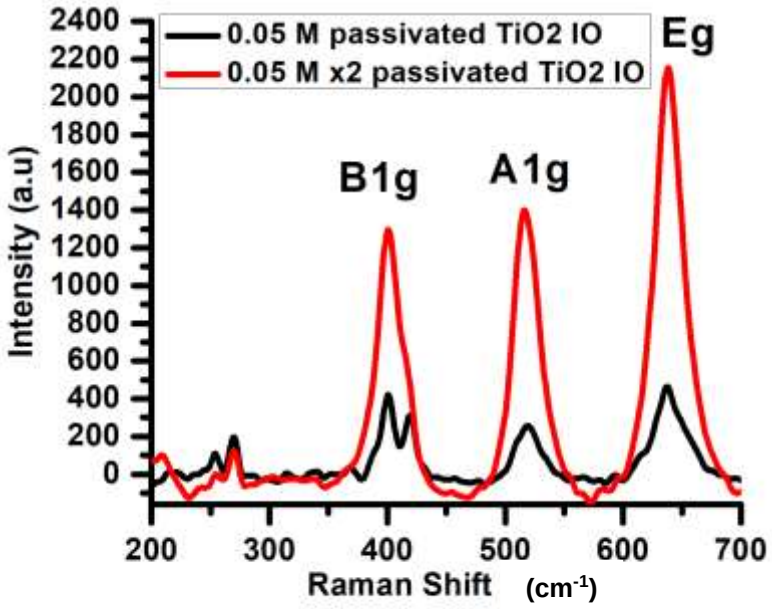

Figure 2.13: Raman spectra for once (0.05 M, black) and twice (0.05 M x2, red) passivated inverse opal films. Each feature is marked with Raman active modes for anatase.

.

2.2.2. Structural and optical characterization of inverse opal nano-composites

We now investigate the morphology and optical properties of P3HT-coated samples. **Figure 2.14** shows the SEM images of 17 and 11 layer unpassivated samples spin-coated with 15 mg/mL P3HT.

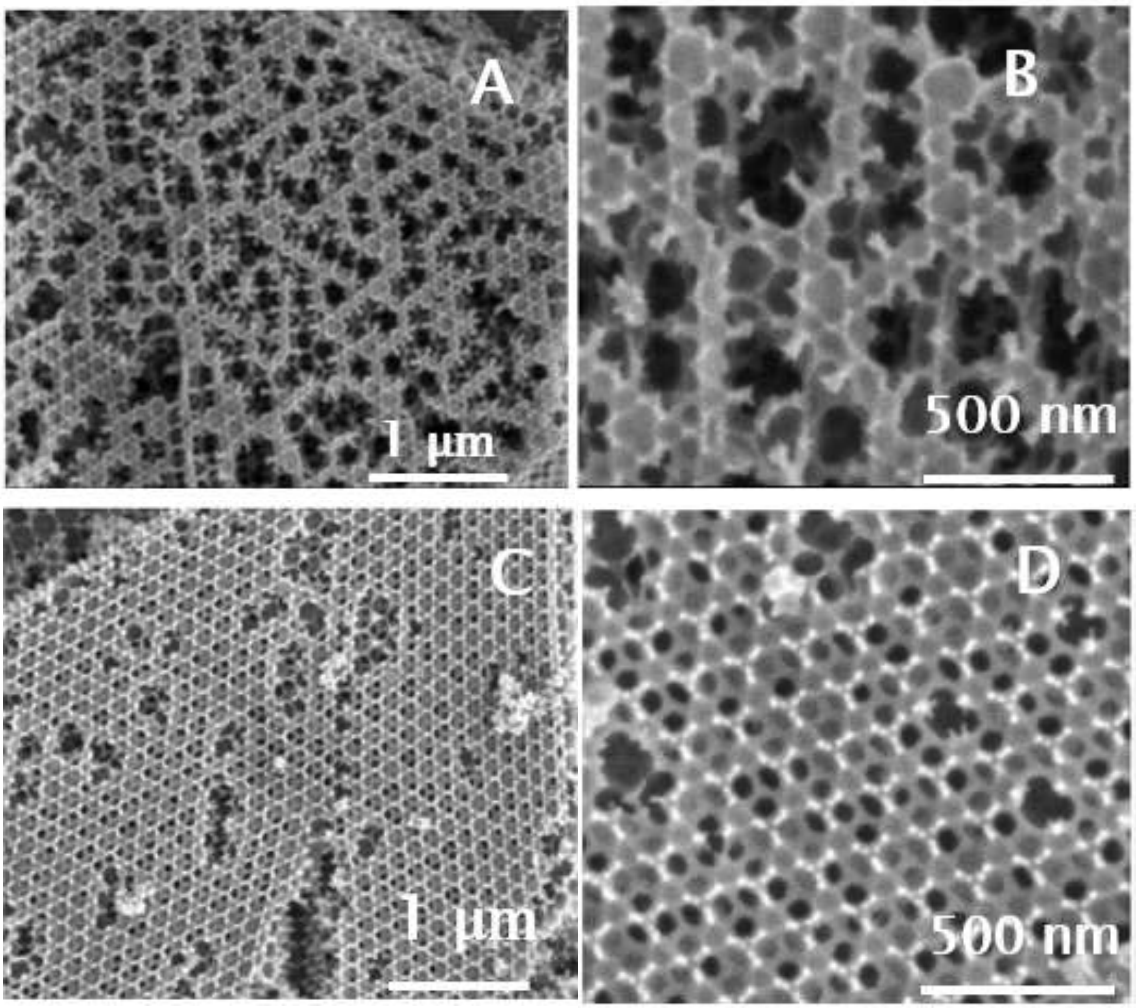

Figure 2.14: SEM images for 11 (A and B) and 17 layer (C and D) 177 nm inverse opal samples coated with P3HT. P3HT concentration was cast with 15 mg/mL.

Extensive void filling by the polymer is observed in thinner samples (A, B) compared to thicker samples (C, D). Thinner samples also appear more damaged compared to thicker samples. Because device engineering for organic photovoltaics requires thinner films, the degree of void filling by P3HT and sample degradation must be minimized. We achieve this by reducing P3HT concentration and characterize the

sample quality optically through reflectance and absorptance measurements. Absorptance was measured by placing the sample in the center of the integrating sphere. The measured light intensity then results from simultaneous measurement of diffuse transmittance and total reflectance. Absorptance (A%) is then calculated by subtracting the total light intensity collected from 100%, 100%-(T_{tot}) = %A[115], where T_{tot} is the total amount of scattered light captured by the integrating sphere. Absorptance can also be calculated by obtaining diffuse transmittance and total reflectance separately, and then subtracting their sum from 100 %. A comparison of absorptance as obtained by the two methods is shown in **Figure 2.15**.

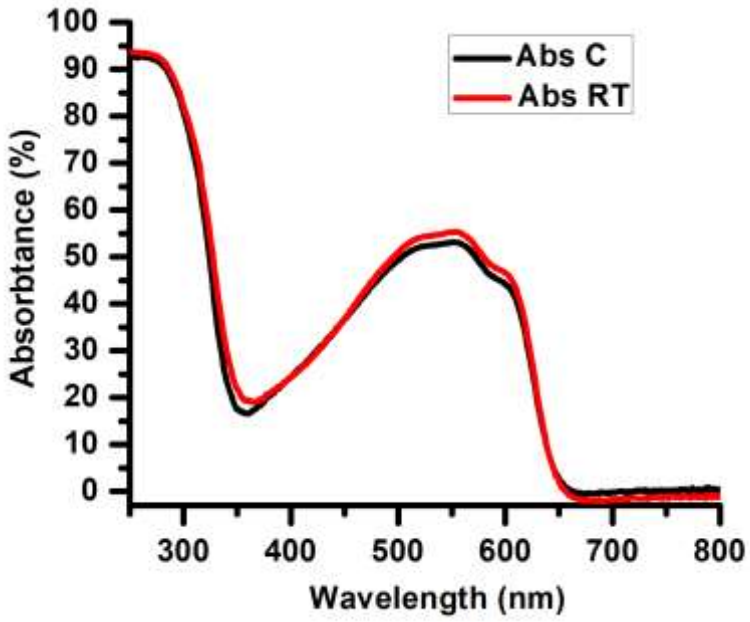

Figure 2.15: Absorptance spectra 140 nm, P3HT cast , 0.05 M inverse opal as calculated by subtracting the total light (T_{tot}, C) captured by the integrating sphere from 100% (black) and calculated by subtracting the sum of the diffuse transmittance and total reflectance (red, RT) from 100%.

Absorptance is similar for both methods. Deviations in absorptance are accounted for by the differences in beam size between reflectance and transmittance measurement modes. Absorptance spectra presented from this point on have been taken by direct measurement (T_{tot}), placing the sample in the center of the integrating sphere.

Figure 2.16 shows the absorptance spectra of 177 nm and 140 nm samples cast with various concentrations of P3HT.

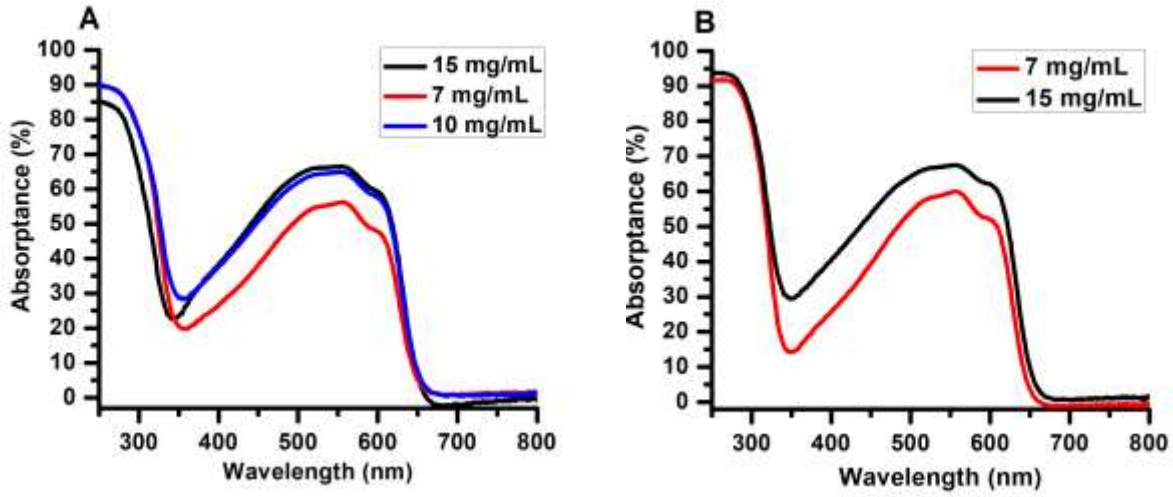

Figure 2.16: Absorptance spectra of 177 nm co-assembled inverse opals (A) cast with 15 mg/mL (black), 10 mg/mL (blue), and 7 mg/mL (red). Absorptance spectra of 140 nm co-assembled inverse opals (B) with 15 mg/mL (red) and 7 mg/mL(black).

The broad feature between 650 and 350 nm, peaking at 550 nm, corresponds to the π-π* transition of P3HT[116], and correlates with the concentration of P3HT, thus the peak decreases with decreasing P3HT concentration. Small peaks near 600, 550, and 500 nm correspond to 0-0, 0-1, and 0-2 vibration transitions of P3HT, respectively[117]. The absorptance onset below 350 nm arises from the electronic band gap transition of TiO_2. **Figure 2.17** shows the reflectance spectra of 177-nm samples before and after P3HT coating:

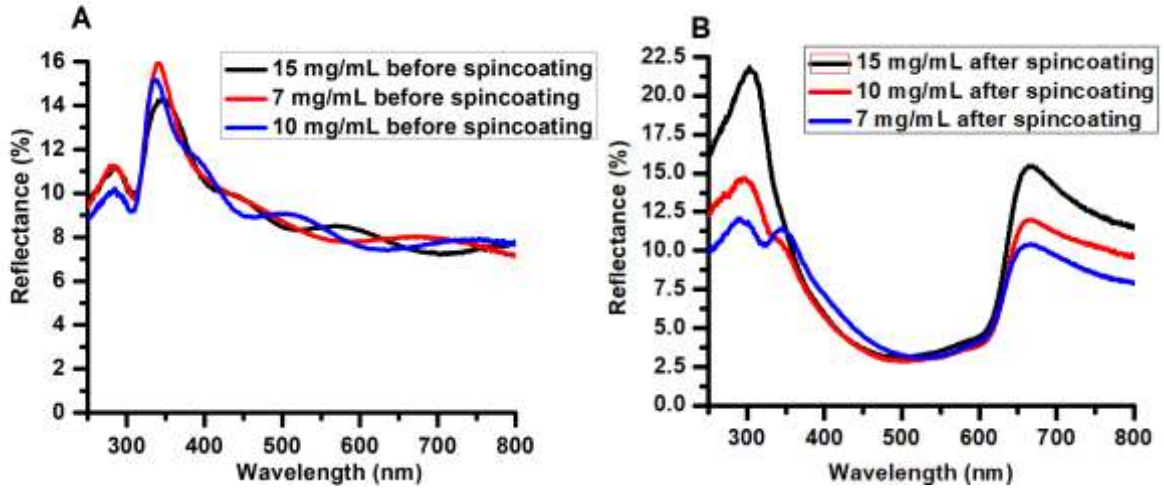

Figure 2.17: Reflectance spectra for 177 nm inverse opals before (A) and after spincoating (B). Each sample was 11 layers thick.

Reflectance spectra are similar between all samples of their respective sizes prior to spin-coating (**Fig. 2.17A**), showing the consistency between sample fabrication. Upon coating with different amounts of P3HT, drops in reflectance between ~375 – 625 nm are due to P3HT absorptance (**Fig. 2.17B**). The stopband intensity increases with increasing concentration of P3HT, which may originate from an increase in the dielectric contrast[118] and an increases in the effective refractive index of the film. Small redshifts are observed consequently upon spin-coating[64]. Rayleigh scattering increased slightly for sample cast with 15 mg/mL P3HT, which could arise from surface roughness and degradation of the morphology as confirmed by SEM. Reflectance parameters are summarized in **Table 2.4** below.

Table 2.4: Summary of reflectance parameters before and after spincoating for 140 and 177 nm co-assembled inverse opals.

Size (nm)	Stopband position before (nm)	Stopband position P3HT (nm)	Stopband intensity before (%)	Stopband intensity P3HT (%)	[P3HT] (mg/mL)
177	284	---	11.26	---	15
	285	296	10.22	14.65	10
	284	291	11.26	12.03	7
140	260	267	4.75	8.33	15
	260	267	5.15	5.85	7

Optical spectra were also obtained for passivated inverse opals cast with P3HT. **Figure 2.18** shows the reflectance spectra for uncoated and spin-cast samples.

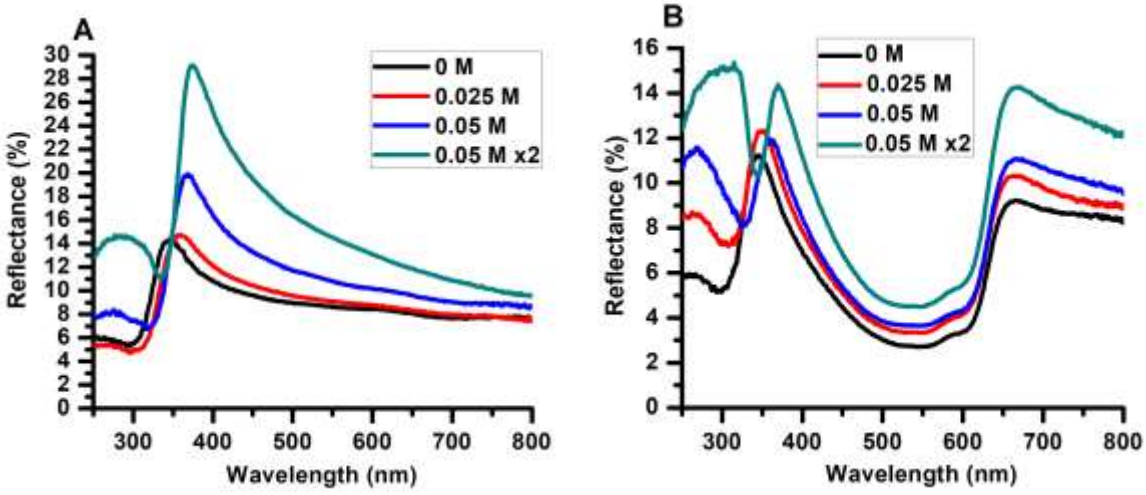

Figure 2.18: Reflectance spectra for inverse opals before (A) and after P3HT coating as a function of passivation treatment (B). Each samples was cast with 7 mg/mL P3HT.

Figure 2.18A shows that increasing passivation treatment induces a redshift in the stopband (~250-290 nm) which also becomes more prominent in intensity in the reflectance spectra. Upon spincoating, the stopband redshifted slightly as shown in **Figure 2.18B.** Slow photons at the red edge of the photonic stopband have been shown to enhance absorption in dyes[119,66] and polymers.[120]. Coupling the absorption onset to the red-edge increases localization of light [121]. This effect may contribute to the enhanced bandedge absorption of TiO_2 for passivated samples as seen in **Fig. 2.19A**.

Potential photonic enhancement or changes in the ordering of P3HT on the IO framework with increasing passivation treatment was evaluated based on the absorptance of the P3HT component of the nano-composites. This was obtained by subtracting the absorptance of passivated TiO_2 prior to spincoating from the total nano-composite absorptance. From this we obtain the absorptance of P3HT in terms of its arrangement within the inverse opal, with all TiO_2 features removed. The spectra are presented in **Figure 2.19**.

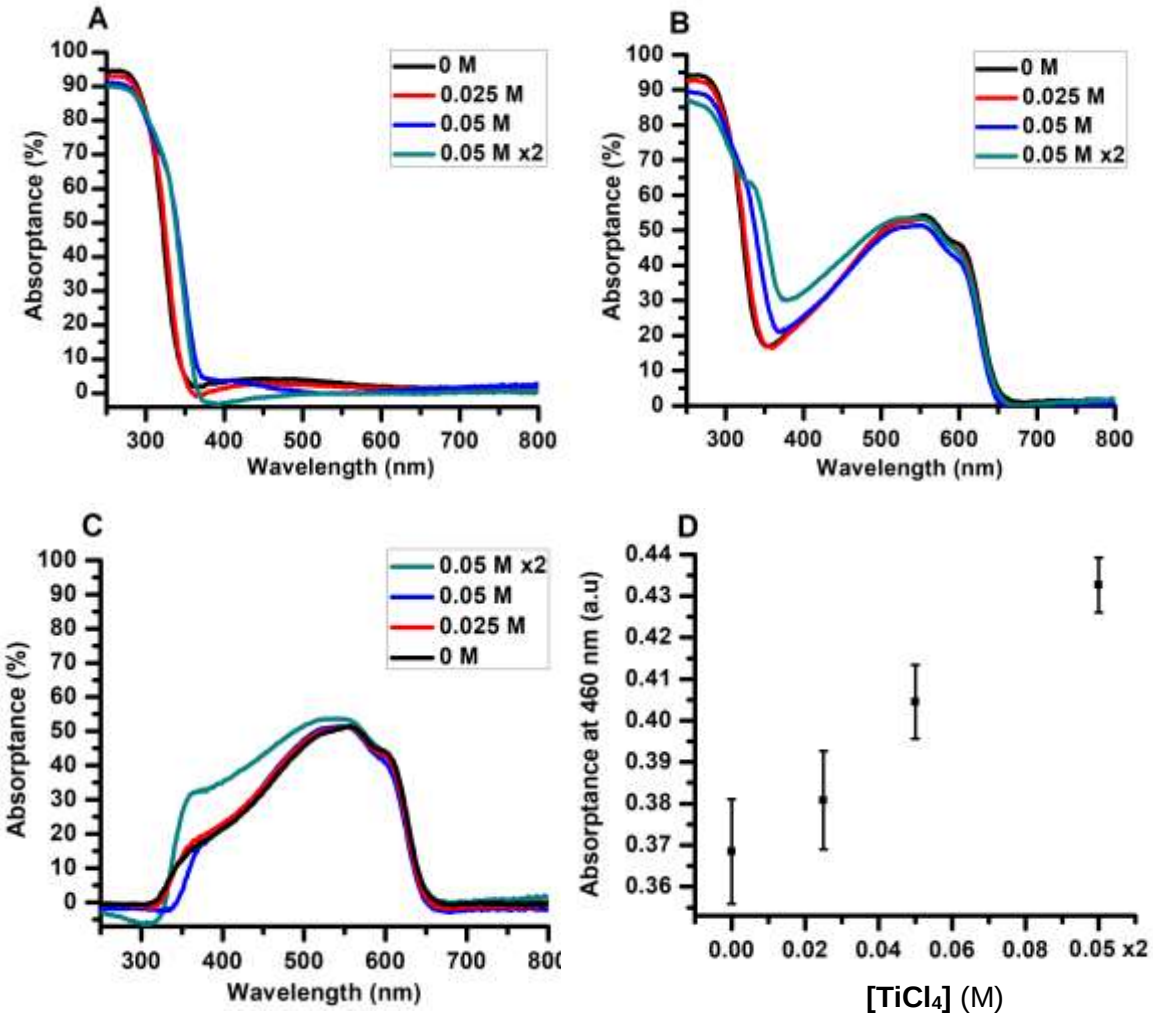

Figure 2.19: Absorptance of passivated TiO_2 inverse opal (A). Absorptance of passivated P3HT:TiO_2 IO nano-composites (B). Absorptance of the P3HT component for passivated P3HT:TiO_2 IO nano-composites (C). Absorptance of P3HT:TiO_2 IO nano-composites at 460 nm as a function of passivation treatment (D). Error bars correspond to the standard error of the mean average from 5 samples.

A broadening of TiO_2 absorptance is observed with increasing passivation treatment in both **Figure 2.19 A and B**. A clear absorption enhancement is seen between 350 and 500 nm for the P3HT component of the twice passivated sample after deconvoluting for the TiO_2 component (**Fig. 2.19 C**). The absorptance intensity at 550 nm is similar between samples so it is unlikely that different P3HT amounts increase absorptance. Nano-composite absorptance at 460 nm, the wavelength of the pump beam used in photoinduced absorption (PIA) experiments, increases with passivation treatment

as shown in **Figure 2.19 D**. Increased absorptance at lower wavelengths (~350 – 450 nm) with respect to the fundamental absorption feature of P3HT as seen in **Figure 2.19 C** results from a higher amount of unaggregated or disordered P3HT in the system[30,]. Blue-shifting in P3HT absorbance has been observed with increasing disorder when transitioning from single-crystal to film to solution based P3HT samples[117] and increased absorbance at lower wavelengths has also been reported for P3HT films cast on rough surfaces such as inorganic nanoparticles[122,123] and has also been observed for P3HT coated over 3D IO previously studied in our group [73]. We hypothesize that increased surface roughness in passivated samples increases the amount of un-aggregated P3HT on the nano-composites. Potential slow photon effects on the absorptance of the polymer should be minimal as the enhancement bandwidth is relatively narrow and the stopbands are far away from 460 nm – the excitation wavelength employed for probing polaron absorption in photoinduced absorption (PIA) experiments. PIA spectroscopy as a function of passivation treatment, P3HT concentration, and donor composition will be discussed in the following chapter.

Chapter 3. Photoinduced absorption spectroscopy

3.1. Phenomenon and principle of operation

Photoinduced absorption spectroscopy (PIA) is a technique used to measure the absorption spectrum of short-lived transient species with lifetimes greater than 10 μs[124]. It is a pump-probe technique that measures the absorbance of photoinduced sub-band gap states[125] upon exciting a sample into a transient state (pumping). PIA has been used extensively to characterize exciton and charge-carrier dynamics of electron-donating polymers in bulk-heterojunction solar cells[126,127,], recombination kinetics of oxidized dyes with injected electrons in dye-sensitized solar cells[128], and electron injection into metal oxides in quantum dot sensitized solar cells[129,124]. PIA can be performed using light sources of similar intensity as sunlight, in contrast to other pump-probe techniques, such as laser flash photolysis (LFP), which require higher light intensities[128].

For polymer solar cells, the use of PIA to measure charge carrier production relies critically on the mechanism of polaron formation. An exciton in a polymer can be produced by exposing the polymer to photons of energy equal to or larger than the HOMO-LUMO energy gap (i.e. 2.0 eV in P3HT[41]). Once the exciton diffuses to the donor-acceptor interface, the electron transfers from the LUMO of the donor (polymer) to unoccupied states of the acceptor (e.g. conduction band of a metal oxide), and the polymer is oxidized into a radical cation species. Oxidation leads to the formation of polaron states through the reorganization of the polymer backbone into a quinoid-like structure. Intermediate energy levels between the HOMO and LUMO of the polymer result, with an energy gap of 1.25 eV or 1000 nm in P3HT[130], corresponding to the P^* transition as shown in **Figure 3.1 B**. Additional transitions between the HOMO and the low energy (LE) polaron state (P_1 transition, 3600 nm, 0.34 eV) and between the HOMO and high energy (HE) polaron state (700 nm, 1.77 eV) can also be probed[131].

Furthermore, polaron states can be delocalized along the polymer axis (one-dimensional, 1D) or between interchain stacks (two-dimensional, 2D)[132]. Polymer stacking leads to the appearance of bipolaron states due to energy splitting of the 1D polaron states[133] with an transition energy of 1.9 ev or 650 nm in P3HT arising from a 0.35 eV downward and upward shift in the LE and HE polaron levels, respectivly[134].

Different transitions and polymer structures in regioregular P3HT[135] are summarized in **Figure 3.1**.

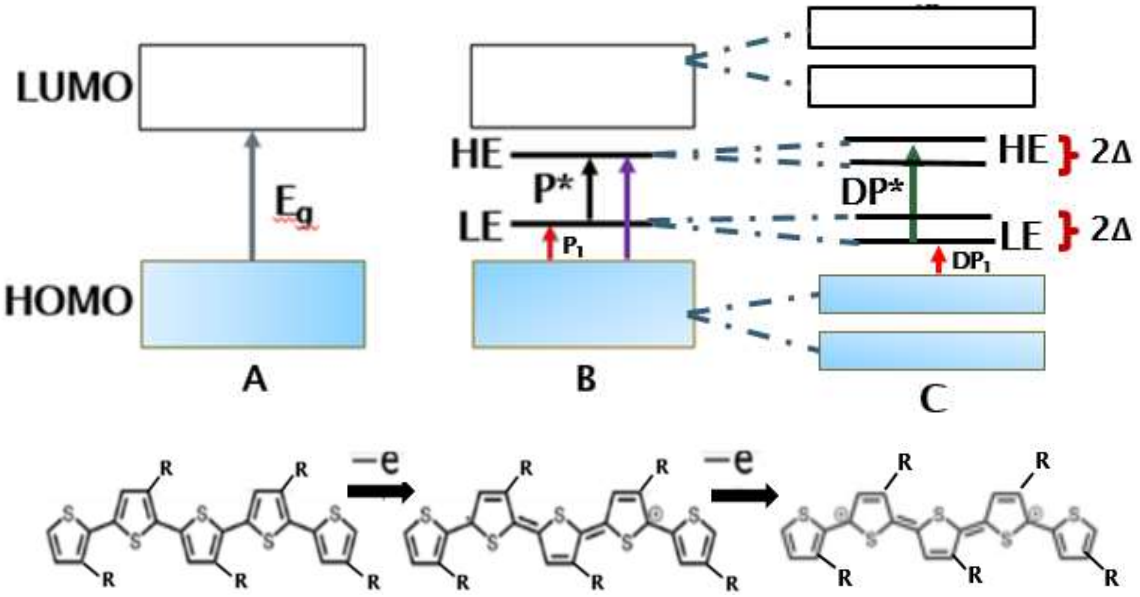

Figure 3.1: Energy level diagrams of ground state P3HT (A), after production of polaron states (B) and after production of bipolaron states (C). Eg refers to the HOMO-LUMO gap of P3HT while P* (black arrow) refers to the energy gap between the high energy (HE) and low energy (LE) polaron states[130]. HOMO to LE and HOMO to HE transitions are represented by red and purple arrows, respectively. Bottom panel shows the relaxation of the neutral P3HT backbone (A, left) into its respective quinoid-like form (B, center) after electron transfer to an acceptor, and bipolaron formation after additional electron transfer (C, right), which results in additional DP_1 and DP* transitions marked by red and green arrows, respectively[131]. R groups represent hexyl side chains (-$CH_2(CH_2)_4CH_3$) of P3HT and Δ is the energy split in HE and LE levels upon bipolaron formation.

Photoinduced absorption spectroscopy was used to determine the absorption of P3HT polarons in inverse opal TiO_2 nano-composites. Excitation was achieved by square-wave modulation of a 460 nm blue LED pump beam operating at 200 Hz. Photoinduced absorption was measured in terms of the differential change in the transmission of the probe beam ($dT = T_{on}-T_{off}$) while the pump flashes on (T_{on}) and off

(T_{off}), as it passes through the sample; the change in transmission is divided by the transmission of the probe beam[136]. The probe beam was also blocked after each reading to correct for extraneous light and dark noise and signals from photoluminescence[137]. Photoluminescence was removed from the spectra by subtracting it from the transient absorption data (dT/T). Spectra were collected at 10-nm interval.

The polaron signal is detected by a lock-in amplifier. The lock-in amplifier operates based on phase-sensitive detection, where the amplitude and phase of a periodic signal is measured in comparison to a reference. It allows the filtering of extraneous signals of differing frequency and noises. The output signal is displayed as two channels, X and Y, with X being in-phase with the pump beam and Y being phase-shifted by 90^{o}. Signals with longer lifetimes appear in the Y channel due to the phase-shift.

An absorption corresponds to a transmittance dip (negative dT/T) in the X-channel[126] and positive dT/T in the Y-channel. The magnitude of total polaron absorption can be determined by taking the vectorial sum of the corrected X and Y channel signals as $R = \sqrt{X^2 + Y^2}$. To account for variable amounts of P3HT on the samples, PIA signal is normalized to the absorptance of the nano-composite at the pump excitation wavelength. An example of a PIA spectrum separated into X and Y channel components and taken as the vectorial sum of the two channels is shown in **Figure 3.2 A and B**, respectively.

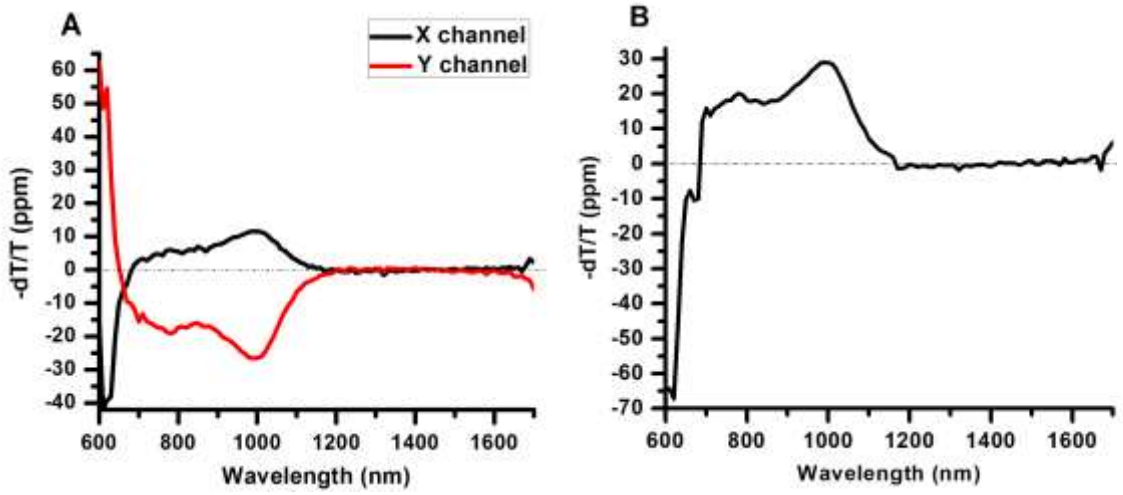

Figure 3.2: Sample PIA spectra showing polaron signals obtain in the X and Y channels (A) and total magnitude calculated by the vector sum (B) for a 140 nm inverse opal with a P3HT concentration of 7 mg/mL.

Polaron lifetimes can be determined by perfoming frequency-modulation experiments – the absorption of polaron at 1000 nm was monitored over 10 – 1000 Hz. [138]. The frequency-dependent polaron signal is then fitted to a dispersive recombination model[134] (eqn. 3.1) where ω is the frequency, $(dT/T)_o$ is the polaron generation at 0 Hz, τ is the mean polaron lifetime and γ is the polaron lifetime dispersion factor. The dispersion factor describes the statistical variation of lifetime values in a sample and can range between 0 and 1, with 0 and 1 signifying non-uniform and uniform polaron lifetime distributions, respectively[126].

$$\frac{-dT}{T} = \frac{\left(\frac{-dT}{T}\right)_o}{1+(\omega\tau)^\gamma} \qquad \text{(Eqn 3.1)}$$

3.2. Experimental

The PIA setup is based on a pump-probe system using a 450 ± 10-nm LED (Luxeon Star Rebel) with 460 ± 24 nm band pass filter as the pump beam and an Oriel APEX 100 W quartz tungsten halogen (QTH) lamp as the probe beam.The pump LED was powered by a Tektronix DC power supply and modulated with a Tektronix arbitrary function generator (AFG2021), at 200 Hz for spectral collection and 10 – 1000 Hz for

modulation-dependent experiments. The LED operated at an intensity of 139 W/m^2 at a modulation frequency of 200 Hz. A silicon/indium gallium arsenide photodiode (Si/InGaAs) detector was used in combination with an Acton monochromator for spectral collection from 600 to 1700 nm at 10 nm intervals with 60 averages per wavelength reading. A Stanford Research System low-noise current pre-amplifier (SR570) and lock-in amplifier (SR830) were used to detect the transient signal from the photodiode. A Keithley 2000 digital multi-meter was used to measure the constant voltage of the photodiode. The phase of the lock-in amplifier was set such that scattered pump light or polymer photoluminescence appeared as a positive value in the x-channel. Additionally a shutter was mounted in front of the probe source to block the probe beam during photoluminescence measurements. An aluminum mask reduced the sampling area to 0.79 cm^2 (1 cm diameter). Measurements were performed under dynamic vacuum since P3HT is susceptible to oxidation.

For lifetime measurements, an InGaAs transimpedance amplified photodetector (Thorlabs PDA10CS) was used in place of the dual-band Si/InGaAs detector. A 900 nm longpass filter was used with the probe beam and pump frequency was modulated between 10 and 1000 Hz. Lifetime measurements were also performed under dynamic vacuum.

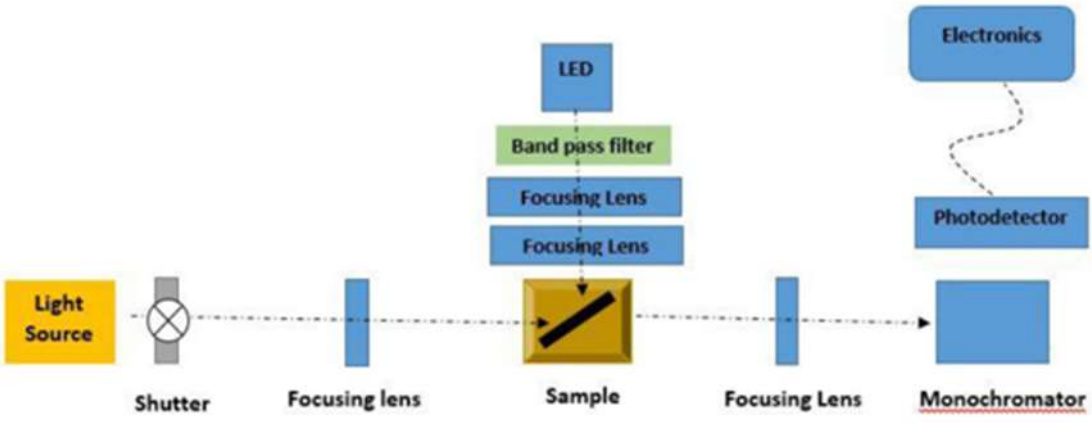

Figure 3.3: Pump-probe spectroscopic setup for polaron generation/detection using a blue LED and a quartz tungsten halogen light source. Black arrow heads with dashed tails outline light paths of the pump and probe beams.

3.3. Results and Discussion

Photoinduced absorption spectroscopy was used to investigate the effect of $TiCl_4$ passivation treatment, donor concentration, and donor composition on polaron absorption, lifetime, and photoluminescence of the inverse opal nano-composites (i-P3HT/TiO_2-o).

3.3.1. Probing the effect of donor concentration on polaron absorption

Due to the short exciton diffusion length of P3HT[40], optimization of donor:acceptor junction thickness is crucial for solar cell performance[139]. In P3HT:PCBM cells, active layer thickness has been optimized by varying rotational speed during spincoating[140], donor acceptor mass ratio[141], interfacial modification[142], and concentration[143]. Supriyanto *et al* evaluated device performances for 1:1 P3HT:PCBM weight ratio films composed of 1,2,8,and 16 mg/mL mass concentrations producing device efficiencies of $0.5x10^{-3}$ %, $2.2x10^{-3}$ %, $5.9x10^{-3}$ %, and $6.1x10^{-3}$ %, respectively[144]. The enhancement in efficiency with increasing active layer concentration was attributed to an increase in absorbing material[144]. However, the effect of donor concentration variation on the performance of hybrid solar cells composed of stable inorganic acceptors is poorly understood. Herein, the effect of the amount of loading of P3HT on TiO_2 inverse opal is evaluated.

Polaron absorption was evaluated for inverse opals coated with different amounts of P3HT. **Figure 3.4 A and B** show the PIA spectra for inverse opals prepared from co-assembly of 177 and 140 nm templated samples, respectively, cast with various concentrations of P3HT ranging from 7 to 15 mg/mL. For the 177 nm samples, a 40% and 36% increase in polaron absorption was observed when decreasing the P3HT concentration from 15 mg/mL to 10 or 7 mg/mL, where samples cast with ≤10 mg/mL exhibited similar polaron absorption. Similar observations can be made for the 140 nm samples, with a 40% increase in polaron absorption being observed when decreasing P3HT concentration from 15 mg/mL to 7 mg/mL. When the amount of polymer was taken into account by normalizing the polaron absorption to the polymer absorptance at the excitation wavelength, the trend still holds. In particular, samples cast with 7 mg/mL P3HT consist of lower amount of P3HT but higher polaron absorption.

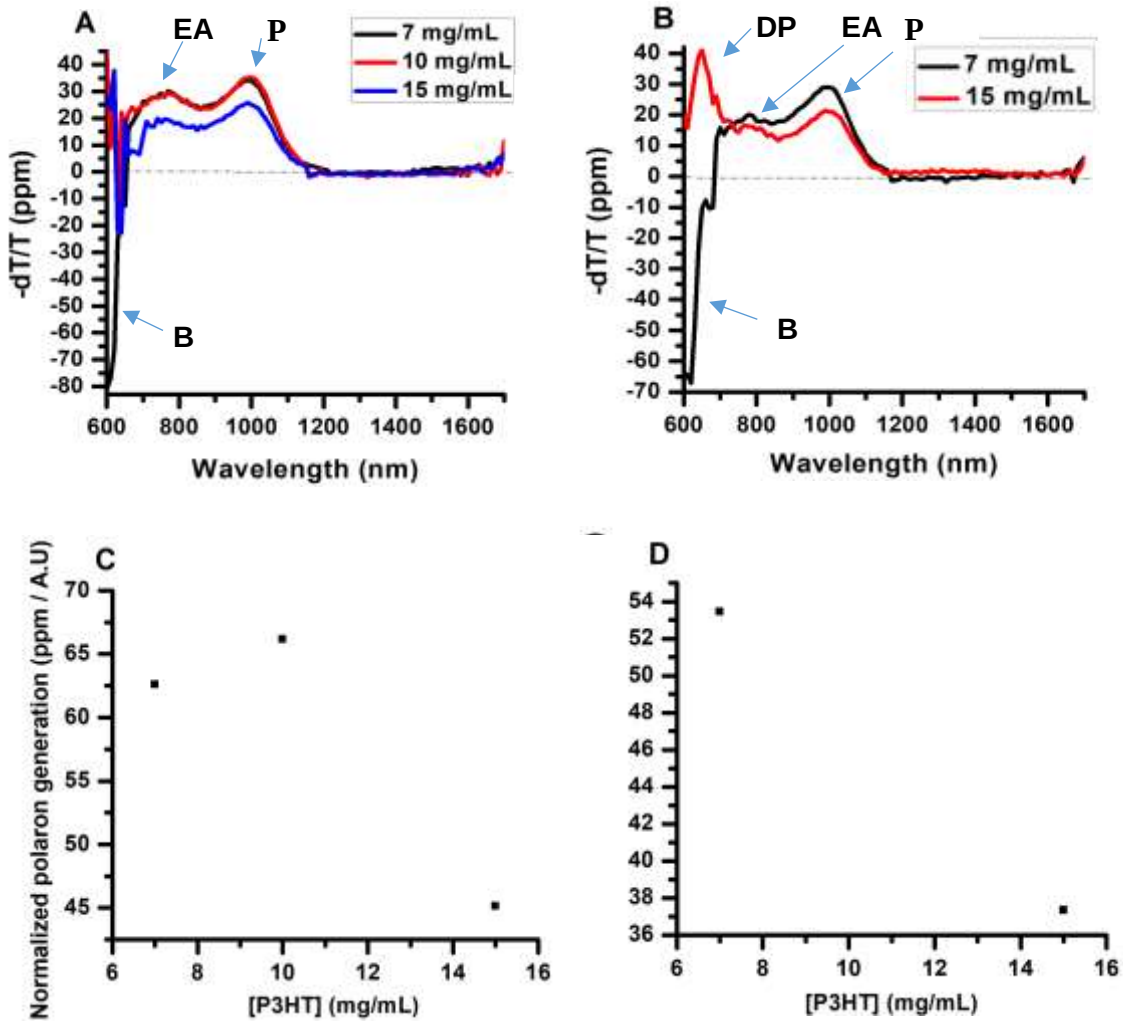

Figure 3.4: PIA spectra for 177 nm inverse opals cast with 7, 10, and 15 mg/mL concentrations of P3HT (A). PIA spectra for 140 nm inverse opals cast with 7, 15 mg/mL (B). All samples were non-passivated. 177 and 140 nm samples exhibited thicknesses of 10 and 16 layers, respectively. The transition between bleaching and absorption signals is marked by a dashed line at -dT/T = 0. Summary plots for the 177 nm samples (C) and 140 nm samples (D). Electro-absorption (EA), polaron (P), bi-polaron (DP) and ground-state depletion (B) transitions are noted near their respective peak positions.

Figure 3.4 also shows substantial bleaching signals at 620 nm in inverse opals cast with 7 mg/mL as compared to the higher polymer concentrations. The greater degree of ground state depletion of the polymer upon irradiation[137] in these samples suggest high interfacial contact between the donor and acceptor. The magnitude of

polaron absorption, polymer absorptance, and other PIA parameters are summarized in **Table 3.1**

Table 3.1: A summary of absorptance (Abs), polaron absorption (P), normalized polaron absoirption (N P), electro-absorption (EA), photoluminescence (PL), polaron lifetime (τ), and polaron lifetime distribution (γ) as a function of donor concentration ([P3HT]) for 140 and 177 nm samples.

Size (nm)	**[P3HT] (mg/mL)**	**Abs (a.u)**	**P (ppm/a.u)**	**N P (ppm/a.u)**	**EA (ppm/a.u)**	**EA:P ratio**	**PL(W)**	**τ (s)**	**γ (unitless)**
177	7	0.547	34	63	55	0.88	9.02E-11	0.034	0.951
	10	0.556	35	66	55	0.83	1.03E-10	0.048	0.906
	15	0.556	25	45	36	0.79	1.91E-10	0.188	0.703
140	7	0.541	29	53	37	0.70	5.09E-11	0.037	0.924
	15	0.562	21	37	29	0.79	1.27E-10	0.077	0.785

The features observed between 630 nm and 750 nm correspond to electro-absorption arising from the transient Stark effect[145]. The Stark effect arising due to a change in the electric field upon illumination of the nano-composite[146]. When an exciton dissociates into charge carriers at the donor:acceptor interface, the charge carriers produce an electric field that offsets the energy gap of the polymer, and has been observed in numerous polymer:acceptor nanocomposites[147,148,134], including hybrid nanocomposites[126,124]. The intensity of the electro-absorption feature acts as a function of the dielectric constant of the photoactive layer[126] and depends on whether the acceptor is organic or inorganic. Previously Noone *et al* reported significant reduction in electro-absorption features in polymer donors coupled to inorganic acceptors relative to the control PCBM acceptor which they attribute to trap states or the high dielectric screening

by the inorganic materials[126]. **Figure 3.4** shows the electroabsorption peak near 750 nm for all but the 140-nm inverse opal casted with 15 mg/mL of P3HT.

Although transient absorption features between 650 and 750 nm have been attributed to electro-absorption features, other groups have attributed the feature to bipolaron transitions resulting from delocalization of charge over the lamellae in two-dimensions[134]. The bipolaron transitions have been observed in ordered regioregular P3HT films[132,133], as well as P3HT:PCBM nano-composites[134,149]. The presence of a potential bipolaron transition for the 15 mg/mL 140 nm sample indicates interchain ordering between P3HT chains from the other concentrations[133]. Further evidence of bipolaron formation can be inferred from computation of the energy splitting factor (Δ, see **Figure 3.1**). The splitting factor can be calculated by subtracting the bipolaron and polaron transition energies from each other and dividing by 2. Performing this for the 15 mg/mL 140 nm sample results in 0.34 ev energy splitting upon bipolaron formation in P3HT, which is supported by the literature[59]. In contrast, bipolaron states are not observed in any 177 nm samples, indicating possible size effects dependence for polymer ordering.

Figure 3.5 shows the photoluminescence spectra for samples cast with different P3HT concentrations. The PL spectra show vibronic coupling corresponding to the 0-0, 0-1 and 0-2 transitions at 660,734 and 820 nm, respectively[59]. A reduction in the photoluminescence intensity with decreasing P3HT concentration is observed. Donor acceptor contact in between P3HT and TiO_2 may be enhanced with lower concentrations because most P3HT are in contact with TiO_2. It leads to more efficient dissociation of excitons at the donor acceptor interface, in line with the observed increase in polaron absorption discussed previously. A solution of P3HT ≤ 10 mg/mL may infiltrate the interstitial sites of nano-crystalline domains more effectively without forming a thick layer on the surface compared to samples coated with 15 mg/mL, thereby leading to enhanced interfacial contact.

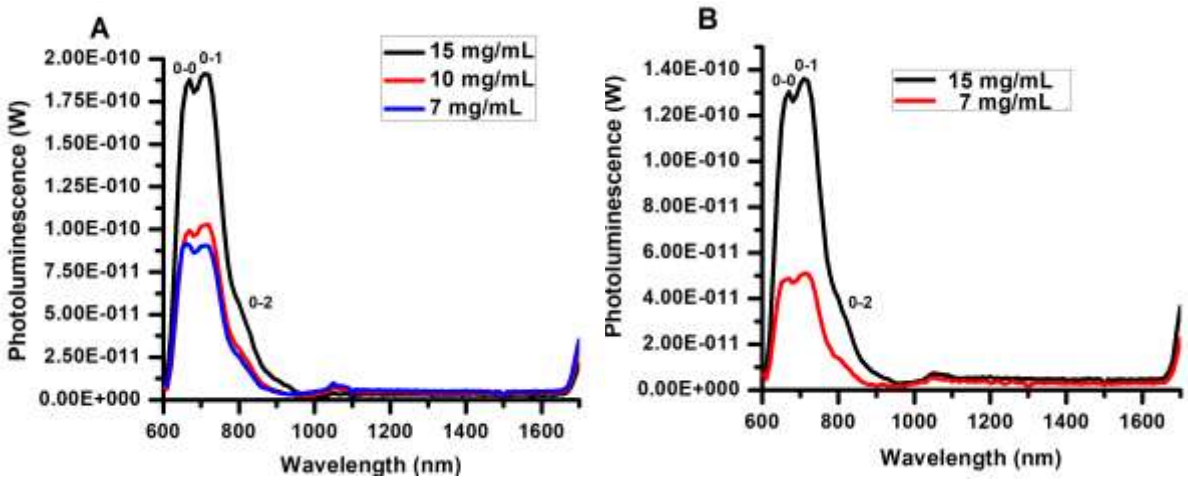

Figure 3.5: Photoluminescence spectra for 177 nm samples (A) and 140 nm samples (B). Vibronic transitions are noted.

Additionally samples coated with dilute P3HT solution (i.e. 7 mg/mL) exhibit low polaron lifetime (τ = 34 ms) and narrow polaron dispersion (γ = 0.95), indicating that charge capture by trap states becomes less severe in both sets of samples with lower P3HT concentrations[126]. Polaron lifetimes and lifetime distributions are longer and broader for samples cast with 15 mg/mL P3HT. This may be due to bipolaron formation, as observed in the 140 nm sample, in which polarons can delocalize over stacked P3HT chains, reducing recombination rates and lengthening the polaron lifetime.

3.3.2. Probing the effect of $TiCl_4$ treatment on polaron absorption

Figure 3.6 shows representative PIA spectra and the average PIA signals of samples with different $TiCl_4$ passivation treatments. Previously discussed features, including electro-absorption at 750 nm and polaron absorption at 1000 nm, are observed in the PIA spectra of the passivated inverse opals. A linear increase in polaron absorption with increasing passivation treatment is observed. The 0.025 M $TiCl_4$-treated samples exhibit about 2.5 times more polarons than those of non-passivated samples while 0.05 M and 0.05 M x2 $TiCl_4$ treated samples exhibit about 6 and 10 times higher polaron signals than those of non-passivated samples, respectively. The significant increase may arise from the increased donor to acceptor contact as the walls of the TiO_2 inverse opals thicken with passivation treatment (**Figure 2.12,Section 2.2.1**). The increased wall thickness can provide greater donor to acceptor contact due to the larger

amount of TiO_2 which would favor charge separation and increase polaron absorption but can also lead to higher amount of disordered P3HT due to higher surface roughness of the inorganic framework. This factor may have contributed to the large variation in polaron absorption for films passivated twice with 0.05 M $TiCl_4$. Representative PIA spectra for each passivation condition combined with a summary of polaron absorption at 1000 nm for each passivation condition are summarized in **Figure 3.6**.

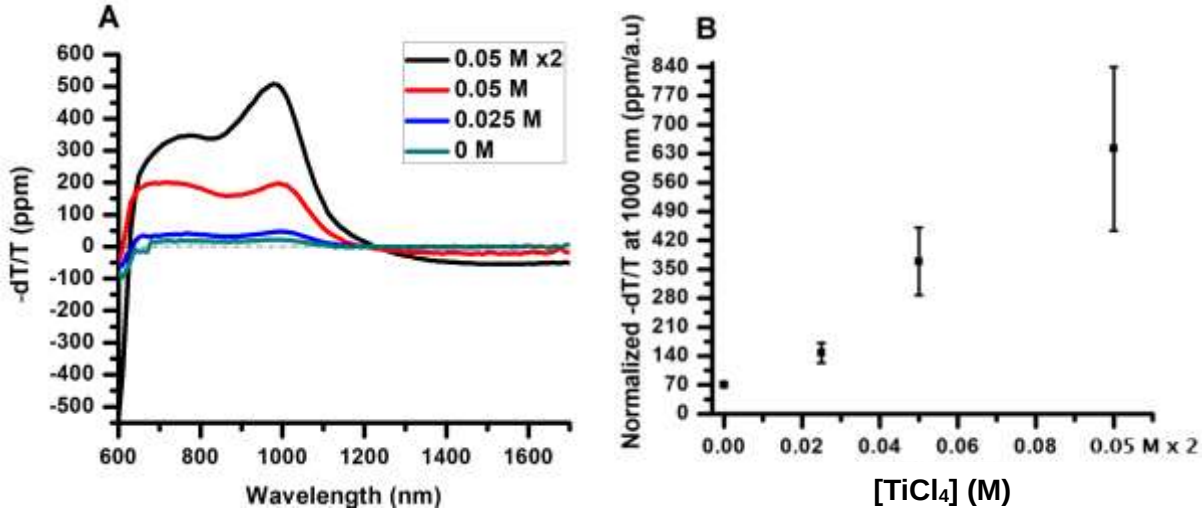

Figure 3.6: Photoinduced absorption spectra for 140 nm inverse opals with different $TiCl_4$ passivation conditions (A). Summary of polaron absorption as a function of $TiCl_4$ treatment (B). Error bars correspond to the standard deviation of the mean of 6 samples for each condition. Transition of signals from absorption to bleaching or stimulated emission is marked by a dashed line (A).

Figure 3.7 shows the photoluminescence spectra for i-P3HT/TiO_2-o treated with different concentrations of $TiCl_4$. P3HT not in contact with TiO_2 or disordered P3HT would be emissive and leads to higher absorption near 460 nm as shown in Figure 2.19 C and D. Significantly higher photoluminescence intensity is observed for twice passivated samples compared to non-passivated samples and other passivation conditions which is also attributed to a higher degree of disordered P3HT not in contact with TiO_2 in the twice passivated samples. The consequence of this is that a large population of excitons are produced in 0.05 M x2 passivated samples compared to other passivation conditions but the thickness of the P3HT over-layer is probably larger than the diffusion length of the

P3HT exciton, reducing exciton dissociation probability[150] and leading to ground state relaxation before dissociating at the donor:acceptor interface[40], therefore more disordered P3HT would be emissive[60].

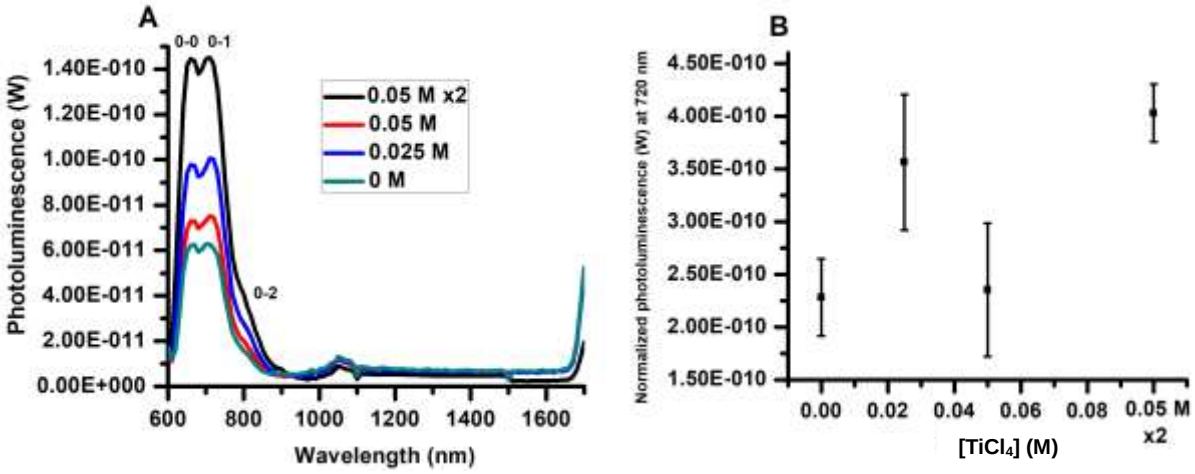

Figure 3.7: Representative photo-luminescence spectra as a function of $TiCl_4$ passivation concentration (A). Summary of average photoluminescence peak intensity at 720 nm as a function of passivation concentration (B). 5 Samples were used for each passivation condition. Error bars correspond to standard error of the mean.

Enhanced polaron absorption with passivation treatment indicates a higher degree of electron transfer into TiO_2. Broad near infrared signal with an onset of 1200 nm extending up to 1700 nm can be observed in $TiCl_4$ passivated samples in **Figure 3.3 A**. It may be attributed to enhanced photoluminescence arising from the relaxation of electrons in the conduction band to lower lying energy states after charge separation. The intensity of the emission increases with increasing passivation treatment as shown in **Figure 3.8**.

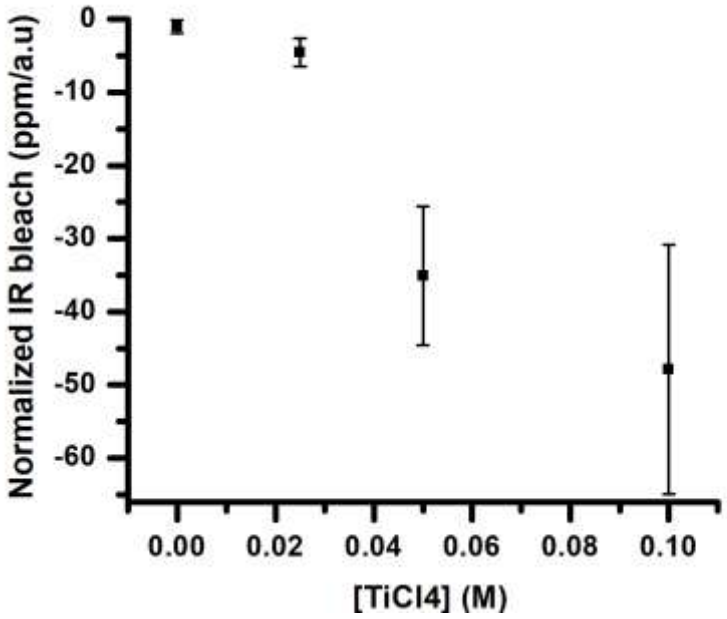

Figure 3.8: Normalized IR photoluminescence at 1360 nm as a function of passivation concentration. Error bars correspond to the standard error of the mean.

The effect of passivation on charge transport and recombination can be determined by polaron lifetime[124]. **Figure 3.9** shows the normalized fractional change in probe beam transmittance as a function of frequency and polaron lifetime (τ) as a function of passivation treatment. The dispersive recombination model (eqn 3.1) ignores the distinction between unimolecular and bimolecular recombination mechanisms for charge carrier relaxation[151], and incorporates charge capture by trap states into the polaron lifetime, in which reduced charge carrier trapping yields narrow polaron lifetime distributions and disordered polymer broadens polaron lifetime distribution[134]. Passivated samples exhibit lower polaron lifetimes and lower lifetime distributions (γ) compared to non-passivated samples. The average polaron lifetimes for non-passivated, 0.025 M, 0.05 M, and 0.05 M x2 passivated samples are 110 ± 24 ms, 57 ± 23 ms, 13.8 ± 3.0 ms, and 9.4 ± 1.2 ms, respectively.

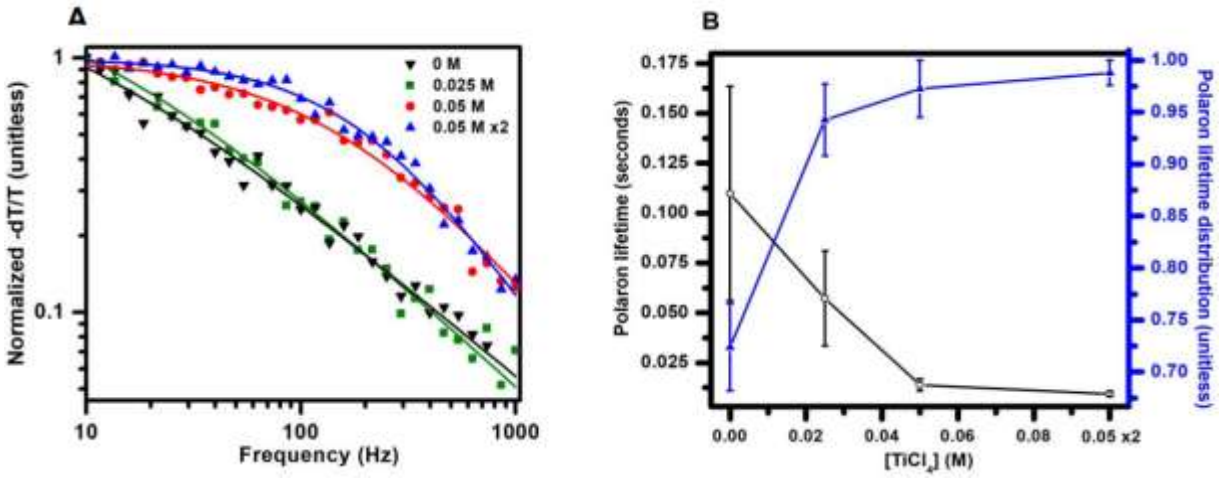

Figure 3.9: Normalized fractional change in transmittance as a function of pump frequency (A). Geometric shapes correspond to experimental data while solid lines correspond to dispersive recombination fits. Summary of polaron lifetime (black) and lifetime distribution (blue) as a function of passivation treatment (B). All samples were spuncoat with 7 mg/mL P3HT and 140 nm polystyrene sphere were used to prepare the inverse opals by co-assembly.

The difficulty of exciton dissociation in low band gap polymers has been previously discussed in terms of the small dielectric constant of organic compounds[152]. Tailoring organic donors to inorganic acceptors with large dielectric constants can quench electro-absorption features via attenuation of the electric field that emerges upon exciton dissociation[145]. Furthermore, electric field attenuation has consequences for charge carrier lifetimes, in which dielectric screening increases P3HT polaron lifetimes[126]. Reduction in polaron lifetime with increasing passivation can be attributed to improved carrier mobility by virtue of trap state passivation upon $TiCl_4$ treatment and/or reduction in dielectric screening by TiO_2. To evaluate the effect of passivation on exciton electric field attenuation, electro-absorption was corrected for potential enhancements in exciton formation/dissociation with passivation by analyzing the ratio of electro- absorption to polaron absorption (EA:P). A reduction in EA:P with $TiCl_4$ would be expected if more effective dielectric screening occurs with increasing passivation. Relative similarity in EA:P ratios is observed for all conditions except for 0.05 M which exhibits a larger ratio, indicating less effect dielectric screening relative to other passivation treatments. Since the EA:P ratio does not correlate with the exponential reduction in polaron lifetime with

increasing passivation treatment, we attribute trap state passivation as the dominant mechanism for reduced polaron recombination over potential dielectric screening effects.

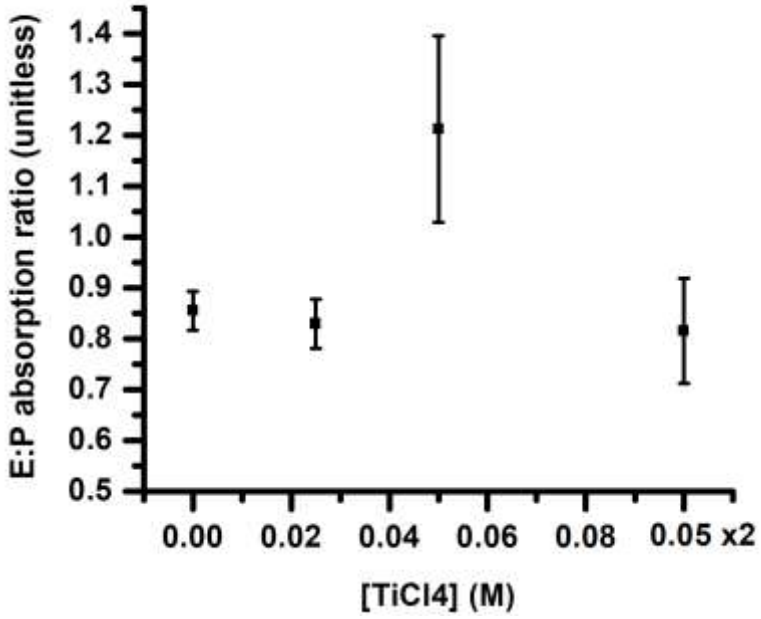

Figure 3.10: Electro-absorption to polaron absorption ratio as a function of $TiCl_4$ passivation treatement. Error bars correspond to the standard error of the mean. 5 samples were used for each passivation condition.

3.3.3. Probing the effect of donor composition on polaron absorption

Next, we evaluate the effect of solution processing and donor composition on polaron absorption in 0.05 M $TiCl_4$ passivated 140 nm inverse opal nano-composites. The identity and relative amount of donor species in contact with the acceptor can have a tremendous effect of device performance.[41] The following donor compositions were explored: spincoating P3HT directly onto TiO_2 (**Fig. 3.11 A**), direct spincoating of a 1:1 weight ratio P3HT:PCBM blend mixture on TiO_2 **(Fig. 3.11 B**); and sequential spincoating of PCBM onto the inverse opal followed by P3HT spincoating (**Fig. 3.11 C**).

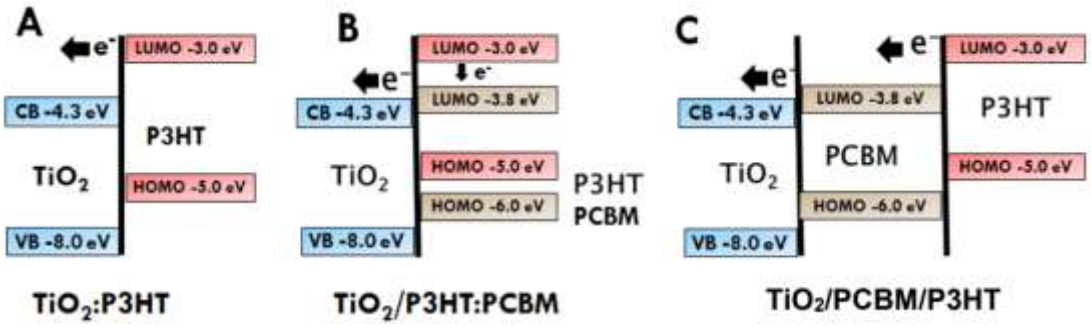

Figure 3.11: Energy level diagram highlighting electron transfer from P3HT directly into TiO2 (A), P3HT into PCBM as a mix then into TiO_2 (B), and P3HT into PCBM then into TiO_2. Solid black bars mark interfaces. Energy level values taken from Yip *et al*[32].

Polaron absorption of PCBM-containing donor was evaluated relative to P3HT-TiO_2 samples. Representative PIA spectra as well as a summary of normalized polaron absorption for the new donor compositions are summarized in **Figure 3.12.** Prominent PIA features seen in previous samples (**Section 3.3.1 and 3.3.2**) can be observed. Polaron absorption near 1000 nm is observed in all samples except the P3HT:PCBM/TiO_2 sample, which exhibits at feature near 920 nm characteristic of triplet exciton formation due to intersystem crossing in RR-P3HT solutions[153]. This might indicate stronger disorder of P3HT on the P3HT:PCBM/TiO_2 nano-composites[154]. All donor compositions exhibited high polaron absorptions intensities. P3HT/TiO_2 films displayed the largest polaron absorption, and PCBM:P3HT/TiO_2 films displaying the lowest polaron absorption and PCBM/P3HT/TiO_2 films displaying intermediate polaron absorption. Also, electro-absorption is not well-resolved in the P3HT:PCBM/TiO_2 sample.

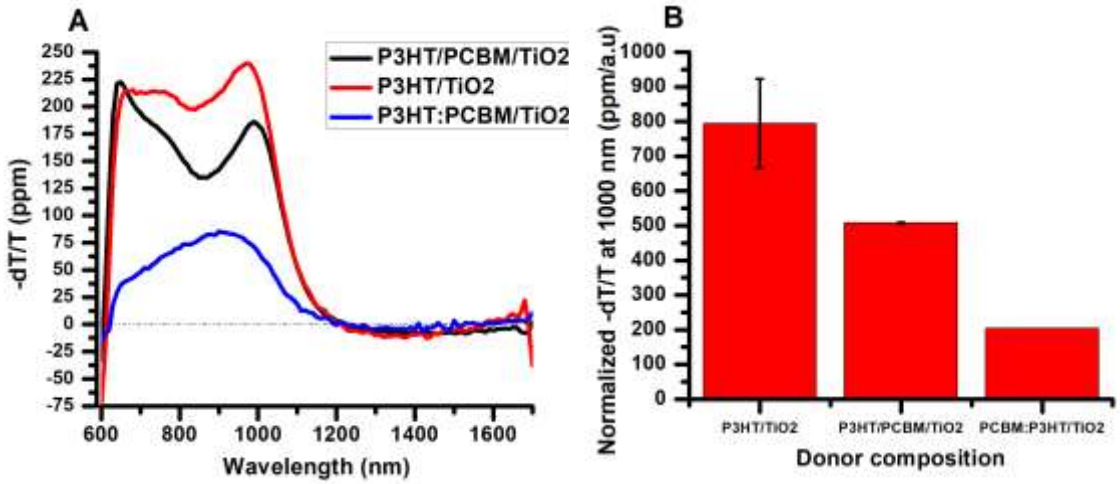

Figure 3.12: PIA spectra for different donor compositions (A**).** Summary plot of mean polaron absorption at 1000 nm as a function of donor composition (B). Each inverse opal sample was passivated with 0.05 M $TiCl_4$ and cast with 7mg/mL of the respective donor agent. Error bars correspond to the standard deviation of the mean collected from 3 samples.

Low polaron absorption may stem from material loss during the spincoating process. To analyze this, the absorptance spectra were obtained for each composition, which is summarized in **Figure 3.13**. The directly cast P3HT:PCBM exhibited the lowest absorptance near 550 nm, indicating a loss of material during either solution preparation or the spincoating process and may also be due to different wetting behavior of P3HT on either TiO_2 or PCBM. For example, organization of P3HT within TiO_2 nanotubes into polymer nano-wires or nano-pores depends on wetting behavior[155]. Surprisingly, the P3HT/PCBM/TiO_2 samples exhibited slightly higher absorptance than the pure P3HT samples, at both 550 nm and the excitation wavelength. This indicates that differences in absorptance at 460 nm alone can't account for the larger polaron absorption observed in P3HT/TiO_2 samples. Reduced polaron absorption in PCBM containing films may stem from different ordering of P3HT which inhibits polaron formation, although more experiments may be required to resolve this.

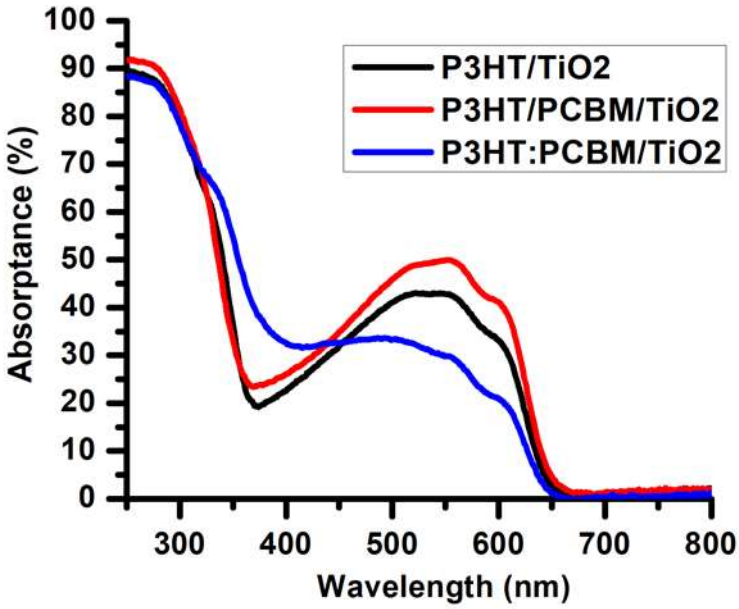

Figure 3.13: Representative absorptance spectra for nano-composites for each donor composition .

The lack of electro-absorption feature and polaron absorption in the P3HT:PCBM blend sample may originate from the poor quality of the sample, which may also explain the longer polaron lifetimes and broader lifetime distributions observed relative to other compositions, as shown in **Figure 3.14** below.

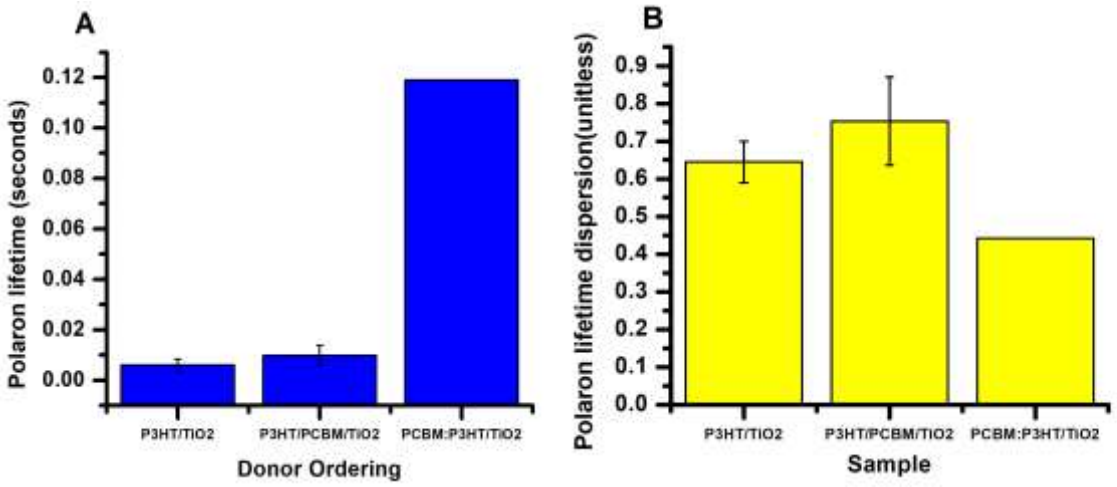

Figure 3.14: Mean polaron lifetime (A) and mean polaron lifetime distribution (B) for each donor composition. Error bars correspond to standard error of the mean collected from 3 samples.

Polaron lifetimes increase when going from P3HT/TiO_2 samples to P3HT/PCBM/TiO_2 samples to P3HT:PCBM/TiO_2 samples, indicating minimal charge capture of trap states in reduced PCBM content[126]. This conflicts with the photoluminescence spectra collected, shown in **Figure 3.15**. The quenching of photoluminescence spectra generally correlates with a lower polaron lifetime. This is consistent for P3HT/TiO_2 and P3HT/PCBM/TiO_2 but not for the P3HT:PCBM/TiO_2 film which exhibits the lower PL and the largest polaron lifetime.

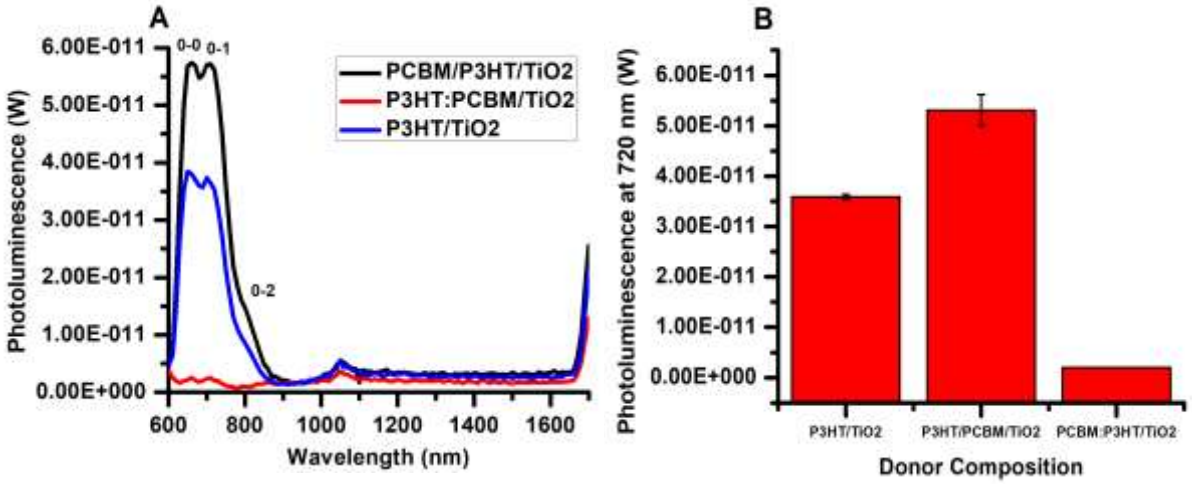

Figure 3.15: Photoluminescence spectra as a function of donor composition (A). Summary of photoluminescence intensity at 720 nm as a function of donor composition (B). Error bars correspond to standard deviation of the mean collected from 3 samples.

.

Chapter 4. Conclusions and Future Work

We have fabricated nano-composites using electron-accepting inverse opal photonic crystal structure of titania coupled to an electron-donating poly (3 – hexylthiophene. Inverse opals were fabricated by coassembly of polystyrene spheres and TiBALDH precursor to produce better quality inverse opals with reduced cracking and baseline scattering relative to IO prepared by infiltration of polystyrene templates. X-ray diffraction and Raman spectroscopy confirmed anatase phase composition for passivated inverse opals as well as inverse opals prepared from infiltration and co-assembly methods. Crystallite size increased with increasing $TiCl_4$ treatment and crystallite size was larger for infiltrated samples compared to co-assembled samples. The thickness of the inverse opal wall increased upon passivation as determined by SEM. Both parameters are expected to improve charge separation as increased crystallite size reduces the activation energy for charge separation and increased wall thickness increases donor:acceptor contact which could also be varied by changing the concentration of the solution from which P3HT is cast. Photoinduced absorption spectroscopy was used to probe polaron generation and polaron lifetimes in nanocomposites as a function of donor concentration, $TiCl_4$ treatment, and donor composition. Reducing P3HT concentration from 15 mg/mL to 7 mg/mL increased polaron absorption, reduced lifetime and enhanced lifetime distribution for both 177 nm and 140 nm inverse opals. A linear increase in polaron absorption with passivation was observed, with polaron absorption enhanced by 10 times for the 0.05 M twice passivated sample. Polaron lifetimes decreased exponentially with increasing $TiCl_4$ concentration and polaron lifetime distributions increased with $TiCl_4$ concentration in a similar manner due to either passivation of trap states or increased contact of the donor:acceptor materials. Increased absorptance of P3HT between 325 and 550 nm for the P3HT component of the nano-composite increased linearly with increasing passivation concentration due to a higher degree of unaggregated,emissive P3HT relative to the non-passivated samples. Increased disorder of P3HT was induced by the increased surface roughness of passivated TiO_2 films. Substituting P3HT with sequentially coated PCBM/P3HT or 1:1 blended PCBM:P3HT donor compositions resulted in reduced polaron absorption and longer polaron lifetimes indicating less efficient charge separation, and higher charge trapping relative to pure P3HT samples, respectively. Increased charge separation in P3HT coated TiO_2 inverse opals presents an opportunity

to apply the large internal surface areas of inverse opals to bulk heterojunction solar cell applications. The successful incorporation of passivated TiO_2 inverse opals into a functioning device could present a new paradigm in emerging hybrid photovoltaics. Insights into the effect of passivation on transient absorption properties of P3HT point towards the application of passivated inverse opals as a model system for evaluating photoinduced properties of other conjugated polymers of interest as well as contributing to the wealth of research concerned with the mechanism of passivation in solar cell components. Future work will concern photoelectron spectroscopy and spectro-electrochemistry measurements of TiO_2 cast with P3HT as a function of passivation treatment as a means of quantifying band bending at the TiO_2:P3HT interface which may contribute to enhanced charge separation with increasing passivation.

References

(1) Shockley, W.; Queisser, H. J. *J-Appl.Phys.* **1961**, *32* (1961), 510–519.

(2) Saga, T. *NPG Asia Mater.* **2010**, *2* (3), 96–102.

(3) Mohammad Bagher, A. *Int. J. Renew. Sustain. Energy* **2014**, *3* (3), 53.

(4) Banerjee, S.; Pillai, S. C.; Falaras, P.; O'Shea, K. E.; Byrne, J. A.; Dionysiou, D. D. *J. Phys. Chem. Lett.* **2014**, *5* (15), 2543–2554.

(5) Bach, U.; Lupo, D.; Comte, P.; Moser, J. E.; Weissörtel, F.; Salbeck, J.; Spreitzer, H.; Grätzel, M. *Nature* **1998**, *395* (6702), 583–585.

(6) Burke, A.; Ito, S.; Snaith, H.; Bach, U.; Kwiatkowski, J.; Grätzel, M. *Nano Lett.* **2008**, *8* (4), 977–981.

(7) Ko, K. H.; Lee, Y. C.; Jung, Y. J. *J. Colloid Interface Sci.* **2005**, *283* (2), 482–487.

(8) Fan, J.; Li, Z.; Zhou, W.; Miao, Y.; Zhang, Y.; Hu, J.; Shao, G. *Appl. Surf. Sci.* **2014**, *319* (1), 75–82.

(9) Fitra, M.; Daut, I.; Irwanto, M.; Gomesh, N.; Irwan, Y. M. *Energy Procedia* **2013**, *36*, 278–286.

(10) Das, T. K.; Ilaiyaraja, P.; Mocherla, P. S. V; Bhalerao, G. M.; Sudakar, C. *Sol. Energy Mater. Sol. Cells* **2016**, *144*, 194–209.

(11) Biernat, K.; Malinowski, A.; Gnat, M. *Biofuels - Econ. Environ. Sustain.* **2013**.

(12) Nakano, Y. *Ambio* **2012**, *41* (SUPPL.2), 125–131.

(13) Bailey, S.; Raffaelle, R. *Space Solar Cells and Arrays*; 2011.

(14) National Renewable Energy Laboratory. *Web*. 2016, p Efficiency Chart.

(15) Becker, J. J.; Boccard, M.; Campbell, C. M.; Zhao, Y.; Lassise, M.; Holman, Z. C.; Zhang, Y. H. *IEEE J. Photovoltaics* **2017**, *7* (3), 900–905.

(16) Zweibel, K. *Science (80-.).* **2010**, *328* (5979), 699–701.

(17) Grätzel, M. *J. Photochem. Photobiol. C Photochem. Rev.* **2003**, *4* (2), 145–153.

(18) Mathew, S.; Yella, A.; Gao, P.; Humphry-Baker, R.; Curchod, B. F. E.; Ashari-Astani, N.; Tavernelli, I.; Rothlisberger, U.; Nazeeruddin, M. K.; Grätzel, M. *Nat. Chem.* **2014**, *6* (3), 242–247.

(19) Hardin, B. E.; Snaith, H. J.; McGehee, M. D. *Nat. Photonics* **2012**, *6* (3), 162–169.

(20) Maçaira, J.; Mesquita, I.; Andrade, L.; Mendes, a. *Phys. Chem. Chem. Phys.* **2015**, *17* (35), 22699–22710.

(21) Yang, W. S.; Park, B.-W.; Jung, E. H.; Jeon, N. J.; Kim, Y. C.; Lee, D. U.; Shin, S. S.; Seo, J.; Kim, E. K.; Noh, J. H.; Seok, S. Il. *Science (80-.).* **2017**, *356* (6345), 1376–1379.

(22) Hoke, E. T.; Slotcavage, D. J.; Dohner, E. R.; Bowring, A. R.; Karunadasa, H. I.; McGehee, M. D. *Chem. Sci.* **2015**, *6* (1), 613–617.

(23) Roiati, V.; Mosconi, E.; Listorti, A.; Colella, S.; Gigli, G.; De Angelis, F. *Nano Lett.* **2014**, *14* (4), 2168–2174.

(24) Yang, S.; Fu, W.; Zhang, Z.; Chen, H.; Li, C.-Z. *J. Mater. Chem. A* **2017**, *5* (23), 11462–11482.

(25) Snaith, H. J. *J. Phys. Chem. Lett.* **2013**, *4* (21), 3623–3630.

(26) Benmessaoud, I. R.; Mahul-Mellier, A.-L.; Horváth, E.; Maco, B.; Spina, M.; Lashuel, H. A.; Forró, L. *Toxicol. Res.* **2016**, *5* (2), 407–419.

(27) Akihiro Kojima,† Kenjiro Teshima,‡ Yasuo Shirai, and T. M. *J Am Chem Soc* **2009**, *131* (October), 6050–6051.

(28) Hoppea; Sariciftci. *J. Mater. Res* **2004**, *19* (7), 1925.

(29) Brabec, C. J.; Hauch, J. a; Schilinsky, P.; Waldauf, C. *MRS Bull.* **2005**, *30* (January), 50–52.

(30) Schwarz, K. N.; Farley, S. B.; Smith, T. a; Ghiggino, K. P. *Nanoscale* **2015**, 19899–19904.

(31) Leblebici, S. Y.; Chen, T. L.; Olalde-Velasco, P.; Yang, W.; Ma, B. *ACS Appl. Mater. Interfaces* **2013**, *5* (20), 10105–10110.

(32) Yip, H.-L.; Jen, A. K.-Y. *Energy Environ. Sci.* **2012**, *5* (3), 5994.

(33) Haring, A. J.; Ahrenholtz, S. R.; Morris, A. J. *ACS Appl. Mater. Interfaces* **2014**, *6* (6), 4394–4401.

(34) Moritomo, Y.; Yonezawa, K.; Yasuda, T. *Int. J. Photoenergy* **2016**, *2016* (2).

(35) Le, K. Q.; Abass, A.; Maes, B.; Bienstman, P.; Alù, A. *Opt. Express* **2012**, *20* (S1), A39.

(36) Zhou, Y.; Eck, M.; Krüger, M. *Energy Environ. Sci.* **2010**, *3* (12), 1851.

(37) Yu, W.; Xu, B.; Dong, Q.; Zhou, Y.; Zhang, J.; Tian, W.; Yang, B. *J. Solid State Electrochem.* **2010**, *14* (6), 1051–1056.

(38) Petersen, A.; Ojala, A.; Kirchartz, T.; Wagner, T. A.; W??rthner, F.; Rau, U. *Phys. Rev. B - Condens. Matter Mater. Phys.* **2012**, *85* (24), 1–10.

(39) Loiudice, A.; Rizzo, A.; Biasiucci, M.; Gigli, G. **2012**.

(40) Tamai, Y.; Ohkita, H.; Benten, H.; Ito, S. *J. Phys. Chem. Lett.* **2015**, *6* (17), 3417–3428.

(41) Luo, G.; Ren, X.; Zhang, S.; Wu, H.; Choy, W. C. H.; He, Z.; Cao, Y. *Small* **2016**, *12* (12), 1547–1571.

(42) Heeger, A. J. *Adv. Mater.* **2014**, *26* (1), 10–28.

(43) Ghosh, T.; Panicker, J. S.; Nair, V. C. *Polymers (Basel).* **2017**, *9* (3).

(44) Martinez, L.; Stavrinadis, A.; Higuchi, S.; Diedenhofen, S. L.; Bernechea, M.; Tajima, K.; Konstantatos, G. *Phys. Chem. Chem. Phys.* **2013**, *15* (15), 5482.

(45) Kleinschmidt, A. T.; Root, S. E.; Lipomi, D. J. *J. Mater. Chem. A* **2017**, *5* (23), 11396–11400.

(46) Facchetti, A. *Mater. Today* **2013**, *16* (4), 123–132.

(47) Dang, M. T.; Hirsch, L.; Wantz, G. *Adv. Mater.* **2011**, *23* (31), 3597–3602.

(48) Zhao, C. X.; Mao, A. Y.; Xu, G. *Appl. Phys. Lett.* **2014**, *105* (6).

(49) Kadem, B.; Hassan, A.; Cranton, W. *J. Mater. Sci. Mater. Electron.* **2016**, *27* (7), 7038–7048.

(50) Liang, Y.; Xu, Z.; Xia, J.; Tsai, S. T.; Wu, Y.; Li, G.; Ray, C.; Yu, L. *Adv. Mater.* **2010**, *22* (20), 135–138.

(51) Kuo, C. Y.; Tang, W. C.; Gau, C.; Guo, T. F.; Jeng, D. Z. *Appl. Phys. Lett.* **2008**, *93* (3), 1–4.

(52) Liu, R. *Materials (Basel).* **2014**, *7* (4), 2747–2771.

(53) Truong, N. T. N.; Nguyen, H.; Le, P. H. T.; Park, C.; Jung, J. H. *J. Nanomater.* **2017**, *2017*.

(54) Saunders, B. R.; Turner, M. L. *Adv. Colloid Interface Sci.* **2008**, *138* (1), 1–23.

(55) Bhatt, M. D.; Lee, J. S. *New J. Chem.* **2017**, *41*, 10508–10527.

(56) Freitag, M.; Teuscher, J.; Saygili, Y.; Zhang, X.; Giordano, F.; Liska, P.; Hua, J.; Zakeeruddin, S. M.; Moser, J.-E.; Grätzel, M.; Hagfeldt, A. *Nat. Photonics* **2017**, *11* (6), 372–378.

(57) Carey, G. H.; Abdelhady, A. L.; Ning, Z.; Thon, S. M.; Bakr, O. M.; Sargent, E. H. *Chem. Rev.* **2015**, *115* (23), 12732–12763.

(58) Yang, P.; Zhou, X.; Cao, G.; Luscombe, C. K. *J. Mater. Chem.* **2010**, *20* (13), 2612.

(59) Salleo, A.; Kline, R. J.; DeLongchamp, D. M.; Chabinyc, M. L. *Adv. Mater.* **2010**, *22* (34), 3812–3838.

(60) Panzer, F.; Bässler, H.; Lohwasser, R.; Thelakkat, M.; Köhler, A. *J. Phys. Chem. Lett.* **2014**, *5* (15), 2742–2747.

(61) Spano, F. C.; Silva, C. *Annu. Rev. Phys. Chem.* **2014**, *65*, 477–500.

(62) Marszalek, T.; Li, M.; Pisula, W. *Chemi.Comm* **2016**, *Accepted*, 1–3.

(63) Duché, D.; Masclaux, C.; Le Rouzo, J.; Gourgon, C. *J. Appl. Phys.* **2015**, *117* (5).

(64) Armstrong, E.; O'Dwyer, C. *J. Mater. Chem. C* **2015**, *3* (24), 6109–6143.

(65) Chen, J. I. L.; von Freymann, G.; Choi, S. Y.; Kitaev, V.; Ozin, G. A. *J. Mater. Chem.* **2008**, *18* (4), 369–373.

(66) Chen, J. I. L.; von Freymann, G.; Choi, S. Y.; Kitaev, V.; Ozin, G. A. *Adv. Mater.* **2006**, *18* (14), 1915–1919.

(67) Kinoshita, S.; Yoshioka, S.; Miyazaki, J. *Reports Prog. Phys.* **2008**, *71* (7), 76401.

(68) McPhedran, R. C.; Nicorovici, N. A.; McKenzie, D. R.; Botten, L. C.; Parker, A. R.; Rouse, G. W. *Aust. J. Chem.* **2001**, *54* (4), 241–244.

(69) Zi, J.; Yu, X.; Li, Y.; Hu, X.; Xu, C.; Wang, X.; Liu, X.; Fu, R. *Proc. Natl. Acad. Sci.* **2003**, *100* (22), 12576–12578.

(70) Chigrin, D. N.; Torres, C. M. S. *Opt. i Spektrosk.* **2001**, *91* (3), 513–518.

(71) Maurin, I.; Moufarej, E.; Laliotis, A.; Bloch, D. *J. Opt. Soc. Am. B* **2015**, *32* (8), 1761.

(72) Ko, D.-H.; Tumbleston, J. R.; Zhang, L.; Williams, S.; DeSimone, J. M.; Lopez, R.; Samulski, E. T. *Nano Lett.* **2009**, *9* (7), 2742–2746.

(73) Tulsiram, N.; Kerr, C.; Chen, J. I. L. *J. Phys. Chem. C* **2017**, *121* (48), 26987–26996.

(74) Ma, J.; Chu, J.; Qiang, L.; Xue, J. *Int. J. Photoenergy* **2013**, *2013*.

(75) Zare, M.; Mortezaali, A.; Shafiekhani, A. *J. Phys. Chem. C* **2016**, *120* (17), 9017–

9027.

(76) Lee, S. W.; Ahn, K. S.; Zhu, K.; Neale, N. R.; Frank, a J. *J. Phys. Chem. C* **2012**, *116*, 21285–21290.

(77) Deskins, N. A.; Rousseau, R.; Dupuis, M. *J. Phys. Chem. C* **2010**, *114* (13), 5891–5897.

(78) Ikeda, H. *J. Appl. Phys.* **2002**, *91* (7), 4637–4645.

(79) Duan, H.-S.; Zhou, H.; Chen, Q.; Sun, P.; Luo, S.; Song, T.-B.; Bob, B.; Yang, Y. *Phys. Chem. Chem. Phys.* **2015**, *17* (1), 112–116.

(80) Di Valentin, C.; Pacchioni, G.; Selloni, A. *J. Phys. Chem. C* **2009**, *113* (48), 20543–20552.

(81) Knorr, F. J.; McHale, J. L. *J. Phys. Chem. C* **2013**, *117* (26), 13654–13662.

(82) Mercado, C. C.; Knorr, F. J.; McHale, J. L.; Usmani, S. M.; Ichimura, A. S.; Saraf, L. V. *J. Phys. Chem. C* **2012**, *116* (19), 10796–10804.

(83) Zhang, J.; Feng, J.; Hong, Y.; Zhu, Y.; Han, L. *J. Power Sources* **2014**, *257*, 264–271.

(84) Knorr, F. J.; Zhang, D.; McHale, J. L. *Langmuir* **2007**, *23* (17), 8686–8690.

(85) Luo, Z.; Poyraz, A. S.; Kuo, C. H.; Miao, R.; Meng, Y.; Chen, S. Y.; Jiang, T.; Wenos, C.; Suib, S. L. *Chem. Mater.* **2015**, *27* (1), 6–17.

(86) Kotsyubynsky, V. O.; Myronyuk, I. F.; Myronyuk, L. I.; Chelyadyn, V. L.; Mizilevska, M. H.; Hrubiak, A. B.; Tadeush, O. K.; Nizamutdinov, F. M. *Materwiss. Werksttech.* **2016**, *47* (2–3), 288–294.

(87) Ahmed, R.; Bell, J.; Wang, H. **2013**, *8793*, 87930Z.

(88) Kim, J.; Choi, H.; Nahm, C.; Kim, C.; Nam, S.; Kang, S.; Jung, D.; Kim, J. I.; Kang, J.; Park, B. **2012**, *220*, 108–114.

(89) Lin, Y.; Xiao, X. R.; Li, W. Y.; Wang, W. B.; Li, X. P.; Cheng, J. Y. *J. Photochem.*

Photobiol. A Chem. **2003**, *159* (1), 41–45.

(90) Murakami, T. N.; Miyadera, T.; Funaki, T.; Cojocaru, L.; Kazaoui, S.; Chikamatsu, M.; Segawa, H. *ACS Appl. Mater. Interfaces* **2017**, acsami.7b07496.

(91) Shin, J.-H.; Moon, J. H. *Langmuir* **2011**, *27* (10), 6311–6315.

(92) Hu, Z.; Xu, L.; Wang, L.; Huang, Y.; Xu, L.; Chen, J. *Catal. Commun.* **2013**, *40*, 106–110.

(93) Kinsinger, N. M.; Wong, A.; Li, D.; Villalobos, F.; Kisailus, D. *Cryst. Growth Des.* **2010**, *10* (12), 5254–5261.

(94) Hatton, B.; Mishchenko, L.; Davis, S.; Sandhage, K. H.; Aizenberg, J. *Proc. Natl. Acad. Sci.* **2010**, *107* (23), 10354–10359.

(95) Seisenbaeva, G. a; Daniel, G.; Nedelec, J.-M.; Kessler, V. G. *Nanoscale* **2013**, *5* (8), 3330–3336.

(96) Reese, C.; Guerrero, C.; Weissman, J.; Lee, K.; Asher, S. *J. Colloid Interface Sci.* **2000**, *232* (1), 76–80.

(97) Dimitrov, A. S.; Nagayama, K. *Langmuir* **1996**, *12* (5), 1303–1311.

(98) Yang, S. M.; Ozin, G. A. **2003**, No. 13, 3479–3485.

(99) Baryshev, A. V; Kaplyanskii, A. A.; Kosobukin, V. A.; Limonov, M. F.; Skvortsov, A. P. *Phys. Solid State* **2004**, *46* (7), 1331–1339.

(100) Fang, J.; Xuan, Y.; Li, Q. *Sci. China Technol. Sci.* **2010**, *53* (11), 3088–3093.

(101) Rengarajan, R.; Mittleman, D.; Rich, C.; Colvin, V. *Phys. Rev. E - Stat. Nonlinear, Soft Matter Phys.* **2005**, *71* (1), 1–11.

(102) Ha, N. Y.; Wu, J. W.; Park, B. *J. Korean Phys. Soc.* **2004**, *45* (1), 108–111.

(103) Nishijima, Y.; Ueno, K.; Juodkazis, S.; Mizeikis, V.; Misawa, H.; Tanimura, T.; Maeda, K. *Opt. Express* **2007**, *15* (20), 12979.

(104) Deepak, T. G.; Anjusree, G. S.; Thomas, S.; Arun, T. A.; Nair, S. V.; Sreekumaran Nair, A. *RSC Adv.* **2014**, *4* (34), 17615–17638.

(105) Galisteo-López, J. F.; García-Santamaría, F.; Golmayo, D.; Juárez, B. H.; López, C.; Palacios-Lidón, E. *Photonics Nanostructures - Fundam. Appl.* **2004**, *2* (2), 117–125.

(106) He, X.; Thomann, Y.; Leyrer, R. J.; Rieger, J. *Polym. Bull.* **2006**, *57* (5), 785–796.

(107) Pham, Q. N.; Barako, M. T.; Tice, J.; Won, Y. *Sci. Rep.* **2017**, *7* (1), 10465.

(108) Yan, H.; Blanford, C. F.; Holland, B. T.; Smyrl, W. H.; Stein, A. *Chem. Mater.* **2000**, *12* (4), 1134–1141.

(109) Chen, X.; Li, Z.; Ye, J.; Zou, Z. *Chem. Mater.* **2010**, *22* (12), 3583–3585.

(110) Etacheri, V.; Seery, M. K.; Hinder, S. J.; Pillai, S. C. *Inorg. Chem.* **2012**, *51* (13), 7164–7173.

(111) Delhez, R.; Keijser, T. H.; Mittemeijer, E. J. *Fresenius Z Anal Chem* **1982**, *312* (1), 1–16.

(112) Cargnello, M.; Gordon, T. R.; Murray, C. B. *Chem. Rev.* **2014**, *114* (19), 9319–9345.

(113) Wu, Y. C.; Tai, Y. C. *J. Nanoparticle Res.* **2013**, *15* (6).

(114) Choi, H. C.; Jung, Y. M.; Kim, S. Bin. *Vib. Spectrosc.* **2005**, *37* (1), 33–38.

(115) Sanchez-Sobrado, O.; Mendes, M. J.; Haque, S.; Mateus, T.; Araujo, A.; Aguas, H.; Fortunato, E.; Martins, R. *J. Mater. Chem. C* **2017**, *5* (27), 6852–6861.

(116) Gollu, S. R.; Sharma, R.; Srinivas, G.; Kundu, S.; Gupta, D. *Org. Electron. physics, Mater. Appl.* **2015**, *24*, 43–50.

(117) Rahimi, K.; Botiz, I.; Agumba, J. O.; Motamen, S.; Stingelin, N.; Reiter, G. *RSC Adv.* **2014**, *4* (22), 11121–11123.

(118) Braun, P. V; Zehner, R. W.; White, C. A.; Weldon, M. K.; Kloc, C.; Patel, S. S.;

Wiltzius, P. *Europhys. Lett.* **2001**, *56* (2), 207–213.

(119) Halaoui, L. I.; Abrams, N. M.; Mallouk, T. E. *J. Phys. Chem. B* **2005**, *109* (13), 6334–6342.

(120) Tulsiram, N.; Kerr, C.; Chen, J. I. L. 1–30.

(121) Liu, J.; Zhao, H.; Wu, M.; Van der Schueren, B.; Li, Y.; Deparis, O.; Ye, J.; Ozin, G. A.; Hasan, T.; Su, B. L. *Adv. Mater.* **2017**, *29* (17), 1–21.

(122) Turner, S. T.; Pingel, P.; Steyrleuthner, R.; Crossland, E. J. W.; Ludwigs, S.; Neher, D. *Adv. Funct. Mater.* **2011**, *21* (24), 4640–4652.

(123) Chasteen, S. V; Carter, S. a; Rumbles, G.; Dept, P.; Cruz, S.; St, H.; Sciences, B.; Lab, N. R. E.; Blvd, C. *Proc. SPIE* **2005**, *5938*, 59380J–1–11.

(124) Noone, K. M.; Anderson, N. C.; Horwitz, N. E.; Munro, A. M.; Kulkarni, A. P.; Ginger, D. S. *ACS Nano* **2009**, *3* (6), 1345–1352.

(125) Haeldermans, I.; Vandewal, K.; Oosterbaan, W. D.; Gadisa, A.; D'Haen, J.; Van Bael, M. K.; Manca, J. V.; Mullens, J. *Appl. Phys. Lett.* **2008**, *93* (22), 1–4.

(126) Noone, K. M.; Subramaniyan, S.; Zhang, Q.; Cao, G.; Jenekhe, S. A.; Ginger, D. S. *J. Phys. Chem. C* **2011**, *115* (49), 24403–24410.

(127) Arndt, C.; Zhokhavets, U.; Gobsch, G.; Winder, C.; Lungenschmied, C.; Sariciftci, N. S. *Thin Solid Films* **2004**, *451–452*, 60–63.

(128) Boschloo, G.; Hagfeldt, A. 2008, pp 729–734.

(129) Dowland, S. a.; Reynolds, L. X.; MacLachlan, A.; Cappel, U. B.; Haque, S. a. *J. Mater. Chem. A* **2013**, *1* (1), 13896.

(130) Braun, S.; Salaneck, W. R.; Fahlman, M. *Adv. Mater.* **2009**, *21* (14–15), 1450–1472.

(131) Beverina, L.; Pagani, G. a; Sassi, M. *Chem. Commun. (Camb).* **2014**, *50* (41), 5413–5430.

(132) Müller, L.; Nanova, D.; Glaser, T.; Beck, S.; Pucci, A.; Kast, A. K.; Schröder, R. R.; Mankel, E.; Pingel, P.; Neher, D.; Kowalsky, W.; Lovrincic, R. *Chem. Mater.* **2016**, *28* (12), 4432–4439.

(133) Enengl, C.; Enengl, S.; Pluczyk, S.; Havlicek, M.; Lapkowski, M.; Neugebauer, H.; Ehrenfreund, E. *ChemPhysChem* **2016**, *17* (23), 3830.

(134) Heinemann, M. D.; Von Maydell, K.; Zutz, F.; Kolny-Olesiak, J.; Borchert, H.; Riedel, I.; Parisi, J. *Adv. Funct. Mater.* **2009**, *19* (23), 3788–3795.

(135) Chen, T. A.; Wu, X.; Rieke, R. D. *J. Am. Chem. Soc.* **1995**, *117* (1), 233–244.

(136) Sheng, C.; Basel, T.; Pandit, B.; Vardeny, Z. V. *Org. Electron.* **2012**, *13* (6), 1031–1037.

(137) Berera, R.; Grondelle, R.; Kennis, J. T. M. *Photosynth. Res.* **2009**, *101* (2), 105–118.

(138) Gao, F.; Li, Z.; Wang, J.; Rao, A.; Howard, I. A.; Abrusci, A.; Massip, S.; McNeill, C. R.; Greenham, N. C. *ACS Nano* **2014**, *8* (4), 3213–3221.

(139) Zhao, W.; Li, S.; Yao, H.; Zhang, S.; Zhang, Y.; Yang, B.; Hou, J. *J. Am. Chem. Soc.* **2017**, *139* (21), 7148–7151.

(140) Hazar Apaydın, D.; Esra Yıldız, D.; Cirpan, A.; Toppare, L. *Sol. Energy Mater. Sol. Cells* **2013**, *113*, 100–105.

(141) Supriyanto, A.; Mustaqim, A.; Agustin, M.; Ramelan, A. H.; Suyitno; Rosa, E. S.; Yofentina; Nurosyid, F. *IOP Conf. Ser. Mater. Sci. Eng.* **2016**, *107*, 12050.

(142) Wang, D.; Tao, H.; Zhao, X.; Ji, M.; Zhang, T. *J. Semicond.* **2015**, *36* (2), 23006.

(143) Ourida, O.; Said, B. M. *Science (80-.).* **2011**, *1* (3), 90–92.

(144) Supriyanto, A.; Maya; Rosa, E. S.; Iriani, Y.; Ramelan, A. H.; Nurosyid, F. *J. Phys. Conf. Ser.* **2016**, *776*, 12012.

(145) Cabanillas-Gonzalez, J.; Virgili, T.; Gambetta, A.; L. Lüer; Lanzani, G.; Anthopoulos, T. D.; De Leeuw, D. M. *Phys. Rev. B - Condens. Matter Mater. Phys.*

2007, *75* (4), 1–7.

(146) Cappel, U. B.; Feldt, S. M.; Schöneboom, J.; Hagfeldt, A.; Boschloo, G. *J. Am. Chem. Soc.* **2010**, *132* (26), 9096–9101.

(147) Wei, X.; Vardeny, Z.; Sariciftci, N.; Heeger, A. *Phys. Rev. B* **1996**, *53* (5), 2187–2190.

(148) Ren, G.; Schlenker, C. W.; Ahmed, E.; Subramaniyan, S.; Olthof, S.; Kahn, A.; Ginger, D. S.; Jenekhe, S. A. *Adv. Funct. Mater.* **2013**, *23* (10), 1238–1249.

(149) Ghosh, R.; Pochas, C. M.; Spano, F. C. *J. Phys. Chem. C* **2016**, *120* (21), 11394–11406.

(150) Caruso, D.; Troisi, A. *… Natl. Acad. Sci.* **2012**, *109*, 13498–13502.

(151) Rezasoltani, E.; Wang, M.; Hill, I. G.; Silva, C. *J. Appl. Phys.* **2014**, *116* (7).

(152) Ohkita, H.; Ito, S. *Polymer (Guildf).* **2011**, *52* (20), 4397–4417.

(153) Jiang, X. M.; Osterbacka, R.; Korovyanko, O.; An, C. P.; Horovitz, B.; Janssen, R. a J.; Vardeny, Z. V. *Adv. Funct. Mater.* **2002**, *12* (9), 587.

(154) Steiner, F.; Lupton, J. M.; Vogelsang, J. *J. Am. Chem. Soc.* **2017**, *139* (29), 9787–9790.

(155) Kowalski, D.; Tighineanu, A.; Schmuki, P. *J. Mater. Chem.* **2011**, *21* (44), 17909.

Appendix

Appendi A: Derivation of refractive index, angle, and colloidal sphere diameter on inverse opal stopband position.

A schematic for the condition of optical interference for two waves effusing through a dielectric material is shown below.

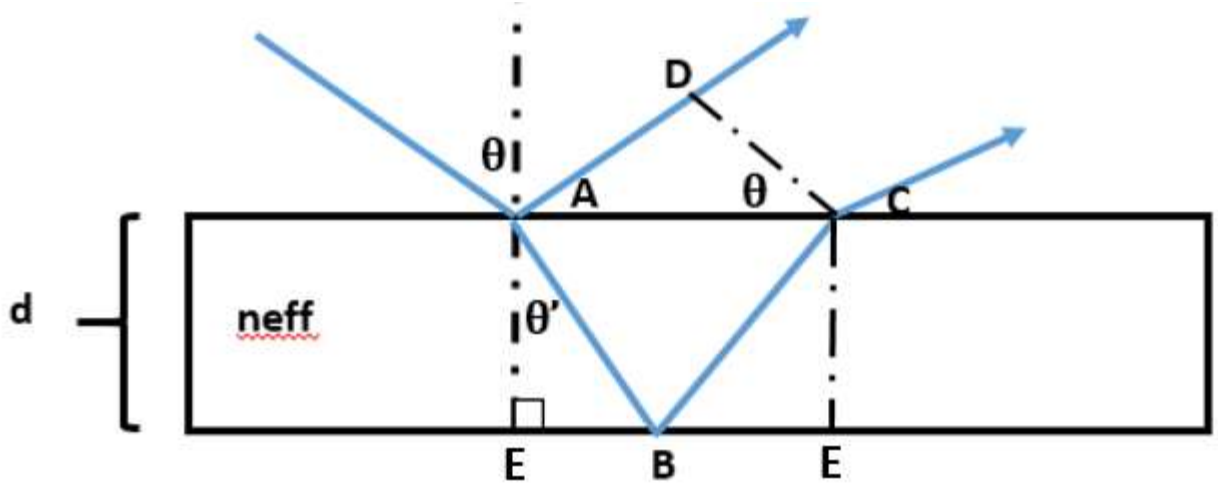

We can express the pathlength of an outgoing wave as the total distance the wave spends inside the dielectric material subtracted by the distance of the original outgoing wave.

$$\boldsymbol{n\lambda = n_1\, d_1 - n_2 d_2}$$

$$\boldsymbol{n\lambda = n_{eff}(AB + BC) - n_{air}(AD)}$$

Where n = the diffraction order and neff is the effective refractive index of the film.

$$\boldsymbol{n_{eff} = n_{air} * f_{air} + n_{dielectric} * f_{dielectric}}$$

The distance AB and BC are equal to distance AB so the above expression can be written as follows.

$$n\lambda = 2AB - AD$$

We can now derive expression for the distance AB in terms of the film thickness and the internal angle (θ').

$$AB = \frac{d}{cos\theta'}$$

The distance AD can be expressed as the product of the sinθ is equal to two times distance BE and arrive at the following expression using trigonometry.

$$BE = 2AC * sin\theta$$

Distance AC can be described in terms of film thickness and internal angle through the following relation.

$$AC = d * tan\theta'$$

$$AC = d * \frac{sin\theta'}{cos\theta'}$$

Thus we arrive at

$$n\lambda = \frac{2 * n_{eff} * d}{cos\theta'} - \frac{2dsin\theta'}{cos\theta'} * sin\theta$$

We can now apply Snell's law to relate sinθ to sinθ' with nair = 1.

$$n_{air} * sin\theta = sin\theta' * n_{eff}$$

And the optical pathlength can be expressed as the following.

$$n\lambda = \frac{2 * n_{eff} * d - 2d * n_{eff} * sin^2\theta'}{cos\theta'}$$

The expression for the optical pathlength difference now reduces to the following.

$$n\lambda = \frac{2 * n_{eff} * d}{cos\theta\,'} * [1 - sin^2\theta\,' \,]$$

And we can apply the identity below to express the condition for constructive interference.

$$cos^2\theta\,' = 1 - sin^2\theta\,'$$

$$n\lambda = 2d * cos\theta\,'$$

Where m either a whole number for constructive interference or a fraction for destructive interference. We can express this relation as a function of the external angle. Again, we can use snell's law to obtain this.

$$\frac{sin\theta}{n_{eff}} = sin\theta\,'$$

And using the identity below.

$$cos\theta\,' = \sqrt{1 - \frac{sin^2\theta}{{n_{eff}}^2}}$$

We arrive at the Bragg expression stopband position as a function of effective refractive index, film thickness, and incident angle.

$$n\lambda = 2 * d * n_{eff}\sqrt{{n_{eff}}^2 - sin^2\theta}$$

We can simplify this futher by expressing the wavelength in terms of the wavelength of light reflected off the film, λ m, which is related to the incidient wavelength λ by the effective refractive index of the medium.

$$\frac{n_m}{n_{air}} = \frac{\lambda_{air}}{\lambda_m}$$

Which results in the following simplified expression.

$$\therefore n\lambda_m = 2d\sqrt{n_{eff}^2 - sin^2\theta}$$

However, we still need to relate d, interplanar distance, to the particle sphere size for the case of a colloidal film. The following expressions were useful for a FCC cell.

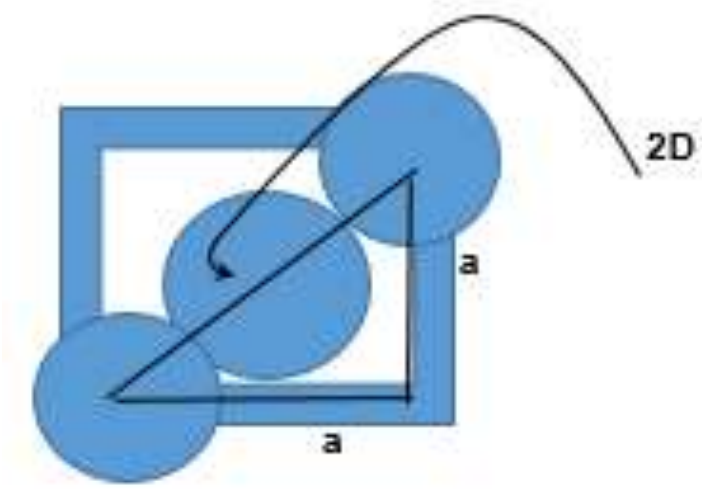

Where a = edge length of a unit cell and D = diameter of sphere. The length of each edge is equal in a face centered cubic array so we can use the pythagoream theorm to arrive at an expression for edge length in terms of the sphere diameter.

$$4D^2 = a^2 + a^2$$

Solve for a in terms of D.

$$\mathbf{a = \sqrt{2}D}$$

We can relate d (interplanar distance) to a by the following expression for a cubic lattice.

$$\mathbf{d} = \frac{a}{\sqrt{h^2 + k^2 + l^2}}$$

Where h,k,l are miller indices. We can substitute 1 for h,k, and l for a face centered cubic lattice since the incident beam that is normal to the film surface intersects with the [111] plane.

$$\mathbf{d} = \frac{\sqrt{2}D}{\sqrt{1^2 + 1^2 + 1^2}}$$

$$\mathbf{d} = \frac{\sqrt{2}D}{\sqrt{3}}$$

We can now substitute the expression for

$$\therefore n\lambda = 2\frac{\sqrt{2}D}{\sqrt{3}} * \sqrt{{n_{eff}}^2 - sin^2\theta}$$

$$n\lambda = mD$$

Where m would be the product of colloid diameter, the refractive index/diffraction angle portion of Bragg's law combined with Snell's law, and the factor accounting for the [1,1,1] miller indices and the edge length of the unit cell in terms of the particle diameter. This m constant can be account for experimentally by measuring the stopband position spectroscopically for an inverse opal experimental slope between D and stop band position ,assuming all other variables remain constant.

Appendix B: Fundamental principles of photoinduced absorption spectroscopy

The intensity of a light source after passing through an absorbing medium (I(x,t)) can be expressed relative to the original intensity (I(t)) by using Beer's law, where x is the thickness of the medium and $\Delta\alpha$ is the change in the absorption coefficient upon production of a population of excited states (N(x)), and $\sigma(E)$ is the absorption cross section.

$$I(x,t) = I(t)e^{-\Delta\alpha x}$$

$$\Delta\alpha(E,x,t) = \sigma(E) * \Delta N(x)$$

The change in the transmission of a material before and after perturbation (for example, before and after light exposure) can be described below, where T_f is the transmission after perturbation and T_i is the transmission prior to perturbation.

$$\Delta T = T_f - T_i$$

$$\frac{\Delta T}{T_i} = \frac{T_f - T_i}{T_i}$$

$$\frac{\Delta T}{T} = \frac{T_f}{T_i} - 1$$

$$\frac{T_f}{T_i} = \frac{I(x,t)}{I(t)} = e^{-\sigma(E)\int_0^d N(x,t)dx}$$

$$\frac{T_i}{T_i} = \frac{I(t)}{I(t)} = e^{-\sigma(E)\int_0^d (0)dx} = 1$$

$$\therefore \frac{\Delta T}{T} = e^{-\sigma(E)\int_0^d N(x,t)dx} - 1$$

Assuming the photoactive material is thin and the differential transmission is on the order of parts per million, the above expression reduces to the following, and the differential transmission is proportional to the excited state population (ΔN).

$$\frac{-\Delta T}{T} = \sigma(E)\int_0^d N(x,t)dx = \sigma(E) * \Delta N(x,t) * d$$

Appendix C: Supporting data

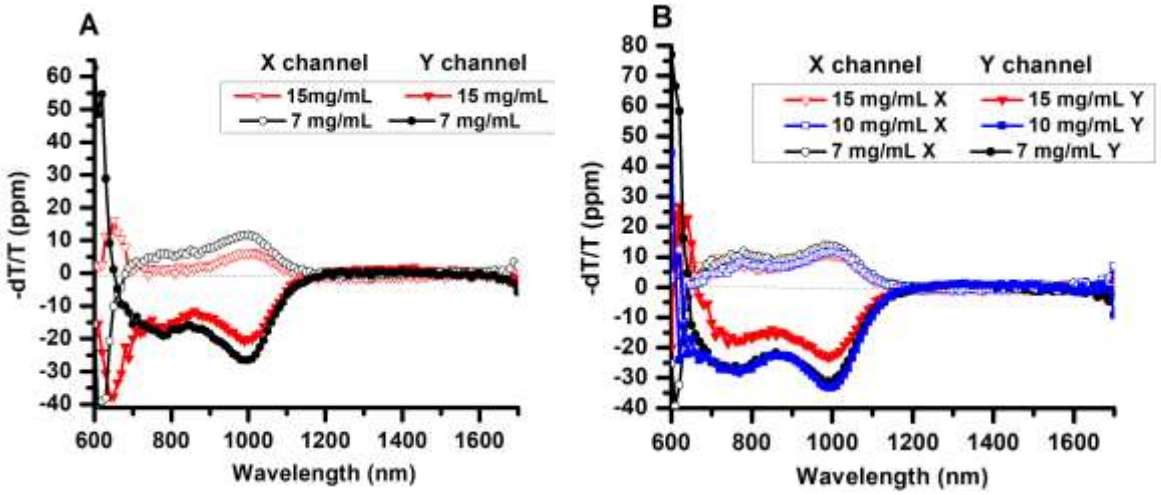

Figure A1: Raw PIA spectra for 140 nm nanocomposites (A) and 177 nm nanocomposites (B) as a function of the concentration of polymer solution from which P3HT is cast. Zero photoinduced absorption is marked by the dashed line.

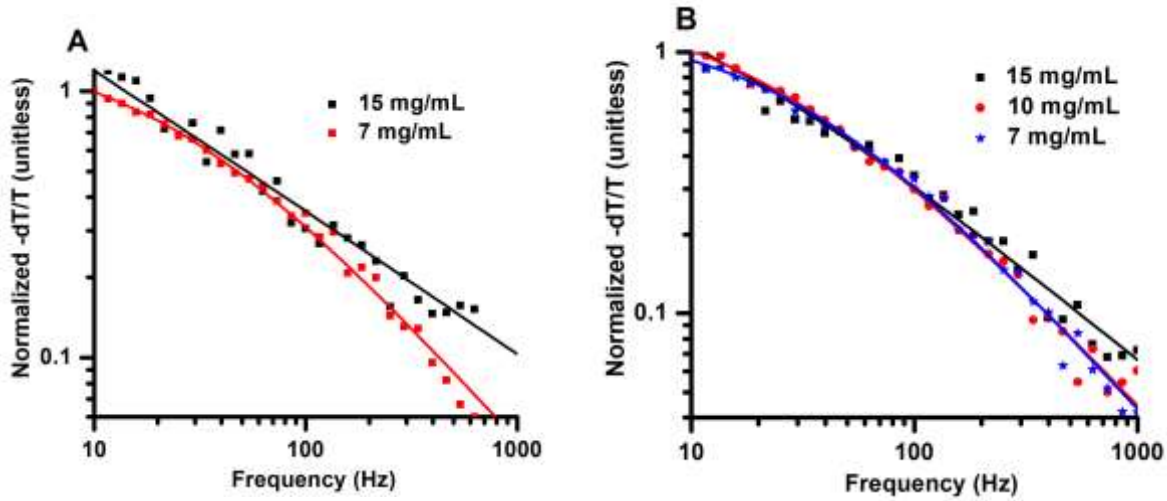

Figure A2: Photomodulation spectra for 140 nm (A) and 177 nm (B) nanocomposites as a function of the concentration of polymer solution from which the P3HT is cast.

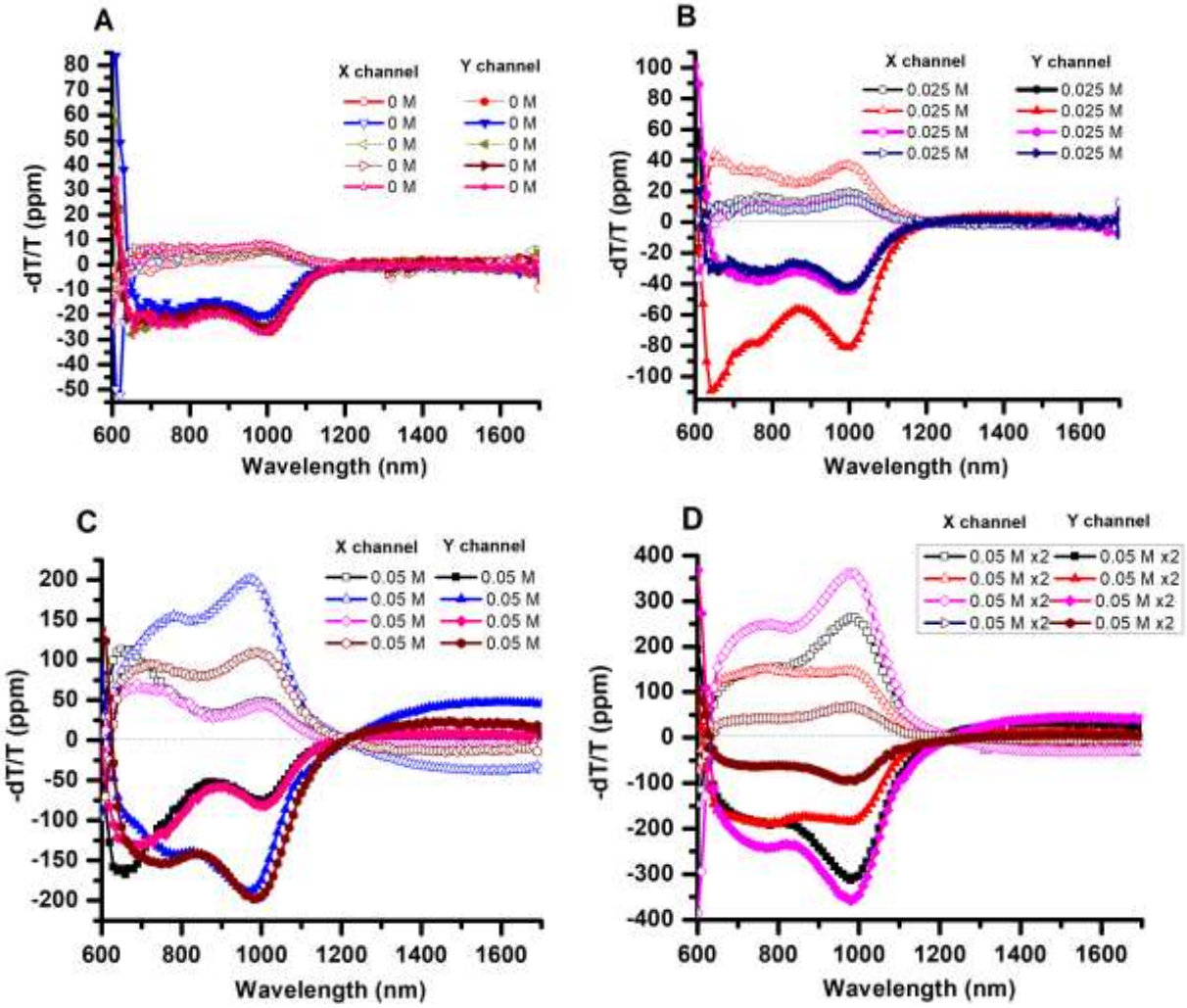

Figure A3: Raw PIA spectra for 140 nm non-passivaed nanocomposites (A) and 0.025 M (B), 0.05 M (C), and 0.05 M x2 (D) $TiCl_4$ treated samples. Zero photoinduced absorption is marked by a dashed line.

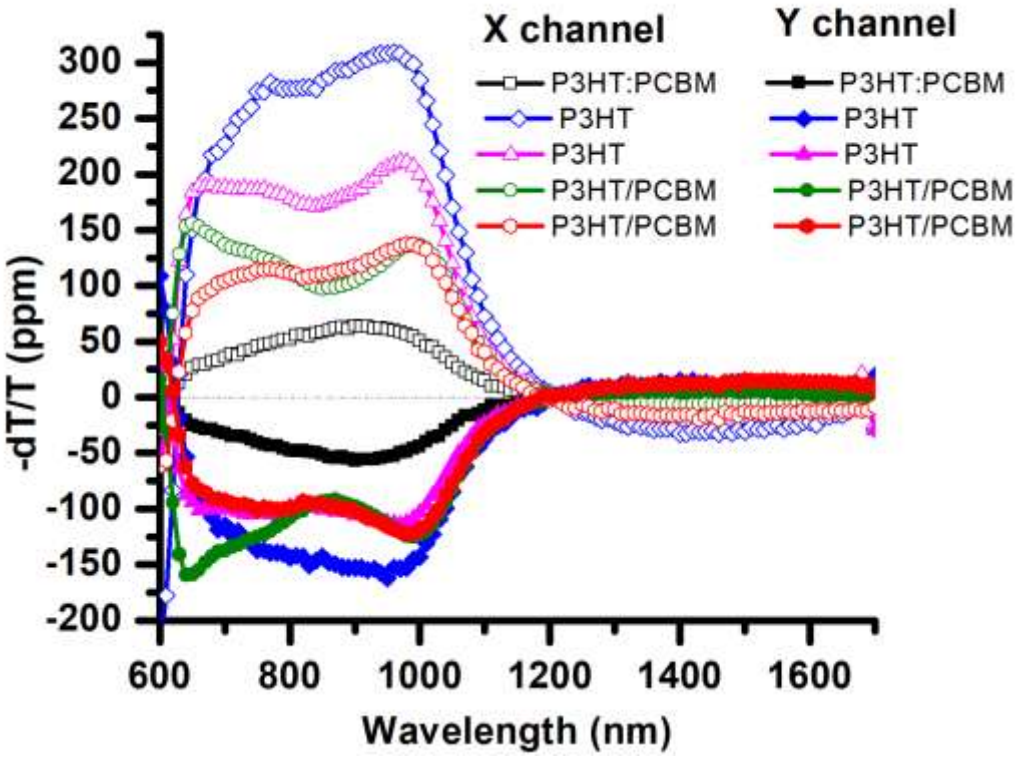

Figure A4: Raw PIA spectra for 140 nm nanocomposites cast with various solutions.

xc

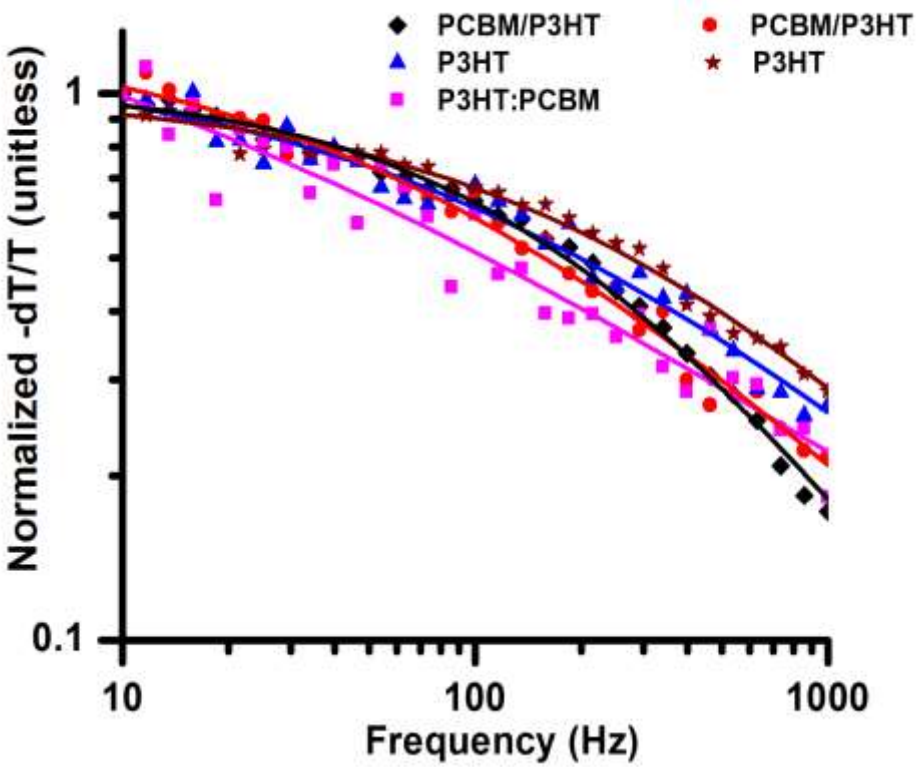

Figure A5: Photomodulation spectra 140 nm nanocomposites cast with various solutions. Modulation fits are marked by solid lines and experimental data are shown as scatter plots.

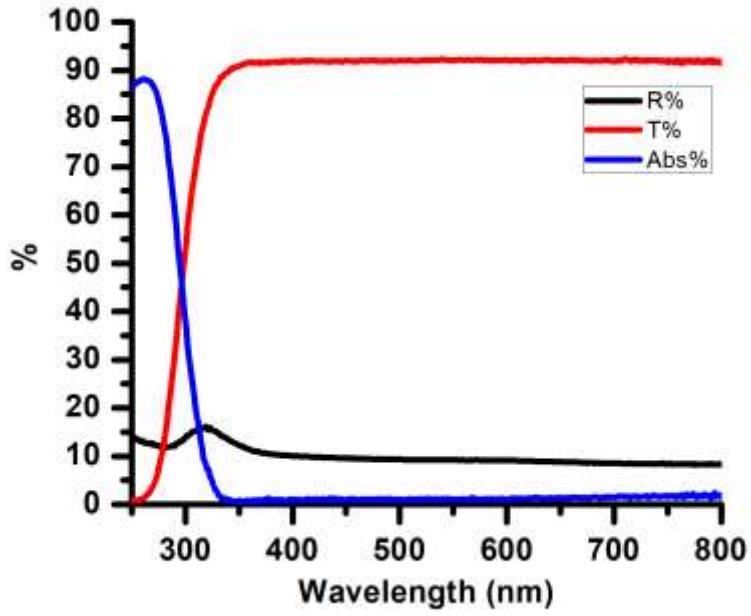

Figure A6: Reference spectra for glass reflectance (black), transmittance (red), and absorptance (blue).